(12) INTERNATIONAL APPLICATION PUBLISHED UNDER THE PATENT COOPERATION TREATY (PCT)

(19) World Intellectual Property Organization
International Bureau

(43) International Publication Date
22 May 2020 (22.05.2020)

WIPO | PCT

(10) International Publication Number
WO 2020/102416 A1

(51) International Patent Classification:
H01L 51/00 (2006.01)

(21) International Application Number:
PCT/US2019/061271

(22) International Filing Date:
13 November 2019 (13.11.2019)

(25) Filing Language: English

(26) Publication Language: English

(30) Priority Data:
62/760,132 13 November 2018 (13.11.2018) US
62/907,405 27 September 2019 (27.09.2019) US
62/927,508 29 October 2019 (29.10.2019) US

(71) Applicant: **DREXEL UNIVERSITY** [US/US]; 3141 Chestnut Street, Philadelphia, MN 19104 (US).

(72) Inventors; and
(71) Applicants: **SPANIER, Jonathan, E.**; 43 Llanberris Road, Bala Cynwyd, PA 19004 (US). **GOLOVINA, Iryna, S.**; 4045 Baltimore Avenue, Apt. A3, Philadelphia, PA 19104 (US). **PLOKHIKH, Aleksandr, V.** [US/US]; 4216 Cedar Avenue, Apt. 3r, Philadelphia, PA 19143 (US).

(72) Inventor: **FALMBIGL, Mattias**; 1666 Callowhill Street, #415, Philadelphia, PA 19130 (US).

(74) Agent: **RABINOWITZ, Aaron, B.**; Baker & Hostetler LLP, 2929 Arch Street, Cira Centre, 12th Floor, Philadelphia, PA 19104-2891 (US).

(81) Designated States *(unless otherwise indicated, for every kind of national protection available)*: AE, AG, AL, AM, AO, AT, AU, AZ, BA, BB, BG, BH, BN, BR, BW, BY, BZ, CA, CH, CL, CN, CO, CR, CU, CZ, DE, DJ, DK, DM, DO, DZ, EC, EE, EG, ES, FI, GB, GD, GE, GH, GM, GT, HN, HR, HU, ID, IL, IN, IR, IS, JO, JP, KE, KG, KH, KN, KP, KR, KW, KZ, LA, LC, LK, LR, LS, LU, LY, MA, MD, ME, MG, MK, MN, MW, MX, MY, MZ, NA, NG, NI, NO, NZ, OM, PA, PE, PG, PH, PL, PT, QA, RO, RS, RU, RW, SA, SC, SD, SE, SG, SK, SL, SM, ST, SV, SY, TH, TJ, TM, TN, TR, TT, TZ, UA, UG, US, UZ, VC, VN, ZA, ZM, ZW.

(84) Designated States *(unless otherwise indicated, for every kind of regional protection available)*: ARIPO (BW, GH,

(54) Title: NANOCRYSTALLINE HIGH-K LOW-LEAKAGE THIN FILMS

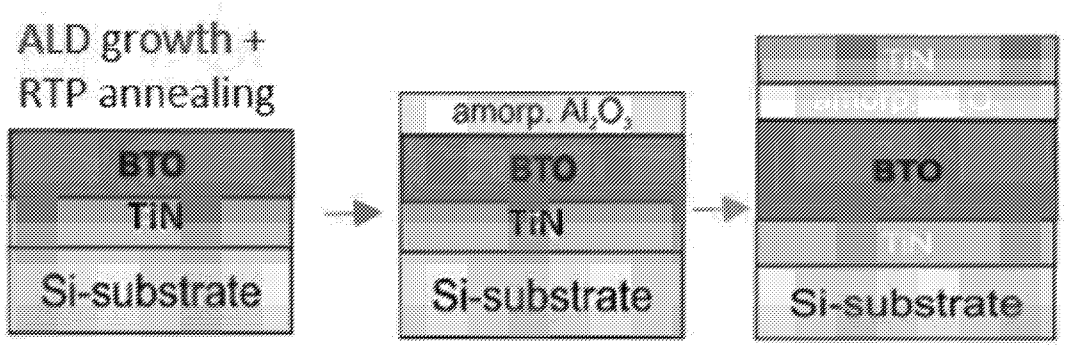

Figure 19

(57) Abstract: Provided is the dielectric response of atomic layer-deposited and annealed polymorphic $BaTiO_3$ and $BaTiO_3$-Al_2O_3 bi-layer thin films based on nanocry stalline $BaTiO_3$ containing the perovskite and hexagonal polymorphs. Also provided are $BaTiO_3$ films having tuned Curie temperatures. Further provided are capacitive components, comprising: a plurality of films, the plurality of films comprising: a first grained film component, the first grained film component comprising at least one of $SrTiO_3$, $BaTiO_3$, and (Ba, Sr)TiO_3, and the first grained film component being characterized as being at least partially polymorphic crystalline in nature; a second film component contacting the first grained film component, the second film component optionally comprising Al_2O_3, and the first grained film component optionally defining an average grain size of less than about 10 micrometers.

WO 2020/102416 A1

[Continued on next page]

GM, KE, LR, LS, MW, MZ, NA, RW, SD, SL, ST, SZ, TZ, UG, ZM, ZW), Eurasian (AM, AZ, BY, KG, KZ, RU, TJ, TM), European (AL, AT, BE, BG, CH, CY, CZ, DE, DK, EE, ES, FI, FR, GB, GR, HR, HU, IE, IS, IT, LT, LU, LV, MC, MK, MT, NL, NO, PL, PT, RO, RS, SE, SI, SK, SM, TR), OAPI (BF, BJ, CF, CG, CI, CM, GA, GN, GQ, GW, KM, ML, MR, NE, SN, TD, TG).

Published:

— *with international search report (Art. 21(3))*

NANOCRYSTALLINE HIGH-K LOW-LEAKAGE THIN FILMS

RELATED APPLICATIONS

[0001] The present application claims priority to and the benefit of United States Application No. 62/760,132, "High Permittivity And Low Leakage Dielectric Thin Film Materials" (filed November 13, 2018); United States Application No. 62/907,405, "Nanocrystalline High-K Low-Leakage Thin Films" (filed September 27, 2019); and United States Application No. 62/927,508 (filed October 29, 2019). The entireties of the foregoing applications are incorporated herein by reference for any and all purposes.

GOVERNMENT RIGHTS

[0002] This invention was made with government support under Contract No. N00014-15-11-2170, awarded by the Office of Naval Research. The government has certain rights in the invention.

TECHNICAL FIELD

[0003] The present disclosure relates to the field of thin film capacitors and also to the field of metal-insulator-metal capacitors.

BACKGROUND

[0004] Many capacitor applications demand both high capacitance and low leakage current. Although efforts have been undertaken to decrease the leakage current of metal-insulator-metal (MIM) capacitors and to create materials having comparatively high dielectric constants, such efforts have to date met with only mixed success. Accordingly, there is a need in the art for capacitor components having both a reduced leakage current and also a comparatively high dielectric constant.

SUMMARY

[0005] Provided is the dielectric response of atomic layer-deposited and annealed polymorphic $BaTiO_3$ and $BaTiO_3$-Al_2O_3 bi-layer thin films based on nanocrystalline $BaTiO_3$

containing the perovskite and hexagonal polymorphs. Also provided are BaTiO3 films having tuned Curie temperatures.

[0006] Compared to an individual $BaTiO_3$ film, a 4-nm thick Al_2O_3 layer in the $BaTiO_3$-Al_2O_3 stack reduces the leakage current by more than 5 orders of magnitude at 1 MV/cm. Therefore, a 32-nm thick $BaTiO_3$ film annealed at 700°C or 750°C and further combined with a 4-nm thick Al_2O_3 layer located between the $BaTiO_3$ film and top electrode exhibits dielectric constants of 108 or 130 and leakage currents $2.2x10^{-8}$ A/mm^2 or $1.3x10^{-7}$ A/mm^2, respectively, at 1 MV/cm at room temperature. An almost order-of-magnitude difference in leakage current is attributed to the larger grain sizes formed in the film after annealing at 750°C as compared to the grains formed at 700°C. Comparison to the most common high-*k* materials reveals the outstanding performance based on the combination of leakage current and dielectric constant for the 32-nm polymorphic $BaTiO_3$ – 4-nm Al_2O_3 thin film stacks. X-ray photoemission analysis study of barrier heights for the metal-$BaTiO_3$-Al_2O_3-metal structure point to using the polymorphic $BaTiO_3$ interspersed between Al_2O_3 layers in tri-layered dielectric thin film capacitors.

[0007] In meeting the described needs in the art, the present disclosure first provides a capacitive component, comprising: a plurality of films, the plurality of films comprising: a first grained film component, the first grained film component comprising at least one of $SrTiO_3$, $BaTiO_3$, and (Ba, Sr)TiO_3, and the first grained film component being characterized as being at least partially polymorphic crystalline in nature; a second film component contacting the first grained film component, the second film component optionally comprising Al_2O_3, and the first grained film component optionally defining an average grain size of less than about 10 micrometers.

[0008] Also provided are capacitive components, comprising: a plurality of films, the plurality of films optionally being disposed between a first electrode and a second electrode, and the plurality of films comprising: a first grained film component, the first grained film component being characterized as being at least partially crystalline polymorphic; a second film component contacting the first grained film component, the second film component optionally comprising Al_2O_3, and the plurality of films optionally having a dielectric constant, at 0 V, of from about 40 to about 140 and optionally a leakage current, measured at 1 MV/cm and 125 deg. C., of from about 10^{-7} A/mm^2 to about 10^{-8} A/mm^2.

[0009] Further provided are articles, the articles comprising a capacitive component according to the present disclosure.

[0010] Additionally provided are methods, the methods comprising discharging electrical energy from a capacitive component according to the present disclosure.

[0011] Further disclosed are methods, the methods comprising storing electrical energy in a capacitive component according to the present disclosure.

[0012] Also provided are methods, the methods comprising energizing an electrical load with energy discharged from a capacitive component according to the present disclosure.

[0013] Also provided are components, the components being made according to the disclosed methods.

[0014] Further provided are nano-grained films, comprising: a $BaTiO_3$ film component comprising a Ba/Ti ratio of between about 0.8 and 1.06, a transition temperature of the nano-grained film being dependent on the Ba/Ti ratio, and the nano-grained film exhibiting a diffused phase transition, optionally whereby a temperature density of a dielectric constant of the nano-grained film is minimized.

[0015] Additionally provided are nano-grained films configured to exhibit a diffused phase transition, whereby a temperature density of a dielectric constant of the nano-grained film is minimized, wherein a transition temperature and the temperature density of the dielectric constant of the nano-grained film is tuned based at least on stoichiometry of one or more materials forming the nano-grained film.

[0016] Further provided are methods, comprising forming a nano-grained film according to the present disclosure.

[0017] Additionally provided are devices, comprising: one or more electrodes in electronic communication with a nano-grained film according to the present disclosure.

[0018] Further provided are methods, comprising operating a device according to the present disclosure.

[0019] Also provided are methods, comprising: tuning a Curie transition temperature of a nano-grained film that comprises a $BaTiO_3$ film component comprising a Ba/Ti ratio of between about 0.8 and 1.06, a transition temperature of the nano-grained film being dependent on the Ba/Ti ratio, and the nano-grained film exhibiting a diffused phase transition, optionally whereby a temperature density of a dielectric constant of the nano-grained film is minimized, the tuning comprising modulating the Ba/Ti ratio.

BRIEF DESCRIPTION OF THE DRAWINGS

[0020] The patent or application file contains at least one drawing executed in color. Copies of this patent or patent application publication with color drawing(s) will be provided by the Office upon request and payment of the necessary fee.

[0021] In the drawings, which are not necessarily drawn to scale, like numerals may describe similar components in different views. Like numerals having different letter suffixes may represent different instances of similar components. The drawings illustrate generally, by way of example, but not by way of limitation, various aspects discussed in the present document. In the drawings:

[0022] FIG. 1. Grazing incidence XRD scans of 32-nm thick BTO films on Pt after deposition and annealing steps.

[0023] FIG. 2. AFM height image of the topography of 32-nm thick BTO films a) after deposition; after annealing b) at 700°C in N_2 flow and depositing 4-nm Al_2O_3, and c) at 750°C in N_2 flow and depositing 4-nm Al_2O_3 for an area of 5 x 5 μm^2 each.

[0024] FIG. 3. Stacking sequence for a bi-layer structure, a ~30-nm thick BTO film and a thin (~4 nm) amorphous Al_2O_3 layer.

[0025] FIG. 4. Leakage current density as a function of applied electric field for 27 nm thick BTO thin films with different thickness of the Al_2O_3-layer after annealing at 500°C.

[0026] FIG. 5. a) Current density as a function of applied electric field for MIM-capacitors after different processing conditions; b) Current density for the positive bias. The crossover of the dashed black lines marks the maximum allowed value per ITRS requirements.

[0027] FIG. 6. a) Dielectric constant as a function of applied electric field for MIM-capacitors with different processing conditions. b) Positive bias for the dielectric constant of the same films.

[0028] FIG. 7. a) Dielectric constant of two MIM-structures with a 32 nm thick BTO structure annealed at 700°C and 750°C under N_2 flow for 10 min and a 4-nm thick Al_2O_3 top layer. b) Current density as a function of electric field for the same MIM-devices measured at room temperature and at 125°C.

[0029] FIG. 8. a) XPS C1s spectra for the Al_2O_3-TiN sample and b) XPS results of the Fermi edges of TiN film on SiO_2/Si (green) and Pt film on SiO2/Si (blue), and valence

bands of a 10-nm thick Al_2O_3 film deposited on the TiN/SiO_2/Si substrate (yellow), 10-nm thick BTO film deposited on the TiN/SiO_2/Si substrate (red), BTO-Al_2O_3 composite stack deposited on the TiN/SiO_2/Si substrate (black), 10-nm thick BTO film deposited on the Pt/SiO_2/Si substrate (purple).

[0030] FIG. 9. A schematic of band alignment for the TiN-BTO-Al_2O_3-TiN structure.

[0031] FIG. 10. Comparison of the dielectric constant at 0 MV/cm and leakage current at 1 MV/cm (or highest electric field measured if below 1 MV/cm) for BTO-Al_2O_3 dielectric stacks to various other high-k thin films and thin film stacks; a particularly desirable material should be located in the top left corner.

[0032] FIG. 11. Raman spectra of 32 nm thick polymorphic BTO films on Pt after different processing steps. The position of the most prominent modes corresponding to the tetragonal (*t*) and the hexagonal (*h*) BTO polymorphs are indicated. For comparison, a Raman spectrum collected for a 50 nm thick BTO film is included.

[0033] FIG. 12. a) Current density for positive bias measured for three different MIM-capacitors (spots) of 32-nm polymorphic BTO – 4-nm Al_2O_3 bi-layer structure after annealing at 750°C at room temperature. b) Dielectric constant for positive bias measured for these three different MIMcapacitors (spots).

[0034] FIG. 13. Tauc plot for a direct allowed band gap for data collected on a 27 nm thick polymorphic BTO film annealed at 700 °C for 5 min deposited on a quartz substrate. The dashed black line represents a linear fit to determine the band gap.

[0035] FIG. 14. Grazing incidence XRD scans of 28-nm thick BTO films on TiN substrates after RTP annealing procedure at different temperature and/or time.

[0036] FIG. 15. AFM images of the topographic height of 28-nm thick BTO films after annealing a) at 850°C for 3 sec; b) at 850°C for 20 sec; c) at 900°C for 3 sec, and d) at 900°C for 10 sec; for an area of 5 x 5 μm^2 each.

[0037] FIG. 16. a) Dielectric constant and b) Current density as a function of applied bias for 28-nm thick BTO films annealed at 850°C for 3 sec. Data were collected at RT and 125°C.

[0038] FIG. 17. a) Relative dielectric constant and b) Current density as a function of applied bias for the 28-nm thick BTO films annealed at 900°C for 3 sec. Data were collected at RT and 125°C.

[0039] FIG. 18. Fitting results for the experimental data considering different conduction mechanisms: (a) Schottky emission, (b) Poole-Frenkel (PF) emission and (c) SCLC mechanism.

[0040] FIG. 19. Schematic of the deposition and processing sequence for the MIM structure with an Al_2O_3 layer between the BTO film and TiN top electrodes.

[0041] FIG. 20. Grazing incidence XRD scans of the 24-nm thick BTO films on TiN substrates after RTP annealing procedure at different temperature.

[0042] FIG. 21. AFM height image of the topography of a) 25-nm thick BTO film after annealing at 850°C for 3 sec; b) 25-nm thick BTO film annealed at 850°C for 3 sec + 2-nm thick Al_2O_3 layer; c) 25-nm thick BTO film annealed at 850°C for 3 sec + 3-nm thick Al_2O_3 layer; for an area of 5 x 5 μm2 each.

[0043] FIG. 22. Relative dielectric constant as a function of applied bias for the 25-nm thick BTO films annealed at 850°C for 3 sec with a) 2-nm thick Al_2O_3 layer and b) 3-nm thick Al_2O_3 layer. Data were collected at RT and 125°C. Measuring frequency was 100 kHz in all cases.

[0044] FIG. 23. Current density as a function of electric field for 25-nm thick BTO films annealed at 850°C for 3 sec with a) 2-nm thick Al_2O_3 layer and b) 3-nm thick Al_2O_3 layer.

[0045] FIG. 24. Fitting results for the experimental data considering different conduction mechanisms in the TiN-BTO-Al_2O_3–TiN MIM-capacitors: (a) Schottky emission, (b) Poole-Frenkel (PF) emission and (c) SCLC mechanism.

[0046] FIG. 25. a) Grazing incidence XRD scans of 28-nm thick BTO film on Pt-coated substrate after RTP annealing at 900°C for 2 min in N2 flow. b) Current density as a function of applied electric field collected for 28-nm BTO – 3.5 nm Al2O3 stack on Pt substrate.

[0047] FIG. 26. Grazing incidence XRD scans of a) the BTO-seed layers of various thickness deposited on TiN substrates and RTP annealed, and b) the main BTO films deposited over the RTP annealed BTO-seed layer and RTP annealed afterwards at 850°C for 3 sec in N_2 flow.

[0048] FIG. 27. Grazing incidence XRD scans of the BTO-Al_2O_3 stacks deposited over 9-nm thick BTO-seed layer RTP annealed at 900°C for 3 sec; afterwards, the whole structure was RTP annealed at 900°C for 3 sec in N_2 flow.

[0049] FIG. 28. Schematic of the deposition and processing sequence for the MIM structure with a BTO film sandwiched between Al_2O_3 layers on the TiN-substrate and with TiN top electrodes.

[0050] FIG. 29. Grazing incidence XRD scans of ~30-nm thick Al_2O_3-BTO-Al_2O_3 composite stacks on TiN substrates after RTP annealing procedure at different temperature and/or time.

[0051] FIG. 30. a) Dielectric constant and b) Current density as a function of applied bias for the ~30-nm thick Al_2O_3-BTO-Al_2O_3 composite stacks on TiN substrates after RTP annealing procedure at different temperature and/or time. For comparison, data for the 28-nm thick BTO-Al_2O_3 stack annealed at 850°C for 3 sec at a heating rate 50°C/sec are also shown. Data were collected at RT.

[0052] FIG. 31. BF TEM images amorphous Al_2O_3-BTO films prepared by one-step and two-step process.

[0053] FIG. 32. STEM BF and HAADF images of a one-step deposited film.

[0054] FIG. 33. SAED of both (one-step and two-step) films.

[0055] FIG. 34. EDS line scans of Al_2O_3-BTO stacks.

[0056] FIG. 35. Grazing incidence XRD scans of a) the 6-nm thick BTO-seed layer a (black) and the main 24-nm BTO film deposited over the seed layer and RTP annealed at 850°C for 3 sec (red), and b) the 9-nm thick BTO-seed layer a (black) and the main 2.5nm Al_2O_3 – 18nm BTO stack deposited over the seed layer and RTP annealed at 900°C for 3 sec (red).

[0057] FIG. 36. a) Dielectric constant and b) Current density as a function of applied bias for the main 24-nm thick BTO film deposited on the top of the 6-nm seed BTO layer and RTP annealed at 850°C for 3 sec.

[0058] FIG. 37. a) Dielectric constant and b) Current density as a function of applied bias for the 2.5 nm Al_2O_3 – 18 nm BTO stack deposited over the 9-nm BTO seed layer and RTP annealed at 900°C for 3 sec.

[0059] FIG. 38. Dielectric constant (black) and losses (red) as a function of measuring frequency collected at RT for a) Pt-BTO-Al_2O_3-TiN MIM-capacitors annealed at 700°C, and b) Pt-BTO-Al_2O_3-TiN MIM-capacitors annealed at 750°C.

[0060] FIG. 39. a) Leakage current density as a function of applied electric field for Pt-BTO-Al_2O_3-TiN MIM-capacitors after different annealing conditions, b) leakage current density for the positive bias.

[0061] FIG. 40 illustrates lattice parameters for the pseudo-cubic structure, a_{pc} (from XRD), and average crystallite size (from TEM) as a function of Ba/Ti ratio.

[0062] FIG. 41 illustrates BF-TEM cross sections of the MIM-structures after the annealing step for the thin films with Ba/Ti-ratio of 1.01 with top Pt electrodes deposited a) before and b) after the annealing procedure. The yellow dashed lines highlight some crystallites within the cross sections.

[0063] FIG. 42 illustrates Temperature dependence (cooling and heating cycles) of a) normalized dielectric constant and b) dielectric loss as a function of the Ba/Ti ratio. Markers – experimental data, lines – fits to equation (1) for the heating cycle.

[0064] FIG. 43 illustrates temperature dependences (on heating) of a) dielectric constant and b) losses at three representative measuring frequencies for the stoichiometric sample (Ba/Ti= 1.01) with top electrodes deposited after the annealing step. Markers are experimental data; lines are guides to the eye.

[0065] FIG. 44 illustrates Polarization behaviour: a) hysteresis loops at 305 K and b) temperature dependence (on heating) of maximum polarization P_{max} at E=0.545 MV/cm (left) and remnant polarization P_{rem} at E=0 (right) for samples with various Ba/Ti ratio. The dashed and solid lines are guides for eye.

[0066] FIG. 45 illustrates Room-temperature hysteresis loop collected at 1 kHz for the thin film with Ba/Ti-ratio of 1.01 and *top electrodes* deposited *after* the annealing step.

[0067] FIG. 46 illustrates Strain from theoretical calculations (circles, triangles), strain determined from XRD (diamonds) and transition temperature T_m (squares) versus Ba/Ti ratio. Markers are experimental or calculated values, solid line is a linear fit (y=-188 + 505x), dashed lines are for clarity.

[0068] FIG. 47 illustrates room-temperature Raman spectra for the stoichiometric thin film (Ba/Ti=1.01) with top electrodes before annealing.

[0069] FIG. 48 illustrates temperature dependences of the frequency, integrated intensity and FWHM of the 520cm^{-1} peak for the Ti-rich sample (Ba/Ti=0.8).

[0070] FIG.s 49 illustrate temperature dependences of frequency, integrated intensity and FWHM of the 520 cm^{-1} (a) and 620 cm^{-1} (b) peaks for the Ba-rich sample (Ba/Ti=1.06).

[0071] FIG. 50 illustrates distribution of grain sizes *beneath top Pt electrodes* deposited *before* annealing step for samples with various Ba/Ti ratios: a) 0.8, b) 0.92, c) 1.01, d) 1.06. Solid red curves are fits to the histogram using a Gaussian.

[0072] FIG. 51 illustrates distribution of grain sizes *beneath top Pt electrodes* deposited *after* the annealing step for a stoichiometric sample (Ba/Ti=1.01). Red curves are two Gaussian functions and the blue curve is the sum of these fit functions to the histogram.

[0073] FIG. 52 illustrates grain size distribution from the TEM cross section between the uncovered area (between top electrodes) obtained for a stoichiometric sample (Ba/Ti=1.01). Solid red curve is the histogram fitting by a Gaussian function.

[0074] FIG. 53 illustrates experimental XPS Ti spectra collected for the films with Ba/Ti=0.8, 0.92, 1.01, 1.06 (a) and fitting of the experimental Ti 2p3/2 peak by a Voigt function.

[0075] FIG. 54 illustrates experimental XPS Ba spectra collected for the films with Ba/Ti=0.8, 0.92, 1.01, 1.06 (a) and fitting of the experimental Ba 3d5/2 spectrum for the film with Ba/Ti=1.06 by a Voigt function.

[0076] FIG. 55 illustrates room temperature current density as a function of electric field (a) and dielectric constant as a function of frequency (b) for the films with Ba/Ti=0.8, 0.92, 1.01 and 1.06.

[0077] FIG. 56 illustrates room temperature hysteresis loops collected at different maximum electric fields and different frequencies for the stoichiometric (Ba/Ti=1.01) film with *Pt electrodes* deposited *after* the annealing procedure.

[0078] FIG. 57 room temperature hysteresis loops collected at a maximum electric field of 0.65 MV/cm and at different frequencies for the stoichiometric (Ba/Ti=1.01) film with *Pt electrodes* deposited *after* the annealing procedure.

[0079] FIG. 58 illustrates temperature dependences of the integrated intensity, frequency, and FWHM of the Raman mode at 620 cm^{-1} for the Ti-rich sample (Ba/Ti=0.8).

[0080] FIG. 59 illustrates grazing incidence X-ray diffraction scans of the 32 nm thick BTO films on Pt after the deposition and annealing steps.

[0081] FIG. 60 illustrates Raman spectra of the 32 nm thick BTO films on Pt after different processing steps. The position of the most prominent modes corresponding to the perovskite (*t*) and the hexagonal (*h*) BTO polymorphs are indicated. For comparison a Raman spectrum collected for a 50 nm thick BTO film is included.

[0082] FIG. 61 (a)-(d) illustrate AFM height image of the topography of the 32 nm thick BTO films **a)** after the deposition, **b)** after annealing at 700 °C in O_2 flow, **c)** after annealing at 700 °C in N_2 flow and depositing 4 nm Al_2O_3, **d)** and at 750 °C in N_2 flow and depositing 4 nm Al_2O_3 for an area of 5 x 5 μm^2 each.

[0083] FIG. 62 (a)-(b) illustrate **a)** HR-TEM image of a 50 nm thick BTO film with Ba/Ti-ratio of 1.06 after annealing at 750 °C in O_2, and **b)** a 50 nm thick BTO film with Ba/Ti-ratio of 0.80 after annealing at 750 °C in O_2.

[0084] FIG. 63 (a)-(b) illustrate **a)** dielectric constant and loss as a function of frequency for ~55 nm thick BTO films with varying Ba/Ti-ratio. **b)** Normalized dielectric constants as a function of applied electric field for the same films. The tunability, *n*, is provided for a field of 1MV/cm.[4]

[0085] FIG. 64 (a)-(b) illustrate temperature dependence (cooling and heating cycles) of **a)** normalized dielectric constant and **b)** dielectric loss as a function of the Ba/Ti ratio.

[0086] FIG. 65 (a)-(b) illustrate **a)** current density (CD) as a function of applied electric field (E) for MIM-capacitors after different processing conditions for positive bias, **b)** Dielectric constant as a function of applied electric field for MIM-capacitors with different processing conditions for positive bias. The inset shows the scheme of the MIM-stack under measurement conditions.

DETAILED DESCRIPTION OF ILLUSTRATIVE EMBODIMENTS

[0087] The present disclosure may be understood more readily by reference to the following detailed description taken in connection with the accompanying figures and examples, which form a part of this disclosure. It is to be understood that this invention is not limited to the specific devices, methods, applications, conditions or parameters described and/or shown herein, and that the terminology used herein is for the purpose of describing particular embodiments by way of example only and is not intended to be limiting of the claimed invention.

[0088] Also, as used in the specification including the appended claims, the singular forms "a," "an," and "the" include the plural, and reference to a particular numerical value includes at least that particular value, unless the context clearly dictates otherwise. The term "plurality", as used herein, means more than one. When a range of values is expressed, another embodiment includes from the one particular value and/or to the other particular value. Similarly, when values are expressed as approximations, by use of the antecedent "about," it will be understood that the particular value forms another embodiment. All ranges are inclusive and combinable, and it should be understood that steps may be performed in any order.

[0089] It is to be appreciated that certain features of the invention which are, for clarity, described herein in the context of separate embodiments, may also be provided in combination in a single embodiment. Conversely, various features of the invention that are, for brevity, described in the context of a single embodiment, may also be provided separately or in any subcombination. All documents cited herein are incorporated herein in their entireties for any and all purposes.

[0090] Further, reference to values stated in ranges include each and every value within that range. In addition, the term "comprising" should be understood as having its standard, open-ended meaning, but also as encompassing "consisting" as well. For example, a device that comprises Part A and Part B may include parts in addition to Part A and Part B, but may also be formed only from Part A and Part B.

[0091] High-k materials are widely used in a variety of integrated circuits, including FETs, DRAM and FeRAM devices, input/output coupling circuitry. Metal-insulator-metal (MIM) capacitors with different high-k individual binary and ternary oxide insulators, *e.g.* HfO_2 (k » 20), Ta_2O_5 (k » 25), TiO_2 (k » 100), ZrO_2 (k » 19-30), $BaHfO_3$ (k » 38), $BaZrO_3$ (k » 40), $SrTiO_3$ (k » 180), $BaTiO_3$ (k » 70-165), $(Ba,Sr)TiO_3$ (k » 200-750) have been fabricated. For capacitor applications, the key functional parameters are high capacitance and low leakage current.

[0092] Significant efforts have been undertaken to decrease the leakage current of MIM-capacitors. One approach is to combine two or more dielectrics into multilayer stacks, *e.g.*, HfO_2–Ta_2O_5, TiO_2-ZrO_2, Al_2O_3–HfO_2–Al_2O_3, $SrTiO_3$-Al_2O_3, $(Ba,Sr)TiO_3$-Al_2O_3, ZrO_2-Al_2O_3-ZrO_2, and ZrO_2/$(Ta/Nb)O_x$-Al_2O_3/ZrO_2. Use of Al_2O_3 in the stacking structure was

shown as an effective way to reduce leakage current. As Al_2O_3 has a relatively low dielectric constant ($k \approx 10$), the other material can have a relatively higher k to maintain a high dielectric constant of the stack, and candidates include $SrTiO_3$ (STO), $BaTiO_3$ (BTO) or $(Ba,Sr)TiO_3$ (BST).

[0093] Atomic Layer Deposition (ALD) is advantageous for fabrication of a nanoscale-conformal insulating thin-film capacitor materials. An excellent conformal step coverage is useful for extreme three-dimensional (3D) structures having a high aspect ratio, *e.g.*, trench structures.

[0094] ALD allows precise stoichiometry control for ternary oxides, high thickness control and good doping control. In addition, ALD utilizes low growth and processing temperatures. In thin-film MIM-capacitors of thickness below 50 nm, interfacial and grain boundary-induced strains in polycrystalline films can drive defect formation, in turn affecting film insulator material electrical properties. While $k \approx 280$ in bulk STO, it exhibits a smaller k ($\approx$ 100-180) in thin films. The effects of post-deposition annealing conditions and doping were explored to control oxygen vacancies formation in ALD-grown thin films.

[0095] By varying the stoichiometry, electrical performance can also be tuned. A thin seed layer can be used to help the overlying film to be crystallized more easily. This approach allows to reduce leakage current as well. For instance, a 5-nm thick STO seed layer annealed at 650°C for 1 min with rapid thermal annealing (RTA) resulted in an improvement in the capacitance (2.7 $\mu F\ cm^{-2}$ without a seed layer vs. 4.5 $\mu F\ cm^{-2}$ with a seed layer) and a decrease in the leakage current density (10^{-1} A cm^{-2} without a seed layer vs. 10^{-5} A cm^{-2} with a seed layer at 1 V) of the main STO layer.

[0096] Also, a 3-nm thick STO seed layer annealed at 700°C for 1 min with RTA resulted in capacitance increase of a 17 nm thick main STO layer by a factor of 5 and a low leakage current density, 10^{-7} A/cm^2 at 0.8 V. As mentioned above, reduced leakage current was present in layered structures when Al_2O_3 was employed. While STO has been studied more widely, the potential of ALD-grown BTO thin films has not been fully explored.

[0097] Here, we utilize seed layering for nanocrystalline and polymorphic BTO (NP/BTO) growth and bi-layering with Al_2O_3 aiming to achieve the combination of high dielectric constant and low leakage current for NP/BTO-based planar MIM capacitors. The present disclosure provides, *inter alia*, the growth and properties of, e.g., a bi-layer BTO-

Al_2O_3 stack, with Al_2O_3 layer between the BTO film and the top electrode. The thickness of the Al2O3 layer can influence leakage current. It is further demonstrated that the NP/BTO film thickness and morphology, in particular grain sizes, can affect leakage current. The findings show that ALD-grown and annealed BTO - Al_2O_3 MIM-stacks simultaneously exhibit a combination of high dielectric constant and low leakage that is superior to other high-k polycrystalline thin-film materials.

[0098] Experimental

[0099] Atomic layer depositions of BTO thin films and BTO-Al_2O_3 bi-layer structures were performed in a Picosun R200 Advanced Reactor on (100)-oriented Si substrates with native oxide layer and Pt(111)/Ti/SiO_2/Si(100) substrates (Gmek Inc.). N_2 gas of 6N purity was used as carrier gas.

[00100] ALD growth of ultrathin Al_2O_3 layers

[00101] We performed ALD-growth of thin Al_2O_3 layers at T = 350°C using TMA (Trimethylaluminum, Sigma-Aldrich 97%) precursor and ozone as a reactant for the deposition. The thickness of the Al_2O_3 layer and corresponding growth per cycle (GPC) vary as the pulses number increases. The pronounced deviation from the linear growth behavior was observed below 40 pulses. The saturation of GPC occurs at 40 pulses as well and produces ~0.92 Å. The uniformity of the Al_2O_3 layers over 100 mm^2 remains above 99%.

[00102] ALD-growth of BTO-Al_2O_3 bi-layers

[00103] Absolut-Ba (Air Liquide, bis(1,2,4 triisopropylcyclopentadienyl)Ba, $Ba(Cp)_2$), high-temperature stable Ti (IV) methoxide (TMO, $Ti(OCH_3)_4$, Alfa Aesar 95%) were used as precursors for Ba and Ti, respectively, and ozone (O_3) as a reactant. For the first set of films a seed layer approach was employed, and »4-5 nm BTO seed layers were annealed at 700°C for 5 min. before depositing a thicker BTO film at 350°C. Due to the lattice mismatch to Pt, a small amount of crystalline BTO forms during the ALD-process, as shown in the X-ray diffraction (XRD) scan revealed by a weak peak at »32° in 2θ (FIG. 1) and atomic force microscopy (AFM) height image by small crystallites (FIG. 2a).

[00104] The properties of MIM-capacitors using a stacking sequence according to FIG. 3a were investigated. In one series we studied the influence of the top Al_2O_3 layer on the crystallization behavior of the BTO film. Al_2O_3 films of 4 nm in thickness were deposited onto amorphous BTO films grown on Si-substrates. Subsequently, two films were annealed in air, one at 700°C for 1 hour and the second film at 800°C for 1 hour. In both cases XRD

showed no sign of crystallization of the BTO layer, which is consistent with reports in literature for STO thin films. This eliminates the option to deposit aluminum oxide before the annealing step. Therefore, the BTO films deposited on Pt/Si were annealed at 700°C and at 750°C for 10 min. in air prior to depositing 4 nm thick Al_2O_3 on the crystalline BTO. The polycrystalline nature of the BTO films after the annealing step was confirmed by XRD (FIG. 1).

[00105] Raman spectra (FIG. 11) confirm the polymorphism in all of the ALD-deposited and annealed BTO thin films, where signature modes of tetragonal as well as hexagonal BTO were clearly observed. These characteristics for polymorphism in these nanocrystalline BTO films are independent of the cation ratio.

[00106] The surfaces for this set of films were examined after the deposition, after annealing at 700°C and at 750°C in N_2 flow, and depositing 4-nm Al_2O_3. Confirming the XRD-results the as-deposited film reveals only small grains on the surface, while annealing results in grain growth and crystallization. That the Al_2O_3 layers in Figs. 2b and 2c cannot be seen as a conformal growth should preserve the topology of the BTO. Interestingly, the average roughness (RMS) does not increase significantly, being »2 nm for all films. An increase of the grain size with annealing temperature is visible, which results in a locally increased variation in film thickness.

[00107] For MIM-capacitors, TiN top electrodes of » 45 nm thickness, a resistivity of 300-400 μΩcm, and a square base area of 90×90 μm^2 were deposited at a power of 450 W utilizing a standard photolithography process and sputtering at room temperature for the »30 nm thick BTO films and BTO-Al_2O_3 bi-layer structures of stacking sequence shown in FIG. 4 grown on Pt(111)/Ti/SiO_2/Si(100) substrates after annealing.

[00108] Structural and Property Characterization

[00109] Grazing incidence X-ray diffraction (GI-XRD) and X-ray reflectivity (XRR) measurements were performed using a Rigaku Smartlab equipped with a Cu-source. Film thicknesses were extracted from XRR data by least squares fits to the modified Bragg equation. Raman spectra were collected in backscattering configuration $z(x,x+y)z^-$ using a single monochromator (XploRA, Horiba Jobin-Yvon, Edison, NJ) and a laser (4 mW, $\lambda = 532$ nm) focused to a spot diameter of ≈10 μm at an intensity of 1.6×103 $W*cm^{-2}$. Light was dispersed using a 2400 gr per mm grating and collected using a Peltier-cooled array detector.

Surface morphology was probed using an Asylum Research MFP-3D atomic force microscope. The transmittance was measured using a Shimadzu UV-2501 PC spectrometer.

[00110] Electrical properties were measured in a metal-insulator-metal (MIM) configuration on the samples grown on Pt(111)/Ti/SiO_2/Si(100) substrates. The bottom electrode was contacted using Ag-paste. The MIM-structured samples were placed in a probe station (Lakeshore Cryotronics TTP4) and measured in air at room temperature and 125°C utilizing a Keithley SCS-4200 electrometer.

[00111] XPS measurements were performed using a Physical Electronics VersaProbe 5000 under a base-pressure of ~10^{-6} Pa. An Al-Kα source provided incident photons with an energy of 1486.6 eV at 10 kW mm^{-2}. XPS spectra were collected with the pass energy of 23.5 eV. An electron neutralizer was used to neutralize the surface. Linear energy correction was applied in reference to the carbon spectra. The energy of the C1s peak of non-oxidized carbon was set at 284.8 eV. The detector was placed at the angle of 87.2° relative to the surface of the films.

[00112] Exemplary Results and Discussion

[00113] BTO films and BTO-Al_2O_3 stacks

[00114] To investigate the influence of the Al_2O_3 layer thickness on the leakage current, layers of Al_2O_3 of 1 nm, 2 nm, and 3 nm in thickness were deposited on the BTO film as described above. The thicknesses of the layers were confirmed by XRR. The results of leakage current measurements at room temperature for slightly Ba-rich films after annealing at 500°C are displayed in FIG. 4. The voltage was first ramped up to +4V in 0.1 increments and then from 0 to -4V. Compared to the individual (without Al_2O_3) BTO film, a 2-nm thick Al_2O_3 allows one to decrease the leakage current by »2 orders of magnitude at 1 MV/cm, while a 3-nm thick Al_2O_3 layer reduces leakage current by »5 orders (FIG. 4). In subsequent experiments, a 4-nm thick Al_2O_3 layer was used.

[00115] FIG. 5 provides the room-temperature leakage current density as a function of process conditions for these films. The different processing and annealing steps were: i) as deposited: after the ALD-growth of the film, ii) 700°C+ 4-nm Al_2O_3 and iii) 750°C+ 4-nm Al_2O_3: subsequent annealing for 10 min under N_2 flow, followed by the growth of 4-nm Al_2O_3.

[00116] It can be seen in FIG. 5a that the as-deposited film exhibits a low current density, $3x10^{-10}$ A/mm^2 at 1 MV/cm, in agreement with the amorphous state determined by

XRD. After annealing, the leakage current increases and becomes asymmetric. This asymmetry may arise due to two-step ALD-growth, as first the BTO film was deposited and annealed and then the Al_2O_3 layer was deposited. As a result, interface defects and contamination layer introduced at the film surface, lead to the bigger difference in the Schottky barrier heights at the Pt-BTO and TiN-Al_2O_3 interfaces as will be shown below. However, the data for positive bias are expected to be representative for the properties of the MIM-stacks. In FIG. 5b the positive bias is shown along with the minimum ITRS requirement (10^{-8} A/mm^2, at higher voltages).

[00117] Comparing the films annealed at 700°C with and without Al_2O_3 layer, one sees that a 4-nm amorphous Al_2O_3 layer reduces the current density by one order of magnitude below this value. Annealing at 750°C increases the leakage current again by one order of magnitude. Without being bound to any particular theory, one can attribute this increase to the larger grains observed by AFM (see Figs. 2b and 2c), which results to locally increased electric fields due to variations in the film thickness.

[00118] The dielectric constant as a function of electric field for the same MIM-capacitors is shown in FIG. 6. We calculated the dielectric constant of the BTO-Al_2O_3 stacks using the standard model for two parallel-plate capacitors in series. Similar to the leakage current a strong asymmetry is observed for the dielectric constant. Under negative bias also the dielectric loss (not shown) increases dramatically (by at least 3 orders). The measured dielectric constant has a large contribution from space charge, *i.e.*, charge carriers leaking through the device, and cannot be considered as a reliable value (FIG. 6a). On the other hand, under positive bias the dielectric losses remain below 10^{-2} and the contribution to the dielectric constant can (again without being bound to any particular theory) be attributed to the insulating BTO-Al_2O_3 stack.

[00119] The as-deposited MIM-structure has a very low field independent dielectric constant of 18 as expected for an amorphous film. After annealing, the dielectric constant for all MIM-devices shows a similar field-dependence with the film annealed at 700 °C exhibiting a value of 108 at electric field $E = 0$ and the film annealed at 750 °C exhibiting a value of 130 at E=0, respectively. Both MIM-capacitor stacks exceed a value of 100. One can notice a good reproducibility between different Pt-BTO–Al_2O_3-TiN capacitors (FIG. 12).

[00120] To test these devices for capacitance and leakage current, we performed additional testing under the defined conditions for the two MIM-structures with Al_2O_3 layer

of 4 nm annealed at 700°C and 750°C (FIG. 7). The relevant performance parameters for these 2 structures are provided in Table 1.

[00121] To test these devices for capacitance and leakage current, we performed additional testing under the defined conditions for the two MIM-structures with Al_2O_3 layer of 4 nm annealed at 700°C and 750°C (FIG. 7). The dielectric constant at 6.3V drops below 50 for the BTO–Al_2O_3 stack annealed at 700°C, while it remains at 55 at 6.3 V for the BTO–Al_2O_3 stack annealed at 750°C meeting the defined range (FIG. 7a). In testing different top electrode spots, while for the BTO–Al_2O_3 structure annealed at 700°C »80-90 % of the MIM-capacitors were able to withstand 6.3V bias, for the BTO–Al_2O_3 structure annealed at 750°C this rate dropped below 50 %. A similar observation was made for the leakage current tests at 125°C showing that annealing at 750°C results in less stable films with larger fluctuations of the properties. The current density for both films increases by one order of magnitude between room temperature and 125°C with higher values than 10^{-8} A/mm^2. The relevant performance parameters for these 2 structures are provided in Table 1, below.

[00122] **Table 1.** Total thickness, dielectric constant at 6.3V and leakage current density at room temperature and 125°C for two most promising BTO-Al_2O_3 bi-layer stacks.

	Thickness	Dielectric Constant	Leakage Current density
Annealed at 700°C, Pt-BTO-Al_2O_3-TiN	36	44	2.2 x 10^{-8} A/mm^2 at RT 5 x 10^{-7} A/mm^2 at 125°C
Annealed at 750°C, Pt-BTO-Al_2O_3-TiN	36	53	1.3 x 10^{-7} A/mm^2 at RT 2.5 x 10^{-6} A/mm^2 at 125°C

[00123] Band alignment for the Pt-BTO-Al_2O_3-TiN structure

[00124] To gain a deeper insight into the nature of the leakage current in the bi-layered stack, an effort was made to reconstruct a band alignment from the study of barrier heights for the Pt-BTOAl_2O_3-TiN structure. For collecting experimental data, we applied XPS technique which has been widely used for many years to explore the metal/dielectric interface formation and band alignment.

[00125] For this study, six samples were prepared: 1) commercially available metallized substrate with a 20-nm TiN film sputtered on SiO_2/Si<100>; 2) as-deposited 10-nm thick Al_2O_3 film grown on the TiN/SiO_2/Si substrate; 3) 10-nm thick BTO film grown on the TiN/SiO_2/Si substrate; this film was annealed at 700 °C for 3 min in air; 4) 10-nm thick BTO film grown over Al_2O_3/TiN/SiO_2/Si film; this film was annealed at 700 °C for 3 min in

air; 5) commercially available metallized substrate with a 150-nm Pt film sputtered on SiO_2/Si<100>; 6) 10-nm thick BTO film grown on the Pt/SiO_2/Si substrate; this film was annealed at 700 °C for 3 min in air. In addition, we used magnetron-sputtered TiN as top electrodes to ensure that the process identically works for both bottom and top TiN/dielectric contact interfaces. The film thickness has been obtained from the XRR scans.

[00126] Stoichiometry and crystallinity for BTO films were confirmed from SEM/EDS and XRD data. For each sample, the XPS spectrum of C1s as well as the valence band and/or Fermi energy band spectra have been collected. The presence of carbon is due to unavoidable surface contamination. As we take the C1s lines as a standard for a linear calibration, the C1s spectra was fitted by three Voigt (Gaussian/Lorentzian=70/30) functions. The XPS C1s spectra for the sample Al_2O_3-TiN is presented in FIG. 8a. The Fermi energy position for the samples TiN, Pt and TiNAl_2O_3 was defined as the middle of the first slope at a low-energy edge of binding energy scale. The valence band maximum (VBM) for the samples TiN-Al_2O_3, TiN-BTO, TiN-Al_2O_3-BTO and Pt-BTO is determined by the intercept of the base line and the leading edge of valence band spectrum, as depicted in FIG. 8b. For clarity, the Fermi edges of TiN and Pt were set at 0 eV and the other XPS spectra were shifted accordingly. Therefore, the energy offset between the TiN Fermi energy and VBM extracted from these spectra is 3.0 eV and 2.5 eV for BTO and Al_2O_3, respectively. Note that the energy offset is 2.85 eV for the sample TiN-Al_2O_3-BTO. However, because the thickness of BTO layer is ~10 nm, we can get the XPS response mainly from BTO and slightly from Al_2O_3. As a result, we observe the shift of VBM at 0.15 eV for the sample TiNAl_2O_3-BTO compared to the sample TiN-BTO. The energy offset between the Pt Fermi energy and VBM of the BTO is 3.0 eV. Using these XPS results, we reconstructed the band alignment for the structure Pt-BTO-Al_2O_3-TiN, shown in FIG. 9.

[00127] The Schottky barrier height (SBH), f_n, which is determined as the difference between the conduction band minimum (CBM) of a dielectric, E_c, and the Fermi energy position of metal, E_F, can be obtained using the band gaps 3.85 eV for BTO, determined experimentally (FIG. 13), and 6.2 eV for ALD-grown Al_2O_3, taken from the literature.

[00128] The values of SBH can be thus estimated as f_n=0.85 eV for Pt-BTO interface and f_n=3.2 eV for TiN-Al_2O_3 interface. Also, we notice the difference between the CBM of BTO and Al_2O_3 at the BTO-Al_2O_3 interface, that amounts 0.6 eV. The SBH values

determined from the experimental data differs from the values of ideal Schottky barrier which is formed at an interface in the Schottky limit and can be estimated from the Schottky-Mott rule, $\phi_B = F_m - \chi_i$, where F_m is the work function of the metal contact and χ_i is the electron affinity of the dielectric. Based on the reported work functions of TiN (F_m=4.6 eV) and Pt (F_m=5.6 eV) and the electron affinity of BTO (3.8 eV) and Al_2O_3 (2.58 eV), the SBH is 1.8 eV and 2.02 eV for Pt-BTO and TiN-Al_2O_3 interfaces, respectively. The presence of the surface contamination layer and point defects introduced at the film surface during fabrication are usually considered as the causes for the difference between experimentally observed and ideal Schottky barriers. The difference between experimental values of the SBH for Pt-BTO interface (f_n=0.85 eV) and for TiN-Al_2O_3 interface (f_n=3.2 eV) can explain the asymmetry in the electric-field dependences of leakage current and dielectric constant (Figs. 5a and 6a, respectively).

[00129] Comparison of different high-k oxide thin films

[00130] Comparing our results to a variety of other high-k oxides, both individual materials and multilayered structures, reveals the remarkable performance for the nanocrystalline polymorphic BTOAl_2O_3 thin film stacks (FIG. 10) in terms of the combination of leakage current and dielectric constant. In this respect the nanocrystalline polymorphic BTO-Al_2O_3 thin-film stacks produced in present work are well separated from other reported materials. In particular, the comparison to STO-Al_2O_3 stacks with STO thickness of 50 nm and Al_2O_3 of up to 4 nm demonstrates the superior performance of the disclosed materials.

[00131] Conclusions

[00132] Compared to the individual (without Al_2O_3) BTO film, a 2-nm thick Al_2O_3 allows one to decrease the leakage current by »2 orders of magnitude at 1 MV/cm, while a 3-nm thick Al_2O_3 layer reduces leakage current by »5 orders. A 4-nm thick Al_2O_3 layer thus provides substantially reduced leakage current, while it still preserves a high effective dielectric constant of the stack.

[00133] A bilayer stack that encompasses a 32-nm thick BTO film annealed at 700°C and a 4-nm thick Al_2O_3 layer deposited over the BTO film exhibited dielectric constant 108 at 0V and 44 at 6.3V, respectively, while leakage current is $5x10^{-7}$ A/mm^2 and $2.2x10^{-8}$ A/mm^2 at 125°C and room temperature, respectively.

[00134] A bilayer stack that encompasses a 32-nm thick BTO film annealed at 750°C and a 4-nm thick Al_2O_3 layer deposited over the BTO film exhibits dielectric constant 130 at 0V and 53 at 6.3V, respectively, while leakage current is $2.5x10^{-6}$ A/mm^2 and $1.3x10^{-7}$ A/mm^2 at 125°C and room temperature, respectively. Higher leakage current is attributed to the greater grain sizes in BTO film due to annealing at higher temperature.

[00135] Reconstruction of a band alignment for the Pt-BTO-Al_2O_3-TiN structure shows that Al_2O_3 layers located between TiN electrode and BTO can substantially reduce leakage current. In addition, the quality of BTO-Al_2O_3 interface should be taken into consideration.

[00136] Compared to common high-*k* materials the films presented in this work demonstrate a better overall performance considering both key parameters, dielectric constant and current density.

[00137] Additional Disclosure

[00138] Characterization and electrical testing of the BTO films on TiN-coated substrates

[00139] BTO films were grown using Absolut-Ba (Air Liquide, bis(1,2,4 triisopropylcyclopentadienyl) Ba, Ba(Cp)2) and high-temperature stable Ti (IV) methoxide (TMO, $Ti(OCH_3)_4$, Alfa Aesar 95%) as precursors for Ba and Ti, respectively, and ozone (O_3) as a reactant. The deposition was carried out at 350°C.

[00140] The first set of samples we investigated involved 28-nm thick BTO films grown on TiN-coated substrates. Taking the aforementioned RTA approach in mind, we performed RTP annealing at 700°C, 800°C, 850°C, and 900°C. Annealing time was varied from 1 to 30 sec. In all cases, N_2 flow was used. Samples were investigated using XRD and SEM/EDS to identify the onset of BTO crystallization and to control the stoichiometry.

[00141] The representative XRD scans are presented in FIG. 14. No evidence of the BTO phase is observed for the film annealed at 800°C. However, crystallization of BTO appears in the films annealed at 850°C for 3 sec, at 850°C for 20 sec, and at 900°C for 3 sec. This is reflected in the XRD scans with a (110) peak at ~32° in 2θ and weak (111) and (200) peaks at ~38° and 44°, respectively.

[00142] The XRD scan for the BTO film annealed at 900°C for 10 sec shows a weaker (110) peak than that for the samples annealed at 900°C for 3 sec. This result indicates that longer annealing time at 900°C leads to the partial degradation of the BTO phase.

Annealing at 850°C for 20 sec results in the (110) peak of the same intensity compared to that for sample annealed at 850°C for 3 sec. On the other hand, the (111) and (200) peaks are almost unseen in the XRD scan for the sample annealed at 850°C for 20 sec. Based on XRD data, crystallization of the BTO thin film on TiN-coated substrate occurs after RTP annealing at 850°C and at 900°C both for 3 sec in N_2 flow.

[00143] The surfaces for this set of films were examined after annealing at 850°C for 3 sec and for 20 sec, and after annealing at 900°C for 3 sec and for 10 sec. The AFM data are presented in FIG. 15. Examining the XRD results for the film annealed at 850°C for 3 sec reveals tiny grains on the surface, while annealing at the same temperature for longer time appears to result in partial deterioration of the BTO phase.

[00144] The average roughness (RMS) is small, around 0.2 nm, for the two films. An increase of the grain size with annealing temperature is clearly visible in FIG. 15c. However, the surface is not uniformly covered by grains, resulting in a locally increased variation in film thickness and in an increased RMS up to 2.5 nm. The BTO surface in FIG. 15d again shows partial degradation of the BTO phase. The average roughness decreases with phase deterioration and becomes ≈0.5 nm for the film annealed for 10 sec. at 900°C.

[00145] For MIM-capacitors, TiN top electrodes of ≈45 nm thickness and a square base area of 90 × 90 μm2 were deposited at a power of 450 W utilizing standard photolithography and sputtering at room temperature on the 28 nm thick BTO films annealed at 850°C and at 900°C that are crystallized or partially crystallized as determined by the XRD and AFM data. The electrical properties under applied electric field for two representative films are shown in Figs. 16 and 17.

[00146] The relative dielectric constant at E = 0 is ≈30 for both films. This result corroborates the XRD and AFM data that the films are partially amorphous. The TiN-BTO-TiN MIM-capacitors based on these films were tested for dielectric constant and leakage current at RT and 125°C. It can be seen from Figs. 16a and 17a that the relative dielectric constant >50 under positive bias at 6.3V at 125°C for both films.

[00147] To gain insight into the nature of leakage current, we considered different conduction mechanisms for the BTO film annealed at 900°C. Because the E-field dependence is symmetric in positive and negative bias directions, the analysis can be conducted for the positive upward bias. We consider Schottky emission, Poole–Frenkel (PF) emission and

space-charge limited conduction (SCLC) mechanisms, which are commonly observed in perovskite oxides.

[00148] The relation between current density, J (or conductivity s), and voltage, V, for each of these mechanisms is:

$$\text{Schottky emission: } J_S = AT^2 exp - [\frac{\Phi}{k_B T} - \frac{1}{k_B T}\sqrt{\frac{q^3 V}{4\pi\varepsilon_0 K d}}] \quad (1)$$

$$\text{Poole-Frenkel emission: } \sigma_{PF} = c\ exp - \left[\frac{E_l}{k_B T} - \frac{1}{k_B T}\sqrt{\left(\frac{q^3 V}{\pi\varepsilon_0 K d}\right)}\right] \quad (2)$$

$$\text{SCLC mechanism: } J_{Ohm} = \frac{qn_0\mu V}{d},\ J_{TFL} = \frac{9}{8}\mu\varepsilon\Theta\frac{V^2}{d^3}, J_{Child} = \frac{9}{8}\mu\varepsilon\frac{V^2}{d^3} \quad (3)$$

[00149] In equations (1)-(3), A is the Richardson constant, T is the temperature, Φ is the height of the Schottky barrier, k_B is the Boltzmann constant, q is the elementary charge, V is the applied voltage, ε_0 is the permittivity of free space, K is the optical dielectric constant, d is the sample thickness, c is a constant, E_1 is the trap ionization energy, n_0 is the concentration of the free charge carriers in thermal equilibrium, μ is the mobility of charge carriers, ε is the static dielectric constant and Θ is the ratio of the free carrier density to total carrier (free and trapped) density.

[00150] As equations (1) and (2) show, Schottky and Poole-Frenkel emission are similar in terms of current-voltage relationship, but the first one is interface-limited, while the second one is bulk-limited. Representative dependences for these different mechanisms are shown in FIG. 18. In general, each mechanism contributes to the electrical conductivity, so that strictly speaking, one can identify only the dominating mechanism. As can be clearly seen from the fitting in FIG. 18, the SCLC mechanism is dominant in the film. For this mechanism, the log J – log V dependence is comprised of three distinct regions, namely, Ohm's law, traps-filled limit (TFL) current, and Child's law with the points V_{tr} and V_{TFL} which are the transition voltages between the regions. In the film, the transition voltage V_{tr} is 0.25 V. Note that V_{tr} is the voltage at which the transition from Ohm's law to SCLC takes place. At this point, the traps are filled up and a space charge appears. V_{TFL} defined as the voltage required to fill the traps is 0.75 V for this film.

[00151] Formation of the BTO over the post-deposition annealing occurs in accordance with the reaction: $BaO + TiO_2 = BaTiO_3$. It means that crystallization implies 3

steps: 1) breaking of the Ba-O and O-Ti-O bonds, 2) diffusion of the Ba, Ti and O atoms, 3) formation of the $BaTiO_3$ perovskite structure.

[00152] Characterization and properties of BTO-Al_2O_3 stacks with Al_2O_3 layer between BTO and TiN top electrode

[00153] Fabrication of the TiN-BTO-Al_2O_3–TiN MIM-capacitors with an Al_2O_3 layer located between the BTO film and TiN top electrodes follows the steps presented in FIG. 19. First, we deposited the 25-nm thick Ba-Ti-O on TiN substrate and cut as-deposited film into four pieces. Two of the four pieces were RTP annealed at 850°C for 3 sec and other two at 900°C for 3 sec.

[00154] Before depositing top Al_2O_3 layer, the XRD scans were collected to ensure that the BTO phase has been formed (FIG. 20). While all four peaks are very well defined in the XRD-pattern for the film annealed at 850°C, (100) and (110) peaks are much weaker for the film annealed at 900°C. It indicates that the BTO phase is well crystallized already at 850°C, while it is partially decomposed at 900°C temperature. This is quite reasonable, as a thinner film can be expected to require a reduced annealing temperature for crystallization.

[00155] In order to show the influence of the thickness of the Al_2O_3 layer, we deposited 2-nm and alternately 3-nm thick Al_2O_3 layers on the annealed 25-nm thick BTO/TiN films.

[00156] FIG. 21 shows the topographical AFM images of these films and their roughness mean square (RMS) values for an area of 5 x 5 μm^2. The BTO phase crystallites can be clearly seen in FIG. 21a. This topology becomes almost indiscernible for the films with top Al_2O_3 layer. The top Al_2O_3 layer also impacts the surface smoothness. The RMS value decreases from 3 nm for the film without Al_2O_3 layer, to 2.4 nm with the 2-nm thick Al_2O_3 layer and to 1.7 nm with 3-nm thick Al_2O_3 layer.

[00157] The electrical properties under applied electric field for two representative BTO-Al_2O_3 films with 2-nm and 3-nm thick Al_2O_3 layer are shown in Figs. 22 and 23. We notice that dielectric constant at $E = 0$ is around 70 for both films. This value is higher than that for the 28-nm thick BTO films without Al_2O_3 layer (see previous section). This result is in agreement with XRD and AFM data, and evidences a better level of crystallization of the 24-nm thick BTO film annealed at 850°C for 3 sec compared to the 28-nm thick BTO annealed at 900°C for 3 sec. At positive bias of 6.3V, dielectric constant of the BTO-Al_2O_3 stack is 30 at RT and ~50 at 125°C for both, 2-nm and 3-nm thick, Al_2O_3 layers.

[00158] The TiN-BTO-Al_2O_3–TiN MIM-capacitors were also tested at RT and 125°C. Representative data collected for the BTO-Al_2O_3 stacks that contain BTO films annealed at 850°C are shown in FIG. 23. It can be seen that 3-nm thick Al_2O_3 layer allows to decrease leakage current in 1 order of magnitude compared to the 2-nm thick Al_2O_3 layer at E = 0 at RT. However, leakage current is the same at 1 MV/cm at RT and 125°C for both, 2-nm and 3-nm thick Al_2O_3 layer.

[00159] Again, we considered different conduction mechanisms in order to identify possible reasons for high leakage current. The analysis of three conduction mechanisms was made as described above. The comparison of the results presented in FIG. 24 for the TiN-BTO-Al_2O_3–TiN MIM-capacitors with the results obtained for the TiN-BTO-TiN MIM-capacitors shown in FIG. 18 demonstrates that the nature of the leakage current is identical and comes predominantly from the space charges formed in the BTO layer.

[00160] The transition voltage V_{tr} is 0.35 V in the TiN-BTOAl_2O_3–TiN MIM-capacitor, that is a little higher than V_{tr}=0.25 V in the TiN-BTO-TiN MIMcapacitor. The voltage required to fill the traps V_{TFL} is 0.75 V for the TiN-BTO-Al_2O_3–TiN structure, which is the same as for the TiN-BTO-TiN film.

[00161] To investigate the bottom electrode's contribution to leakage current, we produced and tested the BTO-Al_2O_3 stacks on Pt-substrates. For this structure, the 28-nm thick BTO film was annealed at 950°C for 2 min in N_2 flow to have the sigh of BTO phase in XRD scan (FIG. 25a).

[00162] The 3.5 nm thick Al_2O_3 layer was deposited on the top of the annealed BTO film. For this BTO-Al_2O_3 stack, relative dielectric constant is 50 at E = 0 at RT. Leakage current is as low as ~10^{-8} A/cm^2 at E=0 at RT and 125°C.

[00163] ALD-growth of the BTO on TiN-substrates using a seed BTO layer

[00164] For seed layering, a thin BTO-seed layer of three different thicknesses (4 nm, 6 nm, 9 nm) was deposited on the TiN-coated substrates and annealed at a 900°C or 950°C for 3 sec. Short annealing time was intentionally applied to avoid the oxidation of TiN bottom electrode. While there is no sign of crystallization of the 4-nm and 6-nm BTO-seed layers even after annealing at 950°C in their XRD scans, weak (110) and (200) peaks indicate the onset of crystallization of the 9-nm thick BTO-seed layer after annealing at 900°C for 3 sec (FIG. 26a). Indeed, well defined (110) peak in the XRD scans for the main BTO film

deposited on the top of the 4-nm and 6-nm thick layers demonstrates the formation of the BTO phase in the film after annealing at 850°C for 3 sec (FIG. 26b).

[00165] We also deposited BTO-Al_2O_3 stacks over the annealed BTO-seed layers. Two stacking sequences for the BTO-Al_2O_3 structure were used: 1) bottom 3-nm Al_2O_3 + top 17-nm BTO layer; 2) bottom 17-nm BTO layer + top 3-nm Al_2O_3 layer. All BTO-Al_2O_3 stacks were deposited in one-step ALD growth procedure. After the deposition, whole structure was RTP annealed at 900°C for 3 sec in N2 flow. The XRD scans is clearly demonstrate well defined (100), (110), (111) and (200) peaks for both stacking sequences, indicating the formation of the BTO phase. Crystallization happens in the film with top Al_2O_3 layer. This is unexpected result, as typically XRD shows no sign of crystallization of the BTO layer with top Al_2O_3 layer.

[00166] Characterization and electrical testing of the Al_2O_3-BTO-Al_2O_3 tri-layer composite stacks on TiN-substrates

[00167] Fabrication of the TiN-Al_2O_3-BTO-Al_2O_3–TiN MIM-capacitors proceeds according to the steps presented in FIG. 28. First, we deposited a 2.5-nm thick Al_2O_3 layer and ~26-nm thick Ba-Ti-O on TiN substrate and cleaved the as-deposited film into four pieces. The four pieces were RTP annealed at 850°C for 1 min, at 900°C for 10 sec, for 1 min and for 2 min, respectively. In all cases, a heating rate was 10°C/sec. After the annealing step, another 2.5-nm thick Al_2O_3 layer was deposited. For MIM-capacitors, TiN top electrodes of ~45 nm thickness and a square base area of 90 × 90 μm2 were deposited utilizing a standard photolithography process and sputtering at room temperature.

[00168] The XRD data show a pure BTO phase on the Al_2O_3-BTO-Al_2O_3 structures annealed at 850°C for 1 min and at 900°C for 10 sec, while it demonstrates the presence of additional phases in the structures annealed at 900°C for 1 min and at 900°C for 2 min. The representative Grazing Incidence XRD (GIXRD) scans are presented in FIG. 29.

[00169] Crystallization of BTO is shown in the trilayer structure annealed at 900°C for 10 sec. This is reflected in the XRD scan (in black color) with a strong (110) peak at ~32° in 2θ and weak (100), (111) and (200) peaks at ~23°, ~38° and 44°, respectively. The XRD scan for the structure annealed at 900°C for 1 min (in red color) shows a weak (110) peak from BTO phase and two peaks at 25° and ~28° (denoted with arrows) from the secondary phase(s).

[00170] Annealing at 900°C for 10 sec at a heating rate of 10°C/sec results in the XRD peaks of higher intensity (accounting for signal-to-noise) compared to that for sample annealed at 900°C for 3 sec at a heating rate 50°C/sec (XRD scan in blue color). Without being bound to any particular theory, a lower heating rate and a longer annealing time at 900°C may improve crystallization of the BTO phase.

[00171] The electrical properties under applied electric field for two representative Al_2O_3-BTO-Al_2O_3 structures are shown in FIG. 30. We notice that dielectric constant at $E = 0$ is ~70 for the structure annealed at 850°C for 1 min, while it is ~60 for the structure annealed at 900°C for 10 sec. For comparison, data for the 28-nm thick BTO-Al_2O_3 stack annealed at 850°C for 3 sec at a heating rate 50°C/sec are also shown. It can be seen that at 6.3V the structure annealed at 850°C for 1 min exhibits the highest dielectric constant which is 45. Leakage current was quite low at $E = 0$. It should be noticed that leakage current is one order of magnitude lower at a magnitude of 1 MV/cm for the Al_2O_3-BTO-Al_2O_3 tri-layer stack annealed at 850°C for 1 min at a heating rate 10°C/sec.

[00172] The asymmetric shape of the J-E dependence in this case reveals the effect of the interface between TiN top electrodes and the Al_2O_3-BTO-Al_2O_3 structure. On the positive bias side, the leakage current is practically the same for this structure and for the 28-nm thick BTO-Al_2O_3 stack annealed at 850°C for 3 sec at a heating rate 50°C/sec. Thus, the lower heating rate and longer annealing does not reduce leakage current. On the other hand, we observe the influence of the metal-dielectric interface that results in reduction of leakage current at a factor of 10. Moreover, contraindicated tendency of the dielectric constant and leakage current behavior (dielectric constant goes down while current goes up) for the $Al2O_3$-BTO-Al_2O_3 structure annealed at 900°C for 10 sec. compared to the Al_2O_3-BTO-Al_2O_3 structure annealed at 850°C for 1 min. indicates on the contribution of both internal interfaces, TiN-Al_2O_3 and Al_2O_3-BTO.

[00173] TEM study of the BTO-Al_2O_3 stacks with Al_2O_3 layer between BTO and TiN-substrate

[00174] Previous measurement revealed that the BTO film on TiN-substrate (which has a 20-nm thick TiN sub-layer over Si-substrate) has higher thickness than expected according to the XRR measurement of the BTO film on pure Si-substrate. The additional thickness could arise from penetration of oxygen atoms into TiN-substrate with sequential formation of TiO_2 phase with the higher unit cell volume than TiN. We performed TEM

measurement in order to check the presence of TiO_2 phase and the quality of TiN-Al_2O_3 interface.

[00175] Shown in FIG. 31 are bright-field (BF) images of amorphous Ba-Ti-O films on TiN-substrates with Al_2O_3 layer between TiN-substrate and BTO. Two samples were prepared, by one-step and two step deposition process. As seen from FIG. 31, a two-step prepared film has a thicker (23.7 nm vs 23.2 nm) TiN sub-layer. This can be explained by the higher degradation degree of this film during the two-step process, as a total exposure time at elevated temperature (350°C) is longer. We note that in the case of a one-step process, the Al_2O_3 layer has much sharper interfaces with both TiN sub-layer and BTO film with little interdiffusion of Al_2O_3 into the BTO film and TiN sub-layer. Without being bound to any particular theory, this may help to preserve properties of both materials.

[00176] FIG. 32 represents STEM high-angle annular dark field (HAADF) and BF images of BTO films. High Z-contrast of this type of imagining reveals that the top area (denoted as Ti-N-O) amounting to ~40% of the total thickness of the TiN sub-layer has a lower electron density than the bottom area. This result can be explained by the fact that the average distance between relatively heavy Ti ions is increased because of penetration of oxygen atoms into interstitial spaces of TiN lattice.

[00177] We performed selected area electron diffraction (SAED) of TiN sub-layer in order to clarify phase composition of this layer. The electron diffractograms displayed (FIG. 33) reveal only crystalline TiN phase, and no TiO2 phase was found. The quality of diffraction pattern is practically the same for one-step and two-step process, but close inspection reveals that the TiN lattice reflections in one-step prepared film have a somewhat better defined shape indicating on better overall quality of the TiN sub-layer.

[00178] We also collected EDS line scans in the direction perpendicular to the interfaces (FIG. 34). This line scans clearly show that oxygen penetrates into TiN sub-layer in both samples from the side of Al_2O_3-BTO stack almost up to half of the thickness of TiN film. Aluminum spectrum shows a tighter shape for the case of one-step deposition process which is consistent with our previous observations.

[00179] Briefly summarizing results, the combined effects of lower heating rate and longer annealing time in the RTA procedure improves the crystallization of the BTO phase. Due to better crystallization, dielectric constant increases to some extent. Analysis of the

electrical tests and TEM data allow us to conclude that the quality of the interface between TiN substrate and BTO-Al_2O_3 stack has a primary effect on the leakage current.

[00180] Specifically, a substantial fraction of oxidized area (~40%) of the TiN-substrate that evolves during the ALD deposition process at 350°C. Interfacial defect states formed in this area reduce the quality of the interface and prevent a decrease in leakage current. Thus, while the lower heating rate and longer RTP annealing time together improve BTO crystallization, it appears that they lead to even more oxidization of the TiN-substrate, and therefore leakage current remains unchanged.

[00181] Characterization and electrical testing of the BTO films and Al_2O_3-BTO stacks with a seed BTO layer on TiN-substrates

[00182] For seed layering, a thin BTO-seed layer of two thicknesses, 6 nm and 9 nm, was deposited on the TiN substrates and RTP annealed at 900°C for 3 sec. Short annealing time and a heating rate 50°C/sec were intentionally applied to avoid the oxidation of TiN bottom electrode. While there is no sign of crystallization of a 6-nm BTO-seed layer, weak (110), (111) and (200) peaks indicate the onset of crystallization of the 9-nm thick BTO-seed layer after annealing at 900°C for 3 sec (black scans in FIG. 35). A weak (110) peak in the XRD scan for the main 24-nm thick BTO film deposited on the top of the 6-nm seed layer demonstrates a partial formation of the BTO phase in the film after annealing at 850°C for 3 sec (red scan in FIG. 35a).

[00183] We also deposited BTO-Al_2O_3 stacks over the annealed BTO-seed layers. Two stacking sequences for the BTO-Al_2O_3 structure were used: 1) bottom 2.5-nm Al_2O_3 + top 18-nm BTO layer; 2) bottom 18-nm BTO layer + top 2.5-nm Al_2O_3 layer. All BTO-Al_2O_3 stacks were deposited by one-step process. After the deposition, the whole structure was RTP annealed at 900°C for 3 sec in N_2 flow. The representative XRD scan (red in FIG. 35b) clearly demonstrates well defined (100), (110), (111) and (200) peaks for the stacking sequence with the Al_2O_3 layer located between bottom TiN electrode and the BTO film, indicating a well crystallized BTO phase. Interestingly, this crystallization also occurred in the film with Al_2O_3 layer located between BTO film and the top TiN electrode. This is an unexpected result, as typically XRD shows no sign of crystallization of the BTO layer with top Al_2O_3 layer.

[00184] The TiN-BTO-TiN and TiN-Al_2O_3-BTO-TiN MIM-capacitors based on the films using seed layering were tested for dielectric constant and leakage current at RT and

125°C. Representative data are displayed in Figs. 36 and 37. First, we notice that dielectric constant near E = 0 is higher for the TiN-Al_2O_3-BTO-TiN MIM-capacitor (60 vs 30 at RT and 75 vs 50 at 125°C). This results reflects better BTO crystallization for the TiN-Al_2O_3-BTO-TiN structure. The dielectric constant is almost the same for both MIM-capacitors, 43 and 47, under positive bias 6.3V at 125°C. The leakage current is excessively large.

[00185] Further testing results and analysis

[00186] Additional device-to-device variation testing has been performed for two most promising MIM structures that showed good results. The characteristic parameters initially identified for both structures and correspondent specifications are summarized in Table 2 below. The results are obtained using data collected on 3 devices for each structure.

	Thickness	Dielectric Constant	Leakage Current density
Annealed at 700°C, Pt-BTO-Al_2O_3-TiN	36	44	2.2×10^{-8} A/mm^2 at RT 5×10^{-7} A/mm^2 at 125°C
Annealed at 750°C, Pt-BTO-Al_2O_3-TiN	36	53	1.3×10^{-7} A/mm^2 at RT 2.5×10^{-6} A/mm^2 at 125°C

[00187] We collected electrical data on a statistically significant number of MIM-capacitors, specifically on 20 and 22 devices for BTO-Al_2O_3 composite structure annealed at 700°C and 750°C, respectively. For all MIM-structures the bottom electrode is Pt and the top electrode is TiN. These data are displayed in Figs. 11-13. Analyzing statistical data for dielectric constant (ε) and losses $(\tan\delta)$ collected at 100 kHz (FIG. 11), the Average ± Standard Deviation values have been determined as following: e = 90 ± 7 and e = 116.6 ± 5, $(\tan\delta) = 0.15 \pm 0.03$ and $(\tan\delta) = 0.0288 \pm 0.0044$ for structures annealed at 700°C and 750°C, respectively.

[00188] In FIG. 12 the room-temperature leakage current density as a function of process conditions for these MIM-capacitors are displayed. The different annealing conditions were: i) 700°C+ 4-nm Al_2O_3 and ii) 750°C+ 4-nm Al_2O_3: subsequent annealing for 10 min under N_2 flow in tube furnace, followed by the growth of 4-nm Al_2O_3. It can be clearly seen in FIG. 39a that the leakage current is asymmetric. This asymmetry most likely arises due to two-step ALD-growth, as first the BTO film was deposited and annealed and then Al_2O_3 layer was deposited. As a result, interface defects and contamination layer introduced at the film surface. However, the data for positive bias are expected to be representative for the properties of the MIM-stacks. In FIG. 39b the positive bias is shown.

Analyzing statistical data for leakage current density at 1 MV/cm under positive bias (FIG. 39), the Average ± Standard Deviation values have been determined to be $5.58*10^{-7}$ ± 10-7 A/cm^2 and $1.07*10^{-5}$ ± $2*10^{-6}$ A/cm^2 for the MIM-structures annealed at 700°C and 750°C, respectively.

[00189] Device-to-device reproducibility was present. Specifically, dielectric constant varies at 7.7% and 4.3%, and leakage current density (at 1 MV/cm) varies at 17.9% and 18.7% for Pt-BTO-Al_2O_3-TiN MIM-capacitors annealed at 700°C and 750°C, respectively. Significantly, even with this variation the MIM caps annealed at 700°C yield results that are better than the 10^{-8} A/mm^2. These results are not only the best reported combination of low-leakage and high dielectric permittivity for a thin-film polycrystalline ceramic; further, variation in their properties is not unreasonable given that the data are collected on initial laboratory-scale devices.

[00190] Our results demonstrate that several factors can be important for minimizing increases in leakage that arise during annealing, including, e.g., preserving the integrity of the BTO-metal interface, and limiting annealing to a single step. We expect that leakage involving all TiN-electroded BTO-Al_2O_3 capacitors can be reduced with additional investigation beyond the limited budget and scope of the present project (e.g., dielectric stoichiometry and phase, seed layer procedure, number of annealing steps, annealing atmosphere and flow rates, time-temperature profile, number of layers and respective thicknesses).

[00191] Additional Disclosure

[00192] Atomic layer depositions of semi-amorphous $Ba(OH)_2$-TiO_2 laminates of ~50 nm total film thickness on Pt(111)/Ti/SiO_2/Si(100) substrates (Gmek Inc.) were conducted in a Picosun R200 Advanced Reactor. The cation-precursors were Absolut Ba (Air Liquide, $Ba(iPr_3Cp)_2$), kept at 473 K, and titanium-isopropoxide (Alfa Aesar, $Ti(iOPr)_4$), kept at 388 K. For both of them H_2O, kept at room temperature, served as reactant. High purity N_2 gas (99.9999 %) was used as carrier gas and the growth temperature was 563 K. The pulse and purge times were 1.6/6 s for $Ba(iPr_3Cp)_2$ and 0.1/10 s for H_2O for the Ba-O subcycle, and 0.3/1 s for $Ti(iOPr)_4$ and 1/3 s for H_2O for the Ti-O subcycle. An initial 12 Å thick layer of TiO_2 was deposited on all substrates to improve uniformity.

[00193] In order to vary the overall composition of the films, the repeat number for the Ba-subcycle was kept constant, while the repeat number for the Ti-subcycle was varied

between 42 and 55. A sequence of 10 total repeat units of alternating subcycles, as described previously, resulted in a total film thickness of ~ 50 nm.

[00194] Metal-insulator-metal (MIM) capacitors were produced by depositing ~80 nm thick 90 x 90 μm^2 squares of Pt before or after (for one stoichiometric sample) annealing, utilizing photolithography and sputtering at room temperature. *Ex-situ* annealing under an over-pressure of 5 psi O_2 was conducted using the following annealing sequence: the samples were heated to 1023 K with a rate of 4 $K \cdot min^{-1}$, kept at 1023 K for 12 hours, cooled to 353 K at a rate of 1 $K \cdot min^{-1}$. A subsequent step with heating to 433 K (3 $K \cdot min^{-1}$) followed by cooling to 373 K at a slow rate of 0.5 $K \cdot min^{-1}$ was applied to ensure a slow cooling through the Curie temperature of bulk $BaTiO_3$ (T_C=396 K).

[00195] The grazing incidence X-ray diffraction (GI-XRD) scans were performed on a Rigaku Smartlab using Cu-K_α radiation. The lattice parameters were extracted from least squares fits utilizing the WinCSD program package.

[00196] Cross-sections of the MIM-capacitors for high resolution transmission electron microscopy (HR-TEM) were prepared in a Helios Nanolab 600i (FEI, USA) Scanning Electron Microscope (SEM)/Focused Ion Beam (FIB) dual beam system equipped with gas injectors for W and Pt deposition and an Omniprobe micromanipulator (Omniprobe, USA). After depositing a 2 µm thick protective Pt layer, milling using a 30 keV Ga^+ ion beam resulted in a cross-section area of 5 × 5 μm^2, which was subsequently polished with 5 keV and 2 keV Ga^+ ion beams, respectively. These MIM-cross sections were investigated utilizing a Titan 80–300 operated at 300 kV, which is equipped with a high-angle annular dark-field (HAADF) detector (Fischione, USA), a spherical aberration (C_S) probe corrector and a post-column Gatan image filter (GIF). Digital Micrograph (Gatan, USA) and Tecnai Imaging and Analysis (FEI, USA) software were used for the image processing.

[00197] X-ray photoelectron spectroscopy (XPS) measurements were conducted using a Physical Electronics VersaProbe 5000 under a base-pressure of ~10^{-6} Pa. An Al-Kα source provided incident photons with an energy of 1486.6 eV at 10 kW mm^{-2}. The XPS spectra were collected with the pass energy of 23 eV. An electron neutralizer was used to neutralize the surface. Linear energy correction was applied in reference to the carbon spectra. The energy of the C1s peak of non-oxidized carbon was set at 284.8 eV. The detector was placed at the angle of 87.2° relative to the surface in order to collect the XPS signal from a larger volume of the films. For MIM-capacitors, TiN top electrodes of 45 nm thickness, a

resistivity of 300-400 μΩcm, and an area of 90 × 90 μm2 were deposited at a power of 450 W utilizing a standard photolithography process and sputtering at room temperature for the 30 nm thick NP/BTO films and NP/BTO-Al2O3 bi-layer structures of stacking sequence shown in FIG. 40, grown on Pt(111)/Ti/SiO2/Si(100) substrates after annealing

[00198] The electrical properties of the MIM-capacitors were measured in a probe station (Lakeshore Cryotronics TTP4) utilizing a Keithley SCS-4200 electrometer for collecting frequency dependences (10kHz - 1MHz) of capacitance & loss tangent and a Precision Tester (Radiant Technologies, Inc.) for collecting polarization hysteresis loops. The measurements were performed in air at room temperature and under vacuum of ~10^{-5} Torr over a temperature range of 190–420 K, on cooling and heating, at a constant rate of 5 K min^{-1}.

[00199] Raman spectra were collected in backscattering configuration $z(x, x+y)\bar{z}$ using a single monochromator (XploRA, Horiba Jobin-Yvon, Edison, NJ) and a laser (4 mW, λ = 532 nm) focused to a spot diameter of ≈10 μm at an intensity of 1.6×10^3 W cm^{-2}. Light was dispersed using a 2400 gr mm^{-1} grating and collected using a Peltier-cooled array detector. The sample temperature was varied from 123 K to 473 K (Linkham THMS 600, instrumental precision ±0.1 K) in increments of 5 K at a heating ramp rate of 5 K min^{-1}. The sample is also allowed to equilibrate for 1 min between consecutive Raman scans.

[00200] Material characterization

[00201] Four BTO thin films with varying Ba/Ti ratio were grown by ALD and were characterized by XRD, RBS, TEM, XPS, and Raman scattering techniques. Details on the structural characteristics of the samples are provided elsewhere.

[00202] Room-temperature X-ray diffraction scans, collected after the annealing step reveal the presence of polycrystalline BTO in the perovskite structure for all samples and, independent of the composition, no additional peaks are detected. The GI-XRD patterns point towards a cubic symmetry or a marginal tetragonal distortion. However, Raman spectra clearly show the tetragonal symmetry for the perovskite in coexistence with the hexagonal BTO polymorph within all thin film samples. The Ba/Ti-ratio values have been determined using RBS measurements. The details of the RBS analysis are provided elsewhere. FIG. 40 shows the lattice parameters, which were extracted from least squares fits to the cubic perovskite structure (SG: $Pm\bar{3}m$). A lattice expansion of 0.2 % with increasing Ba/Ti-ratio is

observed. The mean values and standard deviations of crystallite sizes determined from the Gaussian fittings (FIG. 50) of the distribution of sizes obtained from TEM images are also depicted in FIG. 40. Detailed TEM investigations have been performed for all films, which had top Pt electrodes deposited *before* the annealing procedure. The results of this study (see Ref. 42 for details) imply that an extended metastable solubility range exists for the perovskite-phase on both sides of the stoichiometric composition. The absence of any additional secondary phases besides the hexagonal polymorph, together with the lack of cation segregation at the grain boundaries and film-substrate interfaces confirm that the off-stoichiometry is accommodated within the BTO crystallites. Moreover, the independence of the ratio of hexagonal to perovskite polymorph to the Ba/Ti-ratio and the systematic change of the lattice parameter indicate that cation defects are located in the perovskite phase.

[00203] In the present work, we additionally investigated a stoichiometric (Ba/Ti=1.01) sample by TEM, where the *top electrodes* were deposited *after* the annealing process. A cross section of the MIM-capacitor was examined between the top and bottom Pt electrodes to unravel the influence of the presence/absence of a top electrode during the annealing process on the crystallite size and resulting physical properties. FIG. 41 shows representative BF-TEM images for two stoichiometric (Ba/Ti = 1.01) samples, one with *top electrodes* deposited *before* annealing (FIG. 41a) and the other one with *top electrodes* deposited *after* annealing (FIG. 41b). The distribution of crystallite sizes obtained from the TEM images for each sample and their fitting are presented in Figs. 50 and 51, respectively. As expected, the comparative analysis indicates that the crystallite growth is suppressed by the presence of a top electrode during the annealing process. While the distribution of crystallite sizes is fitted by one Gaussian function with a mean value of 12.1 nm for sample with electrodes *before* annealing, the size distribution is fitted by two Gaussians, with the mean values of 12.0 and 35.0 nm sizes for sample with electrodes *after* annealing. In addition, the cross section between the free area (no top electrodes) and bottom electrode obtained for a stoichiometric sample was also analysed. The distribution of grain sizes obtained from TEM images of this cross section and the fitting are presented in FIG. 52. For this case, the main value of crystallite size is 17.1 nm. Below is described how the difference in crystallite size affects the ferroelectric phase transition.

[00204] The valence states of Ti and Ba and their possible change with compositional variation have been probed by XPS. The Ti and Ba spectra and their fitting are

presented in the Supporting Information. FIG. 53 unambiguously demonstrates that Ti in the oxidation state 4+ is present in all films independent of composition. The XPS Ba spectra collected for the films with various Ba/Ti ratios, displayed in FIG. 54, show that the Ba3d5/2 peak contains two lines, corresponding to the Ba^{2+} ions located in deeper layers of the films and on the surface with a shift to higher energy.

[00205] The intensity of the line originating from the Ba^{2+} ions from the bulk of the films monotonically increases, while the intensity of the line corresponding to the Ba^{2+} on the surface systematically decreases with increasing Ba/Ti ratio. Independent of the composition, no recharging effects of the cations is observed.

[00206] Dielectric study

[00207] Frequency dependences (from 10 kHz to 1 MHz) of the capacitance and loss tangent were collected within temperature intervals of 190 K<T<420 K for the films with Ba/Ti ratios of 0.8, 0.92 and 1.01, and between 250 K and 420 K for the film with a Ba/Ti ratio of 1.06. First, the samples were cooled down from room temperature to 190 K/250 K, followed by heating up to 420 K and a subsequent cooling to room temperature. A negligible frequency dependence of the permittivity and loss tangent was observed within the investigated temperature intervals for all samples. Representative temperature dependent data obtained at 100 kHz for four samples with the top Pt electrodes deposited before the annealing procedure are depicted in FIG. 42. In all cases, the dielectric constant is normalized to its maximum value e_m. The absolute maxima of the dielectric constant and temperature extracted from the cooling and heating cycle are summarized in Table 1. As displayed in FIG. 42a, the samples exhibit a broad non-monotonic dependence with hysteretic behaviour. The maximum permittivity shifts from 212 K to 350 K for cooling and from 230 K to 355 K for heating as the Ba/Ti ratio increases from 0.8 to 1.06, respectively. The temperature dependence of the dielectric loss (tanδ) reveals a distinctly different behaviour for each composition (FIG. 42b).

[00208] While a broad, but at the same time, rather pronounced maximum around 200 K for a Ba/Ti ratio of 0.8 is present, this maximum becomes smoother with increasing Ba-content and practically vanishes at the stoichiometric composition. However, in the Ba-rich sample the scenario is vastly different as the loss tangent not only increases with temperature, but is in general higher than for all other samples. This behaviour might indicate (without being bound to any particular theory) the segregation of space charges at grain

boundaries. Considering the formation of Schottky defects as the main source for off-stoichiometry, the amount of oxygen vacancies is higher in Ba-rich than in Ti-rich sample (see equations (2) and (3) below), so space charges might form more readily in this case. To further consider the influence of the leakage current on the temperature behavior of losses, we provide the electric field dependences of current density (J-E) for the films with different Ba/Ti-ratio. The dependences depicted in FIG. 55a demonstrate that the films with different stoichiometry are basically identical in their J-E response, so there is no correlation between the J-E behavior and features in FIG. 42b for the film with Ba/Ti=1.06.

[00209] The maximum in ε(T) is indicative of a phase transition in ferroelectric materials. The total shift of the peak temperature T_m over the studied frequency range cannot be clearly determined because of its broad occurrence. Nevertheless, it is worth mentioning that the weak frequency dispersion of T_m should still be present due to the diffuse type of the transition as described below. Since ε(T) exhibits thermal hysteresis, a first-order ferroelectric phase transition should be present, which is similar to bulk BTO. A progressive reduction of the hysteresis with increasing Ba/Ti ratio is observed. The hysteresis exhibits the largest value of 18 K for the most Ti-rich sample (Ba/Ti = 0.8), continuously decreases to 10 K for the nearly stoichiometric sample (Ba/Ti = 1.01) and ultimately shrinks to 5 K for the most Ba-rich sample. Compared to the single-crystal counterparts and larger grain ceramic specimens with stoichiometric composition, the transition temperature drops dramatically. This decrease of T_C may relate to the reduced crystallite sizes, as analogous shifts in the ferroelectric transition temperature were observed in a number of ceramic and thin film samples: e. g., the T_C was registered at 379 K for 50-nm and 30-nm ceramic samples and at 333 K for grain sizes of 22 nm. In analogy, the decrease of the Curie temperature was reported for polycrystalline BTO films as a function of the film thickness and grain size.

[00210] To probe how the crystallite size affects the temperature behaviour of dielectric parameters for the present thin films, and thereby disentangle the size effect from a compositional effect, we also investigated the stoichiometric (Ba/Ti = 1.01) sample with the top electrodes deposited after the annealing step. In this case, the crystallites underneath the top electrodes are larger and the distribution of grain sizes is different from the sample, in which the top electrodes were deposited before the annealing procedure (see Figs. 50c and 51). This difference clearly shows that an additional layer on top of the thin film effectively reduces the grain growth compared to an unconfined film surface. FIG. 43 reveals the

presence of two peaks in in ε(T) and tanδ(T) dependences for the MIM-capacitor with the top electrodes deposited after the annealing step. The first peak is observed around T_m = 330 K and the second one at T_m = 390 K. The dependences can be considered as frequency independent, although they exhibit a very broad transition region and, therefore, a diffuse type phase transition. A comparison between the grain size distributions for the samples with top electrodes before and after annealing allows us to attribute these maxima to the phase transitions for crystallites of two groups, with smaller (average 12 nm) and bigger (average 35 nm) sizes.

[00211] The bigger grains are also clearly visible in the TEM image displayed in FIG.41b and the wide grain size distribution results in the very broad phase transition region displayed in FIG. 43. It should be noted that the peak at higher temperature (T_m = 390 K) is very close to the Curie temperature for bulk samples (T_C = 396 K), and the peak at lower temperature (T_m = 330 K) can be associated with a decreased T_C due to the crystallite size reduction and is very close to T_m = 315-325 K for the sample with *top electrodes* deposited *before* the annealing step. This comparison allows us to independently discern the crystallite size effect and hereby confirm that the change of the transition temperature observed for the samples with different Ba/Ti ratio (see FIG. 42a and Table 1) is predominantly caused by the different compositions. Thus, we reveal a shift in the transition temperature of ΔT = 138 K due to the variation in the cation ratio from 0.8 to 1.06.

[00212] Taking into account similar fabrication conditions, film thicknesses, and grain sizes (see FIG. 40) for all four samples, it may be that the deviation of the transition temperature is correlated to the variation of stoichiometry. Such an increase of the Curie point, ΔT = 120 K, due to variation of the Li/Nb ratio from 0.96 to 1.04, has been observed earlier in $LiNbO_3$ crystals.[48] A smaller increase of T_C, about 10 K, due to variation of Ba/Ti ratio from 0.99 to 0.999 has been demonstrated in ceramic BTO samples. Compared to BST ceramics, this large shift in Curie temperature corresponds to a change in the Ba/Sr-ratio of more than 50%. Before discussing which microscopic mechanisms could provoke this effect, below is discussed the behaviour of the dielectric constant.

[00213] Table 1. Maximum temperature, T_m, and dielectric constant, ε_m, extracted from experimental temperature dependence for the four films with top electrodes deposited *before* annealing. Parameters Δ and ξ from least square fits to equation (1)

Ba/Ti ratio	T_m on cooling/heating (K)	ε_m on cooling/heating	Δ (K)	ξ
0.8	212 / 230	84.6 / 84.6	650 ± 6	2
0.92	258 / 275	110.7 / 110.9	593 ± 5	2
1.01	315 / 325	168.6 / 169.3	588 ± 6	2
1.06	350 / 355	163 / 163.8	565 ± 10	2

[00214] The decrease of T_C because of grain size reduction is typically accompanied by the broadening of the maximum and decreasing of the dielectric constant. Table 1 shows how the maximum dielectric constant, ε_m, changes with composition variation. The room temperature dielectric constant as a function of frequency for the films with Ba/Ti=0.8, 0.92, 1.01 and for the film with Ba/Ti=1.01 with top electrodes after annealing is depicted in FIG. 55b. The room temperature dielectric constant depends on stoichiometry, especially on the Ti-rich side. It is reduced by 50% in the Ti-rich samples compared to the stoichiometric one, but remains almost unchanged upon further increasing the Ba/Ti ratio. In the present work, the same trend is observed for ε_m from the temperature dependence of the dielectric constant. As noted above, the phase transition in fine grained samples is very broad and is therefore coined a diffuse phase transition (DPT). A simple and explicit model qualitatively and quantitatively describing the temperature dependence of the dielectric permittivity at the DPT was suggested:

$$\varepsilon = \frac{\varepsilon_m}{1+((T-T_m)/\Delta)^{\xi}} \quad (1)$$

where Δ and ξ are empirical parameters related to the transition diffuseness and to the character of the phase transition, respectively. The parameter ξ is the peak broadening that indicates the degree of diffuseness. The parameter ξ can take values between 1 for a typical ferroelectric behaviour and 2 for the so-called "complete" DPT. The solid curves depicted in FIG. 42a are fitting results to equation 1. All data are best fitted with a parameter ξ=2 and the parameters Δ shown in Table 1. A slight, gradual decrease of the diffuseness degree with increasing Ba/Ti ratio is seen.

[00215] Due to the wide distribution of grain sizes, there is a range for the T_C in a DPT, so the peak temperature T_m can be regarded as an average T_C (correlated to the average grain size). Keeping this in mind, we use the term phase transition temperature for the peak temperature.

[00216] Accounting average grain sizes of 8-12 nm in all compositions (see FIG. 40), we approach the ferroelectricity limit. Indeed, FIG. 44a shows an extremely narrow hysteresis loop collected at 300 K at 500 Hz. We observe here that the polarization changes as a function of Ba/Ti ratio in a similar manner as the dielectric constant (see Table 1). The values of both, maximum polarization P_{max} (at E = 0.545 MV/cm) and remnant polarization P_{rem} drop by almost 50% for the Ti-rich samples and only slightly decrease in the Ba-rich sample compared to the stoichiometric one. FIG. 44b presents the temperature behaviour (heating cycle) of the values of maximum and remnant polarization as a function of Ba/Ti ratio.

[00217] While P_{max} remains almost unchanged over the phase transition region for all compositions, P_{rem} exhibits a non-monotonic behaviour with a weak and wide hillock around T_m for the Ti-rich films (Ba/Ti = 0.8, 0.92) and with more pronounced and narrower maxima for the stoichiometric and the Ba-rich (Ba/Ti=1.06) samples. Considering practically similar grain sizes for all compositions, such a difference indicates that the latter two films contain more crystallites with stable domains or domain structure, which contribute to the polarization in zero electric field. These crystallites are likely more strained and therefore should have a higher ratio of tetragonality (c/a) or lower symmetry.

[00218] Furthermore, the remnant polarization, although approaching zero at elevated temperature, does not vanish above T_m for these two samples, implying that there are residual strains in the vicinity of the DPT on the high-temperature side that preserve the polarization within the grains. For Ti-rich samples, the remnant polarization remains almost zero over the entire temperature region. Therefore, the samples are expected to have more strain relaxed crystallites with minor or no distortion from cubic symmetry (c/a->1). The room-temperature hysteresis loop for the stoichiometric sample with top electrodes deposited after the annealing step is displayed in FIG. 45. While the maximum polarization for this film is similar, the remnant polarization is enhanced by a factor of 3 compared with the same sample with top electrodes deposited before annealing (FIG. 44). This difference most certainly arises from the presence of larger crystallites within this thin film.

[00219] We show the J-E response for the stoichiometric film (Ba/Ti=1.01) with top Pt electrodes deposited after the annealing step in FIG. 55a in the revised SI. This figure indicates that leakage current for this film is higher than that for the stoichiometric film with top Pt electrodes deposited before annealing.

[00220] However, the difference between FIGs. 44 and 45 is not explained by the influence of leakage current. We provide the hysteresis loops collected at different electric fields and different frequencies depicted in FIGs. 56 and 57 and show that in the hysteresis loop presented in FIG. 45 is measured at optimal conditions when the influence of the leakage current is almost negligible. FIGs. 56 and 57 represent room temperature hysteresis loops collected for the stoichiometric (Ba/Ti=1.01) film with Pt electrodes deposited after the annealing step. The hysteresis loops were measured at different maximum electric fields and different measuring frequencies. The hysteresis loop measured at a maximum electric field of 0.65 MV/cm and a frequency of 1 kHz exhibits a maximum polarization of 7.5 μC/cm2, while the influence of the leakage current is negligible there. This representative hysteresis loop is shown in FIG. 45.

[00221] From a microscopic point of view, the shift of the ferroelectric transition temperature in BTO is a strain/stress mediated phenomenon for any kind of effect (including any interfacial and gradient effects). Contrary to epitaxial films, the strain due to the lattice mismatch between substrate and film has a negligible influence on the structure of polycrystalline BTO films. As TEM images show (see FIG. 41), the crystallites within all films are randomly oriented, so no preferential alignment occurs. This fact is further corroborated by XRD data that show the polycrystalline nature of all thin films. Moreover, as the growth and annealing conditions were kept identical for all samples, we assume that the strain induced by the thermal expansion mismatch between substrate and film is equivalent for all films. With respect to the compositional gradient effect, we refer again to the microstructure analysis and further note that no cation segregation at the grain boundaries is observed from TEM. Therefore, we focus on the impact of the composition hereafter.

[00222] For compositional effects within the lattice the strain arises from the defects formed during the crystallization of BTO, so called *Vegard strain* (or chemical pressure).

[00223] In off-stoichiometric BTO the following types of partial Schottky defects are typically considered

Ti-rich side: $TiO_2 \xrightarrow{BaTiO_3} Ti_{Ti}^{X} + 2O_O^X + V_{Ba}'' + V_O^{\bullet\bullet}$ (2)

Ba-rich side: $BaO \xrightarrow{BaTiO_3} Ba_{Ba}^{X} + O_O^X + V_{Ti}'''' + 2V_O^{\bullet\bullet}$ (3)

[00224] Now we estimate the strain due to the presence of partial Schottky defects, with respect to stoichiometric deviations in the chemical formula. For this purpose, we use the results of calculations made by Freedman *et al.* for strontium titanate (STO).[52] Since BTO

is very similar to STO in terms of chemical bonding, the perovskite crystal structure, and lattice parameters, the estimation of the chemical strain in BTO using these results seems appropriate. The local strains imposed by different defects such as oxygen vacancies (V_O), strontium vacancies (V_{Sr}), titanium vacancies (V_{Ti}), strontium-oxygen divacancies (V_{Sr}-V_O), and titanium-oxygen divacancies (V_{Ti}-V_O) determined in the literature are provided in Table 2. Here, ε_c is the chemical strain ($\Delta a/a$), and δ denotes the deviation from stoichiometry that specifies the number of defects per chemical unit. Positive Vegard strain results in lattice expansion, and negative Vegard strain in lattice contraction.

[00225] Table 2. The ratio of the chemical strain to stoichiometric defect deviation δ for $Sr_1TiO_{3-\delta}$, $Sr_{1-\delta}TiO_3$, $SrTi_{1-\delta}O_3$, $Sr_{1-\delta}TiO_{3-\delta}$, and $SrTi_{1-\delta}O_{3-\delta}$ (D. A. Freedman, D. Roundy and T. A. Arias, *Phys. Rev. B*, 2009, 80, 064108.)

	V_O	V_{Sr}	V_{Ti}	V_{Sr}-V_O	V_{Ti}-V_O
ε_c/δ	+0.001	+0.030	+0.402	-0.008	+0.260

[00226] Our Ti-rich samples can be treated as $Ba_{1-\delta}TiO_{3-\delta}$, while Ba-rich samples as $BaTi_{1-\delta}O_{3-2\delta}$ in accordance with equations (2) and (3), respectively. First we estimate the contribution of the partial Schottky defects to the strain. For this, we calculated the strain ε_c which should be created if a) only isolated vacancies are introduced, and b) if only divacancies (and additional V_O for Ti-deficient films to maintain charge balance) are introduced. For the stoichiometric composition ($\delta = 0$) we assume an unstrained state ($\varepsilon_c = 0$).

[00227] The calculated strain versus Ba/Ti ratio is displayed in FIG. 46. The strain determined using the lattice parameters from XRD data (see FIG. 40) is also depicted in FIG. 46. A pseudo-cubic lattice parameter for stoichiometric BTO, a_{pc}=4.007 Å (this is an average value for the tetragonal structure, where a=3.992 Å and c=4.036 Å) was used. In addition, the variation of the phase transition temperature (bars indicate the T_m values on cooling and heating taken from Table 1) as a function of the Ba/Ti ratio is presented in FIG. 46. The dependence for T_m follows a linear relation as indicated by a least-squares fit.

[00228] Comparison of the estimated values of the strain with experimental values allows us to conclude that the strain produced by divacancies exhibits a similar trend as the experimentally observed strain with negative strain on the Ti-rich side and positive strain on

the Ba-rich side. However, the strain obtained using lattice parameters from XRD is smaller than the theoretically predicted strain arising from partial Schottky defects. For possible sources of strain relaxation, the following contributions could be considered: with respect to the internal stress at the grain boundaries, different mechanisms of its evolution were suggested, and there is not a consensus so far. Although many calculations show that the driving force for the internal tensile stress is surface energy reduction due to grain boundary formation, the measured value of this stress is much lower than that attributed to compressive stress due to insertion of additional atoms into the grain boundaries as a way to relax the tensile stress in the film.

[00229] We do not observe any segregation of cations at the boundaries from TEM, and therefore one can (without being bound to any particular theory) assume that quite high internal tensile stress is present in our samples. This suggestion is supported by the fact, that several polymorphs (cubic, tetragonal and hexagonal) are formed for all compositions due to the non-equilibrium state. This internal stress at the grain boundaries could facilitate the relaxation of the strain due to partial Schottky defects located inside crystallites. Regarding the second possible source, we observe compositional inhomogeneity from elemental mapping in TEM cross sections. This spatial off-stoichiometry likely occurs in order to lower the total energy and therefore might also relax the local strain induced by Schottky defects.

[00230] Raman scattering study

[00231] To complement the dielectric study, we conducted a detailed analysis of the Raman spectra collected in the temperature range from 123 K to 473 K (heating cycle) for the two thin films with lowest and highest Ba/Ti-ratio, 0.8 and 1.06, respectively. All spectra were collected in areas of the film surface between the top Pt electrodes. It should be mentioned that the Raman spectra for samples with top electrodes deposited before and after annealing are similar, which means that the microstructure between the top electrodes is basically identical independent of the top electrodes deposition procedure. FIG. 47 shows the room-temperature spectrum collected for the stoichiometric (Ba/Ti=1.01) sample which has top electrodes deposited before annealing. The spectrum demonstrates the presence of tetragonal (*t*-BTO) and hexagonal (*h*-BTO) polymorphs and is representative for all thin films used in this study. No peaks from impurity phases are visible. Note that a polymorphous mixture is frequently observed for polycrystalline BTO thin films and was also reported for nanoparticles with a size of 40 nm.

[00232] The temperature dependent Raman spectra collected for the samples with Ba/Ti-ratios of 0.8 and 1.06 qualitatively look similar to the room-temperature spectra displayed in FIG. 47. The wide band in the wavenumber range of 150-300 cm^{-1} contains several overlapped modes including the ~180 cm^{-1} peak assigned to the E_{2g} mode of *h*-BTO[58] and the ~280 cm^{-1} peak assigned to the $A_1(TO_2)$ mode of *t*-BTO. However, each of these peaks is not well isolated and has contributions of a few modes. Therefore, it is impossible to use these peaks for a meaningful analysis.

[00233] The 520 cm^{-1} peak primarily represents the $A_1(TO_3)$ component of the $A_1(TO)$ spectrum of *t*-BTO. As was shown recently, the frequency of the 520 cm^{-1} mode of *t*-BTO gradually decreases and its width broadens until the mode almost disappears above the ferroelectric transition in a polycrystalline BTO thin film. For the hexagonal polymorph a very prominent ~620 cm^{-1} peak is assigned to the A_{1g} mode. As seen in FIG. 47, the Raman spectra also contain a ~720 cm^{-1} peak, which represents the $A_1(LO_3)$ mode of *t*-BTO. This peak is broad and has a low intensity. Moreover, its frequency remains practically constant throughout the tetragonal phase. According to different studies, the soft mode in the perovskite BTO has two components: a doubly degenerate overdamped component $E(TO_1)$, the frequency of which varies within 35±5 cm^{-1}, and the half-width is 85–115 cm^{-1} and the totally symmetric component $A_1(TO_2)$ at a frequency of 280-308 cm^{-1}. While the overdamped component $E(TO_1)$ condenses very fast and becomes invisible approaching the ferroelectric phase transition, the frequency of the $A_1(TO_2)$ component remains almost unchanged with temperature in polycrystalline thin films.

[00234] In our Raman spectra, the situation is more complicated due to the presence of a polymorphous mixture in all samples. When a soft mode is overdamped or even unavailable in a material with structural disorder, it is appropriate to obtain information about the phase transformation by monitoring the temperature behaviour of the spectroscopic parameters of other modes, which are sensitive to the symmetry of the structure. Considering all these factors, we based the analysis on separately evaluating the temperature behaviour of the frequency, integrated intensity, and FWHM (full width at half maximum) for the 520 cm^{-1} (*t*-BTO) and 620 cm^{-1} (*h*-BTO) peaks. Bose-Einstein correction has been performed prior to the data analysis of structural phase transitions; in addition, fitting with a Lorentzian lineshape has been applied following the methodology described in detail previously.

[00235] FIG. 48 shows the temperature dependences of the spectroscopic parameters of the 520 cm^{-1} peak for the Ti-rich sample (Ba/Ti=0.8). As demonstrated, the frequency of the 520 cm^{-1} peak decreases non-monotonically from 532 cm^{-1} to 526 cm^{-1} as the temperature increases from 100 K to 320 K. The reduction rate sharply changes at ~212 K. Starting from this point, the frequency remains unchanged until ~230 K and continues to gradually decrease above 230 K. The integrated intensity displays an anomaly in the same temperature range, while the FWHM consistently increases over the entire temperature interval. All the features occur in the same temperature interval as the phase transition observed in dielectric measurements for this film. The temperature behaviour of the 620 cm^{-1} peak is not so distinct (see FIG. 58). Its frequency continuously increases and a slight change in the slope can be noticed in the interval from 212 K to 230 K. Other parameters, i.e. the width and integrated intensity, change marginally and monotonically, with no specific features detectable between 212 K and 230 K. Based on this analysis, one can conclude that the phase transition around 212-230 K revealed in the dielectric study is fully attributed to the structural transformation of the perovskite phase from tetragonal to cubic with increasing temperature, although the symmetry change marginally influences the dynamics of the *h*-BTO phase. Moreover, the extended temperature interval for this specific behaviour of the spectroscopic parameters for the 520 cm^{-1} mode, confirms the diffuseness of the phase transition.

[00236] FIG. 49 displays the frequency, integrated intensity and FWHM as a function of temperature for the 520 cm^{-1} and the 620 cm^{-1} peaks for the most Ba-rich thin film (Ba/Ti=1.06). Here, a significant change in the frequency behavior of the 520 cm^{-1} peak is observed over a wide temperature interval, from 350 K to 415 K. While the frequency decreases as temperature increases from 290 K to 350 K, it starts to raise at 350 K followed by a sharp drop at 415 K. The integral intensity and linewidth also experience non-monotonic changes in the same temperature range. While the decrease in the intensity slows down at 350 K and only drops a little between 350 K and 415 K, the FWHM sharply changes the behaviour, from increasing to decreasing, at 350 K and then changes the behaviour again, now from decreasing to increasing, at 415 K. The temperature behaviour of the 620 cm^{-1} peak for the Ba-rich sample exhibits a behaviour strongly correlated to the 520 cm^{-1} peak and even exhibits additional features. As one can see, all parameters have significant peculiarities in

the interval of 350 – 420 K. An additional anomaly occurs within this range, at ~400 K. This feature is observed for all spectroscopic parameters of the 620 cm^{-1} peak.

[00237] Analysis of both peaks for the Ba-rich sample indicates that the structural transformation of both phases, *t*-BTO and *h*-BTO, occurs simultaneously and/or facilitates each other. The observation of the phase transition in the Raman study for the sample with a Ba/Ti-ratio of 1.06 allows a deeper insight into the nature of the structure transformation. Although the phase transition region observed in the Raman spectra includes the transition temperature obtained in dielectric measurements at 350 K to 355 K, the Raman study indicates that the transformation has an extended character and covers a wider temperature range up to 420 K.

[00238] Without being bound to any particular theory, there are two reasons that might cause such a difference: the sample location, at which the Raman spectra were collected (area between top electrodes) might have bigger crystallites in addition to the smaller ones below the electrodes, which are probed in dielectric measurements or the higher losses, which are detected in this sample, could mask additional features that occur during the phase transition for the dielectric measurements. This concerted phase transition of both polymorphs may contribute to the unprecedented increase of the Curie temperature compared to the stoichiometric composition.

[00239] In summary, provided is a novel route to manipulate a ferroelectric phase transition in nanograined ferroelectric thin films. The presented approach is based on the enhanced metastable cation solubility in nanograined polycrystalline BTO thin films, which results in the formation of Schottky defects. The present disclosure comprises a number of various, independent measurements investigating the structural as well as electrical properties, which rule out other possibilities and are all consistent with the formation of Schottky defects.

[00240] The presence of Schottky defects, in particular the cation ratios, in all our films were confirmed from Rutherford backscattering spectrometry (RBS). The Ba/Ti-ratio values have been determined using RBS measurements. The details of the RBS analysis are provided elsewhere. Also, the increase of lattice parameters on Ba-rich side indicates the increased number of vacancies. The latter is consistent with a twice higher number of oxygen vacancies in the Ba-rich samples compared to the Ti-rich samples in accordance with equations (2) and (3). The absence of any additional secondary phases besides the hexagonal

polymorph, together with the lack of cation segregation at the grain boundaries and film-substrate interfaces confirm that the off-stoichiometry is accommodated within the BTO crystallites. Moreover, the independence of the ratio of hexagonal to perovskite polymorph to the Ba/Ti-ratio and the systematic change of the lattice parameter indicate that cation defects are located in the perovskite phase.

[00241] Measurements of the temperature dependence of the dielectric constant reveal that the transition temperature changes linearly from 212 K to 350 K as the Ba/Ti ratio increases from 0.8 to 1.06 for films with average grain sizes of 8-12 nm. A significant reduction in the temperature dependence of the dielectric permittivity that can be desired for some practical applications is observed and arises from a completely diffuse phase transition for all compositions. However, the degree of diffuseness slightly decreases from ~650 for a Ba/Ti-ratio of 0.8 sample to ~565 for 1.06. For two nearly stoichiometric films (Ba/Ti=1.01) with different processing sequences, a size effect manifests itself in the decrease of the Curie point from 390 K for crystallites with average size of 35 nm to 330 K for crystallites with average size of 12 nm. This allows to disentangle the contribution of the size effect to the transition temperature change from compositional effects. We propose (without being bound to any particular theory) that partial Schottky defects forming mostly divacancies (V_{Ba}-V_O, V_{Ti}-V_O) are created to accommodate the off-stoichiometry. However, the estimates show that internally imposed strain via chemical pressure should be higher than that registered by XRD. Therefore, the internal stress evolving at the grain boundaries during the crystallization process of the thin films in conjunction with a locally varying composition throughout the film are suggested to partially relax the local strain induced by Schottky defects inside the crystallites.

[00242] Temperature dependent Raman experiments confirm the transition temperature obtained from dielectric measurements. Monitoring the temperature behaviour of different modes corresponding to the hexagonal and perovskite BTO phases reveals that the presence of the hexagonal polymorph in addition to the perovskite phase influences the structural transformation on the Ba-rich side, while it is ineffective on the Ti-rich side. For the Ba-rich thin film, the Raman study indicates that although the phase transition region includes the transition temperature of 350 K determined from the dielectric measurements, structural reconstructions exhibit an extended character and occur over a wider temperature range up to 420 K.

[00243] Grain sizes

[00244] The distribution of grain sizes was obtained from the TEM images for four samples with various Ba/Ti ratios. All evaluated samples had top Pt electrodes deposited before the annealing step. FIG. 50 shows the distribution for each sample. The solid red curves are the histogram fitting by a Gaussian function. The mean values and standard deviations obtained from the fitting for each composition are as follows (in nm): 8.066 ± 0.643, 11.970 ± 0.694, 12.094 ± 0.481, and 8.697 ± 0.344 for films with Ba/Ti-ratio equals 0.8, 0.92, 1.01, and 1.06, respectively. In addition, TEM images for a stoichiometric sample (Ba/Ti=1.01) with top Pt electrodes deposited after the annealing step have been analyzed. The distribution of grain sizes for this sample is presented in FIG. 51.

[00245] A TEM cross section beneath uncovered area (between top electrodes) was also examined in a similar way. The distribution of grain sizes obtained from this area and the histogram fitting by a Gaussian function are depicted in FIG. 52. The mean value and standard deviation obtained from the fitting is 17.067 ± 0.765 nm.

[00246] It is noted that top Pt electrodes deposited before annealing cause a mechanical clamping of the film ("sandwiched" between bottom- and top-Pt) and thereby suppress the grain growth during the annealing step. The grain growth is not suppressed as the film has an "open" surface, if Pt top electrodes are deposited after annealing.

[00247] XPS data

[00248] The XPS Ti spectra for the films with Ba/Ti ratio of 0.8, 0.92, 1.01 and 1.06 and corresponding fits are presented in FIG. 53a. The two peaks at 458.21 eV and 464 eV originate from the Ti2p3/2 and Ti2p1/2 lines, respectively, and do not shift in energy as a function of composition. The Ti2p3/2 peak is fitted by one Voigt (Gaussian/Lorentzian=50/50) function at 458.19 eV (FIG. 53b), which corresponds to the valence state of Ti^{4+}. The FWHM of the Ti2p3/2 peak is 1.15 eV in all cases.

[00249] The XPS Ba spectra for the films with Ba/Ti=0.8, 0.92, 1.01 and 1.06 are displayed in FIG. 54a. The small shift of the Ba spectra is in the range of instrumental error, when we take the C1s lines as a standard for a linear calibration. The Ba3d5/2 spectrum contains two maxima. The Ba3d5/2 peak for the film with Ba/Ti=1.06 is fitted by two Voigt (Gaussian/Lorentzian=50/50) functions: at 778.84 eV and 780.24 eV, the FWHM of which are 1.3 eV and 1.63 eV, respectively (FIG. 54b). The peak at lower binding energy originates from the barium in deeper layers, and the peak at higher binding energy from the barium on

the surface that could arise due to residual unavoidable amount of $BaCO_3$ or $Ba(OH)_2$. The intensity of the line of the barium in deeper layers monotonically increases, while the intensity of the line corresponding to the barium on the surface systematically decreases with increasing Ba/Ti ratio.

[00250] Electrical data

[00251] FIG. 55 shows the electric field dependence of current density and frequency dependence of dielectric constant for all films studied. The data have been collected at room temperature. FIG. 55a demonstrates that the films with different stoichiometry with top Pt electrodes deposited before the annealing step are basically identical in their J-E response. However, the stoichiometric film (Ba/Ti=1.01) with Pt electrodes deposited after annealing experiences higher leakage current than the stoichiometric film with electrodes deposited before annealing. The error bars in FIG. 55b were evaluated using 5 independently collected data sets for each MIM-capacitor. Considering the films with Pt electrodes deposited before the annealing step, one can state that the room temperature dielectric constant strongly depends on stoichiometry, especially on the Ti-rich side. It is reduced by 50% in the Ti-rich samples compared to the stoichiometric one (Ba/Ti=1.01), but remains almost unchanged upon further increasing the Ba/Ti ratio. It should also be noted that dielectric constant is ~110 for the stoichiometric film (Ba/Ti=1.01) with top Pt electrodes deposited after the annealing procedure, and this is significantly lower than the dielectric constant ~160 for the film with Pt electrodes deposited before annealing.

[00252] The I-V response for the films with different Ba/Ti ratio was shown in (*Nanoscale*, 2018, **10**, 12515). However, in order to explicitly show that there is no correlation between conductivity and features in FIG. 42b for the film with Ba/Ti=1.06, FIG. 55a is shown to demonstrate that the films with different stoichiometry with top Pt electrodes deposited before the annealing step are basically identical in their J-E response. However, the stoichiometric film (Ba/Ti=1.01) with Pt electrodes deposited after annealing experiences higher leakage current than the stoichiometric film with electrodes deposited before annealing. To further consider the influence of the leakage current on the temperature behavior of losses, we provide the electric field dependences of current density (J-E) for the films with different Ba/Ti-ratio. The dependences depicted in FIG. 55a demonstrate that the

films with different stoichiometry are basically identical in their J-E response, so there is no correlation between the J-E behavior and features in FIG. 52b for the film with Ba/Ti=1.06.

[00253] The absolute value of the room temperature dielectric constant as a function of frequency has been presented in (Nanoscale, 2018, 10, 12515). In order to avoid the figure repetition in the present paper, we depicted this data in FIG. 55b. We also added the data collected for the film with top Pt electrodes deposited after annealing to this figure. The room temperature dielectric constant as a function of frequency for the films with Ba/Ti=0.8, 0.92, 1.01 and for the film with Ba/Ti=1.01 with top electrodes after annealing is depicted in FIG. 55b. The error bars in FIG. 55b were estimated using 5 independently collected data sets for each MIM-capacitor. Considering the films with Pt electrodes deposited before the annealing step, one can state that the room temperature dielectric constant strongly depends on stoichiometry, especially on the Ti-rich side. It is reduced by 50% in the Ti-rich samples compared to the stoichiometric one (Ba/Ti=1.01), but remains almost unchanged upon further increasing the Ba/Ti ratio. It should also be noted that dielectric constant is ~110 for the stoichiometric film (Ba/Ti=1.01) with top Pt electrodes deposited after the annealing procedure, and this is significantly lower than the dielectric constant ~160 for the film with Pt electrodes deposited before annealing.

[00254] Although Pt electrodes are described in some example embodiments, it should be understood that other electrode materials can be used, e.g., TiN, copper, graphite, titanium, brass, silver, and other conductive materials. Likewise, it should be understood that materials can be annealed before deposition of electrodes, but materials can also be annealed after deposition of electrodes.

[00255] Polarization loops

[00256] FIGs. 56 and 57 represent room temperature hysteresis loops collected for the stoichiometric (Ba/Ti=1.01) film with Pt electrodes deposited after the annealing step. The hysteresis loops were measured at different maximum electric fields and different measuring frequencies. The hysteresis loop measured at a maximum electric field of 0.65 MV/cm and a frequency of 1 kHz exhibits a maximum polarization of 7.5 $\mu C/cm^2$, while the influence of the leakage current is negligible there. This representative hysteresis loop is shown in FIG. 45.

[00257] Properties of ALD-grown nanocrystalline $BaTiO_3$- including bilayer structrues with Al_2O_3 thin films

[00258] For the deposition of the nanocrystalline $BaTiO_3$ (BTO) thin films we used a seed-layer approach with ~4-5 nm BTO seed layers annealed at 700 °C for 5 mins before depositing a thicker BTO film at 350 °C. A seed-layer approach is known to provide improved crystallinity and resulting dielectric properties for $SrTiO_3$ (STO) thin films. The precursors used for BTO and Al_2O_3 deposition were: Absolut-Ba, Ti-methoxide, Trimethyl-Al, and O_3. All annealing steps were conducted before depositing the Al_2O_3 layers. Due to the larger lattice mismatch to Pt compared to STO only a small amount of crystalline BTO forms during the ALD-process (see FIG. 59) with a weak peak at ~32° in 2θ. This is also reflected in the AFM height image (FIG. 60a) and measured properties with a field independent dielectric constant of 18 and a leakage current of 3×10^{-10} A/mm^2 at 1 MV/cm. For these films we investigated properties of MIM capacitors with the following stacking sequence: (111)-Pt bottom electrode | 32 nm BTO | 4 nm Al_2O_3 | 40 nm TiN top electrode. The TiN top electrodes were deposited using Magnetron sputtering at room temperature at a power of 450 W utilizing a standard photolithography process. The BTO on (111)-Pt substrates was annealed at 700 °C and at 750 °C for 10 mins prior to depositing 4 nm thick Al_2O_3 on top of the crystalline BTO. The crystallinity of the BTO films after the annealing step was confirmed by XRD (FIG. 59).

[00259] The Raman spectra in FIG. 60 reveal the polymorphism in all thin films. Independent of the annealing conditions, signature modes of perovskite as well as hexagonal BTO are clearly observed. These characteristics for polymorphism in these nanocrystalline BTO films are independent of the cation ratio.

[00260] The surfaces for this set of films were examined after the deposition, after annealing at 700 °C in O_2 flow, after annealing at 700 °C and at 750 °C in N_2 flow followed by ALD-growth of 4 nm Al_2O_3. The as deposited partially/slightly crystallized film reveals only small grains on the surface corroborating the XRD-data in FIG. 59, while post-deposition annealing step results in all cases in grain growth and full crystallization of BTO. The Al_2O_3 layers in FIG. 61 c) and FIG. 61 d) cannot be recognized from the AFM images as a conformal growth should preserve the topology of the BTO layer. Interestingly, the average roughness does not increase significantly and is for all films around 2 nm for an area of 5×5 μm^2. Nevertheless, an increase of the grain size with annealing temperature is clearly visible, which results in a locally increased variation in film thickness.

[00261] FIG. 62 displays high-resolution transmission electron microscopy (HR-TEM) images of two films with varying Ba/Ti-ratio after annealing at 750 °C in O_2. On the left side a Ba-rich film (Ba/Ti: 1.06) and on the right side a Ti-rich film (Ba/Ti: 0.80) exhibit very similar microstructures. In both cases, hexagonal and tetragonal BTO crystallites are randomly distributed throughout the film and the average grain sizes are 11.5 nm and 11.1 nm, respectively.

[00262] Importantly, the dielectric properties of these nanocrystalline thin films are very sensitive to the Ba/Ti-ratio. This is shown in Figs 63. a and b, where in particular for the Ti-rich side the permittivity rapidly declines and also the tunability (response to electric field) is drastically reduced.

[00263] Interestingly, the Ba/Ti-ratio also influences the ferroelectric transition temperature of these thin films as shown in FIG. 64. A significant shift in temperature of 130 K can be achieved by changing the cation composition. This new approach to tune the transition temperature is important for applications in specific temperature ranges. Another important difference to bulk $BaTiO_3$ is the relative temperature insensitivity of the dielectric constant, which is achieved by polymorphism as well as nanocrystallinity. Both features introduce additional strain at the grain boundaries of these thin films.

[00264] Based on these properties, we developed bilayers of these nanocrystalline BTO with thin amorphous Al_2O_3 layers to further reduce the leakage current and make them appealing candidates for high-*k* materials. The leakage current and dielectric parameters/characteristics were evaluated from MIM-capacitors produced as described above. In FIG. 65 the leakage current and dielectric constant (at 100 kHz) measured at room temperature for a positive bias are displayed as a function of process conditions. The different processing and annealing steps were: i) as deposited: after the ALD-growth of the film, ii) 700 °C: subsequent annealing for 10 mins under O_2 flow, iii) 700 °C+ 4 nm Al_2O_3 and iv) 750 °C+ 4 nm Al_2O_3: subsequent annealing for 10 mins under N_2 flow, followed by the growth of 4 nm Al_2O_3 at 350 °C. In all cases the top electrodes were produced as described above at the end of the MIM-capacitor processing.

[00265] It can be clearly seen from FIG. 65a that the as deposited film exhibits a very low current density in agreement with the mostly amorphous state of the BTO layer as determined by XRD. Comparing the films annealed at 700 °C with and without Al_2O_3 layer, we can see that a 4 nm thick layer of amorphous Al_2O_3 reduces the current density by one

order of magnitude. Annealing at 750 °C increases the leakage current again by one order of magnitude, which can be attributed to the larger grains observed by AFM (see Figs. 61c and d) resulting in less conformal coverage by Al_2O_3 and in locally increased electric fields due to variations in the film thickness.

[00266] The dielectric constant as a function of positive electric field for the same MIM-capacitors is shown in FIG. 65b. We calculated the overall dielectric constant of the BTO-Al_2O_3 stacks of 36 nm thickness using the standard model for two parallel-plate capacitors in series. The as deposited MIM-structure has a very low field independent dielectric constant of 18 as expected for an amorphous film. After annealing, the dielectric constant for all MIM-devices shows a similar field-dependence with the film annealed at 700 °C exhibiting a value of 103 at E=0 and the film annealed at 750 °C exhibiting a value of 130 at E=0, respectively. Both MIM-capacitor stacks exceed the benchmark value of 100, which is mandatory for further downscaling of electronic devices.

[00267] FIG. 10 shows a comparison of the dielectric constant at 0 MV/cm and leakage current at 1 MV/cm (or highest electric field measured if below 1 MV/cm) for BTO-Al_2O_3 dielectric stacks to various other high-*k* thin films and thin film stacks. The ideal material should be located in the top left corner.

[00268] Comparing these results to a variety of other high-*k* materials reveals the outstanding performance based on the combination of leakage current and dielectric constant for the BTO-Al_2O_3 thin film stacks (see FIG. 10). For high-*k* materials it is most desirable to simultaneously exhibit high dielectric constants and low leakage currents, which corresponds to the top left corner in FIG. 65. In this respect the BTO-Al_2O_3 thin-film stacks are well separated from competitor materials. In particular, the comparison to STO-Al_2O_3 stacks with STO thickness of 50 nm and Al_2O_3 of up to 4 nm demonstrates the superior performance exhibited by the BTO-Al_2O_3 thin-film stacks. The large potential for up-scaling this process as well as integration into existing semiconductor industry platforms deems this approach highly appealing for industrial applications.

[00269] Embodiments

[00270] The following embodiments are illustrative only and do not serve to limit the scope of the present disclosure or the appended claims.

[00271] Embodiment 1. A capacitive component, comprising: a plurality of films, the plurality of films comprising: a first grained film component, the first grained film

component comprising at least one of $SrTiO_3$, $BaTiO_3$, and (Ba, Sr)TiO_3, and the first grained film component optionally being characterized as being at least partially polymorphic crystalline in nature; a second film component contacting the first grained film component, the second film component optionally comprising Al_2O_3, and the first grained film component optionally defining an average grain size of less than about 10 micrometers, optionally less than about 9 micrometers, optionally less than about 8 micrometers, optionally less than about 7 micrometers. optionally less than about 6 micrometers, optionally less than about 5 micrometers, optionally less than about 4 micrometers, optionally less than about 3 micrometers, optionally less than about 2 micrometers, or optionally less than about 1 micrometer.

[00272] The first grained film component can comprise one of $SrTiO_3$, $BaTiO_3$, and (Ba, Sr)TiO_3. $BaTiO_3$ is considered particularly suitable. The first grained film component can be partially crystallized or even completely crystallized.

[00273] Embodiment 2. The capacitive component of Embodiment 1, wherein the first grained film component defines a grain size in the range of from about 0.01 to about 9 micrometers. The grain size can be from about 0.6 to about 7 micrometers, from about 0.8 to about 6 nm, from about 1 to about 4 micrometers, or even from about 1.3 to about 3.5 micrometers. The grain size can also be on the order of nanometers, tens of nanometers, or even hundreds of nanometers.

[00274] Embodiment 3. The capacitive component of any one of Embodiments 1-2, wherein the first grained film component defines a thickness in the range of from about 1 nm to about 50 nm. Thicknesses of about 1 to about 50 nm, or from about 3 to about 43 nm, or from about 5 to about 38 nm, or from about 8 to about 33 nm, or even from about 10 to about 27 nm are all considered suitable.

[00275] Embodiment 4. The capacitive component of any one of Embodiments 1-3, wherein the second film component defines a thickness in the range of from about 1 nm to about 50 nm. Thicknesses of about 1 to about 50 nm, or from about 3 to about 43 nm, or from about 5 to about 38 nm, or from about 8 to about 33 nm, or even from about 10 to about 27 nm are all considered suitable.

[00276] The total thickness of the first grained film component and the second film component can be, e.g., from about 5 to about 100 nm, from about 10 to about 90 nm, from about 15 to about 80 nm, from about 20 to about 75 nm, from about 25 to about 70 nm, from

about 30 to about 65 nm, or even from about 35 to about 55 nm. The total thickness of the capacitive component can be less than about 75 nm, or less than about 70 nm, or less than about 65 nm, or less than about 60 nm, or less than about 55 nm, or even less than about 50 nm or less than about 45 nm.

[00277] Embodiment 5. The capacitive component of any one of Embodiments 1-4, wherein the first grained film component defines a thickness, the second film component defines a thickness, and wherein the ratio of the thickness of the first grained film component to the thickness of the second film component is from about 50:1 to about 1:5.

[00278] Embodiment 6. The capacitive component of any one of Embodiments 1-5, wherein the plurality of films is characterized as having a dielectric constant, at 0 V, of greater than about 40. The dielectric constant can be, e.g., from about 40 to about 140, from about 45 to about 140, from about 50 to about 135, from about 55 to about 130, from about 50 to about 125, from about 55 to about 120, from about 60 to about 115, from about 65 to about 110, from about 70 to about 105, or even from about 80 to about 100. Dielectric constants between 50 and about 100, or between 50 and about 95, or between 50 and about 90, or between 50 and about 85, or between 50 and about 80, or between 50 and about 75, or between 50 and about 70, or between 50 and about 65, or between 50 and about 55 are all considered suitable.

[00279] Embodiment 7. The capacitive component of any one of Embodiments 1-6, wherein the plurality of films is characterized as having a dielectric constant, at 0 V, of from about 40 to about 100 or even to about 120.

[00280] Embodiment 8. The capacitive component of any one of Embodiments 1-7, wherein the plurality of films is characterized as having a leakage current, measured at 1 MV/cm and at 125 deg C., in the range of from about 1×10^{-7} A/mm^2 to about 1×10^{-8} A/mm^2.

[00281] Embodiment 9. The capacitive component of any one of Embodiments 1-8, wherein the plurality of films comprises a third film component. As one example, a component can include films layered as, e.g., Al_2O_3-$BaTiO_3$-Al_2O_3.

[00282] Embodiment 10. The capacitive component of Embodiment 9, wherein the third film component comprises Al_2O_3.

[00283] Embodiment 11. The capacitive component of any one of Embodiments 9-10, wherein the third film component defines a thickness in the range of from about 1 nm to

about 20 nm. The third film component can contact the first film component on a side other than a side where the first film component contacts the second film component.

[00284] Embodiment 12. The capacitive component of any one of Embodiments 1-11, wherein the plurality of films is disposed between a first electrode and a second electrode. One or both of the first electrode and the second electrode can comprise, for example, Ag, Cu, Au, Al, Be, Ca, Mg, Rh, Na, Ir, Cu, Zn, Pb, Ni, brass, bronze, TiN, a conductive polymer (e.g., polyfluorines, polyphenylenes, polypyrenes, polyazulenes, polynaphthalenes, polyacetylenes, poly(p-phenylene vinylene), polypyrroles, polycarbazoles, polyindoles, polyazepines, polyanilenes, polythiopenes, poly(3,4-ethylenedioxythiophene), poly(p-phenylene sulfide), carbonaceous materials (e.g., graphite, graphene, carbon nanotubes), aluminum, LiF, Pd, brass, Pt, carbon steel, and the like.

[00285] As described elsewhere herein, a plurality of films can comprise three dielectric films stacked together, e.g., Al_2O_3 – $BaTiO_3$ – Al_2O_3.

[00286] Embodiment 13. The capacitive component of any one of Embodiments 1-12, wherein the first grained film component comprises $BiTiO_3$, and wherein the molar ratio of Ba to Ti is from about 0.80 to about 1.06.

[00287] Embodiment 14. A capacitive component, comprising: a plurality of films, the plurality of films optionally being disposed between a first electrode and a second electrode, and the plurality of films comprising: a first grained film component, the first grained film component being characterized as being at least partially crystalline polymorphic; a second film component contacting the first grained film component, the second film component optionally comprising Al_2O_3, and the plurality of films optionally having a dielectric constant, at 0 V, of from about 40 to about 140 and optionally a leakage current, measured at 1 MV/cm and 125 deg. C., of from about 10^{-7} A/mm^2 to about 10^{-8} A/mm^2.

[00288] The dielectric constant can be, e.g., from about 40 to about 140, from about 42 to about 135, from about 45 to about 120, from about 50 to about 110, from about 55 to about 105, from about 60 to about 100, from about 65 to about 95, from about 70 to about 90, or from about 75 to about 85.

[00289] As one example, a component can comprise (i) a first electrode that comprises one or more of Pt and TiN, (ii) a first grained film component that contacts the first electrode and that comprises at least one of $SrTiO_3$, $BaTiO_3$, and (Ba, Sr)TiO_3, a second film

component that contacts the first grained film component and that comprises Al_2O_3 (e.g., in at least partially amorphous form), and a second electrode that contacts the second film component and that comprises one or more of Pt and TiN.

[00290] Embodiment 15. The capacitive component of Embodiment 14, wherein the first grained film component defines a thickness, the second film component defines a thickness, and wherein the ratio of the thickness of the first grained film component to the thickness of the second film component is from about 50:1 to about 1:5. The total (combined) thickness of the first grained film component and the second film component can be, e.g., from 10 to 50 nm, from 15 to 45 nm, from 20 to 40 nm, from 25 to 35, nm, or even about 30 nm.

[00291] Embodiment 16. The capacitive component of any one of Embodiments 14-15, wherein the first grained film component defines a grain size of less than about 10 micrometers, optionally less than about 9 micrometers, optionally less than about 8 micrometers, optionally less than about 7 micrometers. optionally less than about 6 micrometers, optionally less than about 5 micrometers, optionally less than about 4 micrometers, optionally less than about 3 micrometers, optionally less than about 2 micrometers, or optionally less than about 1 micrometer. Grain sizes can also be in the range of from about 10 to about 1000 nm, or from about 15 to about 800 nm, or from about 20 to about 700 nm, or from about 50 to about 500 nm, or even from about 75 to about 250 nm. Thus, grains can be in the sub-micrometer size.

[00292] Embodiment 17. An article, the article comprising a capacitive component according to any one of Embodiments 1-16.

[00293] Embodiment 18. A method, comprising discharging electrical energy from a capacitive component according to any one of Embodiments 1-16.

[00294] Embodiment 19. A method, comprising storing electrical energy in a capacitive component according to any one of Embodiments 1-16.

[00295] Embodiment 20. A method, comprising energizing an electrical load with energy discharged from a capacitive component according to any one of Embodiments 1-16. Example electrical loads include, e.g., mobile devices, memory devices, medical instruments, automotive components, aerospace components, and the like. Essentially any electrical load can be energized by energy discharged from a capacitive component according to the present disclosure.

[00296] Embodiment 21. A component, the component being made according to any methods described herein.

[00297] Embodiment 22. The component of Embodiment 21, wherein the component is a component according to any one of Embodiments 1-16.

[00298] Embodiment 23. A nano-grained film, comprising: a BaTiO3 film component comprising a Ba/Ti ratio of between about 0.8 and 1.06, a transition temperature of the nano-grained film being dependent on the Ba/Ti ratio, and the nano-grained film exhibiting a diffused phase transition, optionally whereby a temperature density of a dielectric constant of the nano-grained film is minimized.

[00299] A film according to the present disclosure can have a thickness of from about 1 to about 100 nm, or from about 2 to about 50 nm, or even from about 3 to about 25 nm.

[00300] Embodiment 24. The nano-grained film of claim 23, wherein the transition temperature is the Curie temperature of the nano-grained film.

[00301] Embodiment 25. The nano-grained film of claim 23, wherein the nano-grained film comprises a hexagonal phase associated with at least a Ba-rich portion of the nano-grained film.

[00302] Embodiment 26. The nano-grained film of any one of claims 23-25, comprising a perovskite phase.

[00303] Embodiment 27. The nano-grained film of any one of claims 23-26, wherein the nano-grained film exhibits a dielectric constant of from about 84 on cooling to about 163 on cooling. Dielectric constant value of from about 85 to about 162, or from about 90 to about 155, or from about 95 to about 145, or from about 100 to about 135, or even from about 110 to about 120 are all suitable. Such values can depend on the stoichiometry of the Ba/Ti present in the film.

[00304] Embodiment 28. The nano-grained film of any one of claims 23-27, wherein the nano-grained film defines a thickness of from about 10 to about 100 nm.

[00305] Embodiment 29. The nano-grained film of claim 28, wherein the nano-grained film defines a thickness of from about 25 to about 75 nm,

[00306] Embodiment 30. The nano-grained film of claim 28, wherein the nano-grained film defines an average grain size of from about 5 to about 15 nm.

[00307] Embodiment 31. The nano-grained film of claim 30, wherein the nano-grained film defines an average grain size of from about 8 to about 12 nm.

[00308] Embodiment 32. The nano-grained film of any one of claims 23-31, wherein the Ba/Ti ratio is less than 1.00.

[00309] Embodiment 33. The nano-grained film of any one of claims 23-32, wherein the Ba/Ti ratio is greater than 1.00.

[00310] Embodiment 34. A nano-grained film configured to exhibit a diffused phase transition, whereby a temperature density of a dielectric constant of the nano-grained film is minimized, wherein a transition temperature and the temperature density of the dielectric constant of the nano-grained film is tuned based at least on stoichiometry of one or more materials forming the nano-grained film.

[00311] Embodiment 35. A method, comprising forming a nano-grained film according to any one of claims 22-34.

[00312] Embodiment 36. A device, comprising: one or more electrodes in electronic communication with a nano-grained film according to any one of claims 22-34.

[00313] Embodiment 37. The device of claim 36, wherein the device is characterized as a memory device, a power transfer device, a microwave device, or a surface acoustic wave resonator.

[00314] Embodiment 38. A method, comprising operating a device according to any one of claims 36-37.

[00315] Embodiment 39. The method of claim 38, further comprising operating the device such that the nano-grained film attains its Curie temperature.

[00316] Embodiment 40. The device of any one of claims 36-37, wherein an electrode comprises Pt.

[00317] Embodiment 41. The device of any one of claim 36-37, wherein an electrode comprises TiN.

[00318] Embodiment 42. A method, comprising: tuning a Curie transition temperature of a nano-grained film that comprises a $BaTiO_3$ film component comprising a Ba/Ti ratio of between about 0.8 and 1.06, a transition temperature of the nano-grained film being dependent on the Ba/Ti ratio, and the nano-grained film exhibiting a diffused phase transition, optionally whereby a temperature density of a dielectric constant of the nano-grained film is minimized, the tuning comprising modulating the Ba/Ti ratio.

[00319] References

[00320] H. Hu, C. Zhu, Y. F. Lu, M. F. Li, A High Performance MIM Capacitor Using HfO_2 Dielectrics. IEEE Electron Device Letters 23 (9), 514-516 (2002).

[00321] F. El Kamel, P. Gonon, C. Vallée, and C. Jorel. Electrode effects on the conduction mechanisms in HfO_2-based metal-insulator-metal capacitors. J. Appl. Phys. 106, 064508 (2009).

[00322] P. C. Joshi and M. W. Cole. Influence of post deposition annealing on the enhanced structural and electrical properties of amorphous and crystalline Ta_2O_5 thin films for dynamic random access memory applications. Journal of Applied Physics 86, 871 (1999).

[00323] S.K. Kim, K.M. Kim, D.S. Jeong, W. Jeon, K.J. Yoon, C.S. Hwang, Titanium dioxide thin films for next-generation memory devices, J. Mater. Res. 28 (2013) 313–325.

[00324] S.-Y. Lee, H. Kim, C. McIntyre, K. C. Saraswat, J.-S. Byun. Atomic layer deposition of ZrO_2 on W for metal–insulator–metal capacitor application. Appl. Phys. Lett. 82(17), 2874-2876 (2003).

[00325] B.-E. Park, I.-K. Oh, C. Mahata, C.W. Lee, D. Thompson, H.-B.-Ram Lee, W. J. Maeng, H. Kim. Atomic layer deposition of Y-stabilized ZrO_2 for advanced DRAM capacitors Journal of Alloys and Compounds 722 (2017) 307-312.

[00326] G. Łupina,a G. Kozłowski, J. Dąbrowski, Ch. Wenger, P. Dudek, P. Zaumseil, G. Lippert, Ch. Walczyk, and H.-J. Müssig. Thin $BaHfO_3$ high-*k* dielectric layers on TiN for memory capacitor applications. Appl. Phys. Lett. 92, 062906 (2008).

[00327] G. Łupina, J. Dąbrowski, P. Dudek, G. Kozłowski, P. Zaumseil, G. Lippert, O. Fursenko, J. Bauer, C. Baristiran, I. Costina, H.-J. Müssig, L. Oberbeck, and U. Schröder. Dielectric constant and leakage of $BaZrO_3$ films. Appl. Phys. Lett. **94**, 152903 (2009).

[00328] M. A. Pawlak, B. Kaczer, M.-S. Kim, M. Popovici, K. Tomida, J. Swerts, K. Opsomer, W. Polspoel, P. Favia, C. Vrancken, C. Demeurisse, W.-C. Wang, V. V. Afanas'ev, W. Vandervorst, H. Bender, I. Debusschere, L. Altimime, and J. A. Kittl. Impact of crystallization behavior of $Sr_xTi_yO_z$ films on electrical properties of metal-insulator-metal capacitors with TiN electrodes. Appl. Phys. Lett. 97, 162906 (2010).

[00329] N. Menou, M. Popovici, S. Clima, K. Opsomer, W. Polspoel, B. Kaczer, G. Rampelberg, K. Tomida, M. A. Pawlak, C. Detavernier, D. Pierreux, J. Swerts, J. W. Maes, D. Manger, M. Badylevich, V. Afanasiev, T. Conard, P. Favia, H. Bender, B. Brijs, W.

Vandervorst, S. Van Elshocht, G. Pourtois, D. J. Wouters, S. Biesemans, and J. A. Kittl. Composition influence on the physical and electrical properties of $Sr_xTi_{1-x}O_y$-based metal-insulator-metal capacitors prepared by atomic layer deposition using TiN bottom electrodes. J. Appl. Phys. 106, 094101 (2009).

[00330] V. Longo, F. Roozeboom, W.M.M. Kessels and M.A. Verheijen. ALD of $SrTiO_3$ and Pt for Pt/$SrTiO_3$/Pt MIM structures: Growth and Crystallization study. ECS Transactions, 58 (10) 153162 (2013).

[00331] M. Vehkama¨ki, T. Hatanpa¨a¨, T. Ha¨nninen, M. Ritala and M. Leskela¨, Growth of $SrTiO_3$ and $BaTiO_3$ Thin Films by Atomic Layer Deposition. Electrochem. Solid-State Lett. 2, 504-506 (1999).

[00332] M. Vehkama¨ki, T. Hatanpa¨a¨, M. Ritala, M. Leskela¨, S. Va¨yrynen and E. Rauhala, Atomic Layer Deposition of $BaTiO_3$ Thin Films—Effect of Barium Hydroxide Formation. Chem. Vap. Deposition 13, 239-246 (2007).

[00333] M. W. Cole, E. Ngo, C. Hubbard, S. G. Hirsch, M. Ivill, W. L. Sarney, J. Zhang, and S. P. Alpay. Enhanced dielectric properties from barium strontium titanate films with strontium titanate buffer layers. J. Appl. Phys. 114, 164107 (2013).

[00334] K. P. Jayadevan, C. Y. Liu, and T. Y. Tseng. Dielectric characteristics of nanocrystalline Ag–$Ba_{0.5}Sr_{0.5}TiO_3$ composite thin films. Appl. Phys. Lett. 85, 1211 (2004).

[00335] L. Z. Cao, B. L. Cheng, S. Y. Wang, Y. L. Zhou, K. J. Jin, H. B. Lu, Z. H. Chen, and G. Z. Yang. Dielectric properties of Si–$Ba_{0.5}Sr_{0.5}TiO_3$ composite thin films elaborated by pulsed laser deposition. J. Appl. Phys. 98, 034106 (2005).

[00336] RF and Analog/Mixed-Signal Technologies for Wireless Communications, International Roadmap for Semiconductors (Semiconductor Industry Association, 2009 and 2011 updates).

[00337] Handbook of Electronic and Photonic Materials, edited by S. Kasap and P. Capper. Springer International Publishing AG, 2017.

[00338] K. Kukli, J, Ihanus, M. Ritala, and M. Leskela. Tailoring the dielectric properties of HfO_2– Ta_2O_5 nanolaminates. Appl. Phys. Lett. 68 (26), 3737-3739 (1996).

[00339] S. H. Lin, K. C. Chiang, Albert Chin, and F. S. Yeh. High-Density and Low-LeakageCurrent MIM Capacitor Using Stacked TiO_2/ZrO_2 Insulators. IEEE ELECTRON DEVICE LETTERS 30(7), 715-717 (2009).

[00340] S.-J. Ding, C. Zhu, M.-F., D. W. Zhang. Atomic-layer-deposited Al_2O_3–HfO_2–Al_2O_3 dielectrics for metal-insulator-metal capacitor applications. Appl. Phys. Lett. 87, 053501 (2005).

[00341] J.-H. Ahn, J.-Y. Kim, S.-J. Jeong, S.-H. Kwon. Effect of Al_2O_3 insertion on the electrical properties of $SrTiO_3$ thin films: A comparison between Al_2O_3-doped $SrTiO_3$ and $SrTiO_3/Al_2O_3/SrTiO_3$ sandwich structure. Materials Research Bulletin 64 (2015) 1–5.

[00342] M. Lukosius, C. Wenger, T. Blomberg, G. Ruhl. Properties of stacked $SrTiO_3/Al_2O_3$ metal– insulator–metal capacitors. J. Vac. Sci. Technol. B 31(1), 01A102-1 - 01A102-6 (2013).

[00343] S. Li, A. Wachau, R. Schafranek, A. Klein, Yu. Zheng, and R. Jakoby. Energy level alignment and electrical properties of $(Ba,Sr)TiO_3$-Al_2O_3 interfaces for tunable capacitors. J. Appl. Phys. 108, 014113 (2010).

[00344] M. Pešic′, S. Knebel, K. Cho, C. Jung, J. Chang, H. Lim, N. Kolomiiets, V. V. Afanas'ev, T. Mikolajick, U. Schroeder. Conduction barrier offset engineering for DRAM capacitor scaling. Solid-State Electronics 115, 133–139 (2016).

[00345] Takashi Onaya, Toshihide Nabatame, Tomomi Sawada, Kazunori Kurishima, Naomi Sawamoto, Akihiko Ohi, Toyohiro Chikyow, Atsushi Ogura. Improved leakage current properties of $ZrO_2/(Ta/Nb)O_x$-Al_2O_3/ZrO_2 nanolaminate insulating stacks for dynamic random access memory capacitors. Thin Solid Films 655 48–53 (2018).

[00346] Richard W. Johnson, Adam Hultqvist, and Stacey F. Bent A brief review of atomic layer deposition: from fundamentals to applications. Materials Today 17(5), 236- 246 (2014).

[00347] J. H. Shim, H. J. Choi, Y. Kim, J. Torgersen, J. An, M. H. Lee and F. B. Prinz. Process– property relationship in high-*k* ALD $SrTiO_3$ and $BaTiO_3$: a review. *J. Mater. Chem. C,* 2017, 5, 8000.

[00348] H. H. Sønsteby, H. Fjellvåg and O. Nilsen, Functional Perovskites by Atomic Layer Deposition – An Overview, Adv. Mater. Interfaces, 2017, 4, 1600903.

[00349] M. Falmbigl, I. A. Karateev, I. S. Golovina, A. V. Plokhikh, T. C. Parker, A. L. Vasiliev and J. E. Spanier. Evidence of extended cation solubility in atomic layer deposited nanocrystalline $BaTiO_3$ thin films and its strong impact on the electrical properties. Nanoscale, 2018, 10, 12515.

[00350] S. Rentrop, B. Abendroth, J. Walter, J. Rensberg, W. Münchgesang, R. Strohmeyer, H. Stöcker, C. Ronning, S. Gemming, D.C. Meyer. Stoichiometry variation for the atomic layer deposition of $Sr_xTi_yO_z$ from $Sr(iPr3Cp)_2$, $Ti[N(CH3)_2]_4$ and H_2O. Thin Solid Films 577 (2015) 134–142.

[00351] S. W. Lee, J. H. Han, S. Han, W. Lee, J. H. Jang, M. Seo, S. K. Kim, C. Dussarrat, J. Gatineau, Yo-Sep Min, and C. S. Hwang. Atomic Layer Deposition of $SrTiO_3$ Thin Films with Highly Enhanced Growth Rate for Ultrahigh Density Capacitors. Chem. Mater. 2011, 23, 2227– 2236.

[00352] S. Rentrop, T. Moebus, B. Abendroth, R. Strohmeyer, A. Schmid, T.Weling, J. Hanzig, F. Hanzig, H. Stöcker, D.C. Meyer. Atomic layer deposition of strontium titanate films from $Sr(iPr3Cp)_2$, $Ti[N(CH3)_2]_4$ and H_2O. Thin Solid Films 550 (2014) 53–58.

[00353] W. Lee, S. Yoo, W. Jeon, Y. W. Yoo, C. H. An, M. J. Chung, H. J. Kim, S. W. Lee, C. S. Hwang. Reducing the nano-scale defect formation of atomic-layer-deposited $SrTiO_3$ films by adjusting the cooling rate of the crystallization annealing of the seed layer. Thin Solid Films 589 (2015) 723–729.

[00354] An, J.; Usui, T.; Logar, M.; Park, J.; Thian, D.; Kim, S.; Kim, K.; Prinz, F. B. Plasma Processing for Crystallization and Densification of ALD $BaTiO_3$ Thin Films. ACS Appl. Mater. Interfaces 2014, 6, 10656−10660.

[00355] Acharya, S.; Torgersen, J.; Kim, Y.; Park, J.; Schindler, P.; Dadlani, A. L.; Winterkorn, M.; Xu, S.; Walch, S. P.; Usui, T.; et al. Self-Limiting Atomic Layer Deposition of Barium Oxide and Barium Titanate Thin Films Using a Novel Pyrrole Based Precursor. J. Mater. Chem. C 2016, 4 (10), 1945−1952.

[00356] Schindler, P.; Kim, Y.; Thian, D.; An, J.; Prinz, F. B. Plasma-Enhanced Atomic Layer Deposition of $BaTiO_3$. Scr. Mater. 2016, 111, 106−109.

[00357] M. Falmbigl, I. S. Golovina, A. V. Plokhikh, D. Imbrenda, A. Podpirka, C. J. Hawley, G. Xiao, A. Gutierrez-Perez, I. A. Karateev, A. L. Vasiliev, T. C. Parker, and J. E. Spanier. $BaTiO_3$ Thin Films from Atomic Layer Deposition: A Superlattice Approach. J. Phys. Chem. C 2017, 121, 16911−16920.

[00358] M. Tyunina; M. Plekh; J. Levoska; M. VEHKAMÄKI; M. HATANPÄÄ; M. Ritala; M. LESKELÄ. Dielectric Properties of Atomic Layer Deposited Thin-Film Barium Strontium Titanate. Integrated Ferroelectrics 102: 29–36, 2008.

[00359] I. S. Golovina, M. Falmbigl, A. V. Plokhikh, T. C. Parker, C. Johnson and Jonathan E. Spanier. Effect of annealing conditions on the electrical properties of ALD-grown polycrystalline $BiFeO_3$ films. *J. Mater. Chem. C,* 2018, 6, 5462.

[00360] K. Lee, W. Jang, H. Kim, H. Lim, B. Kim, H. Seo, H. Jeon. Leakage current suppression in spatially controlled Si-doped ZrO_2 for capacitors using atomic layer deposition. *Thin Solid Films 657 (2018) 1–7.*

[00361] I. S. Golovina, M. Falmbigl, C. J. Hawley, A. J. Ruffino, A. V. Plokhikh, I. A. Karateev, T. C. Parker, A. Gutierrez-Perez, A. L. Vasiliev and J. E. Spanier. Controlling the phase transition in nanocrystalline ferroelectric thin films via cation ratio. Nanoscale, 2018, 10, 21798.

[00362] O. S. Kwon, S. W. Lee, J. H. Han and C. S. Hwang, Atomic Layer Deposition and Electrical Properties of $SrTiO_3$ Thin Films Grown Using $Sr(C_{11}H_{19}O_2)_2$, $Ti(Oi\text{-}C_3H_7)_4$, and H_2O. *J. Electrochem. Soc.*, 2007, 154, G127.

[00363] S. W. Lee, O. S. Kwon, J. H. Han and C. S. Hwang. Enhanced electrical properties of $SrTiO_3$ thin films grown by atomic layer deposition at high temperature for dynamic random access memory applications. *Appl. Phys. Lett.*, 2008, 92, 222903.

[00364] C. Baristiran Kaynak, M. Lukosius, B. Tillack, Ch. Wenger, T. Blomberg, G. Ruhl. Single $SrTiO_3$ and $Al_2O_3/SrTiO_3/Al_2O_3$ based MIM capacitors: Impact of the bottom electrode material. *Microelectron. Eng.* 88, 1521–1524 (2011).

[00365] M. Kurasawa and P. C. Mclntyre, Surface passivation and electronic structure characterization of $PbTiO_3$ thin films and $Pt/PbTiO_3$ interfaces. *J. Appl. Phys.* **2005**, *97*, 104110.

[00366] Schafranek, R.; Payan, S.; Maglione, M.; Klein, A. Barrier Height at $(Ba,Sr)TiO_3$/Pt Interfaces Studied by Photoemission. *Phys. Rev. B* **2008**, *77* (19), 195310.

[00367] Hillmann, S.; Rachut, K.; Bayer, T. J. M.; Li, S.; Klein, A. Application of Atomic Layer Deposited Al_2O_3 as Charge Injection Layer for High-Permittivity Dielectrics. *Semicond. Sci. Technol.* **2015**, *30* (2), 024012.

[00368] Robertson, J. Band Offsets, Schottky Barrier Heights, and Their Effects on Electronic Devices. *J. Vac. Sci. Technol. A Vacuum, Surfaces, Film.* **2013**, *31* (5), 050821.

[00369] Wang, S. Y.; Li, M.; Liu, W. F.; Gao, J. Resistive Switching Behavior of $BaTiO_3/La_{0.8}Ca_{0.2}MnO_3$ heterostructures. *Phys. Lett. Sect. A Gen. At. Solid State Phys.* **2015**, *379* (18–19), 1288–1292.

[00370] Huang, M. L.; Chang, Y. C.; Chang, C. H.; Lin, T. D.; Kwo, J.; Wu, T. B.; Hong, M. Energy-Band Parameters of Atomic-Layer-Deposition Al_2O_3/InGaAs Heterostructure. *Appl. Phys. Lett.* **2006**, *89* (1), 2006–2008.

[00371] Lee, S. W., Han, J. H., Kwon, O. S. and Hwang, C. S. Influences of a Crystalline Seed Layer during Atomic Layer Deposition of $SrTiO_3$ Thin Films Using Ti(O-iPr)$_2$(thd)$_2$, Sr(thd)$_2$, and H_2O. *J. Electrochem. Soc.* **155,** G253 (2008).

[00372] Kadoshima, M., Hiratani, M., Shimamoto, Y., Torii, K. and Miki, H. Rutile-type TiO_2 thin film for high- k gate insulator. **424,** 224–228 (2003).

[00373] Yan, L. *et al.* High quality, high-*k* gate dielectric: amorphous $LaAlO_3$ thin films grown on Si(100) without Si interfacial layer. *Appl. Phys. A* **77,** 721–724 (2003).

[00374] Kittl, J. A. *et al.* High-*k* dielectrics for future generation memory devices (Invited Paper). *Microelectron. Eng.* **86,** 1789–1795 (2009).

[00375] García, H. *et al.* Influence of precursor chemistry and growth temperature on the electrical properties of $SrTiO_3$-based metal-insulator-metal capacitors grown by atomic layer deposition. *J.* Vac. Sci. Technol. B Microelectron. Nanom. Struct. **29,** 01AC04 (2011).

[00376] Kishiro, K., Inoue, N., Chen, S.-C. and Yoshimaru, M. Structure and Electrical Properties of Thin Ta_2O_5 Deposited on Metal Electrodes. *Jpn. J. Appl. Phys.* **37,** 1336–139 (1998). [56] Zhang, H., Solanki, R., Roberds, B., Bai, G. and Banerjee, I. High permittivity thin film nanolaminates. *J. Appl. Phys.* **87,** 1921–1924 (2000).

[00377] Jeong, C.-W., Lee, J.-S. and Joo, S.-K. Plasma-assisted atomic layer growth of high-quality aluminum oxide thin films. *Jpn. J. Appl. Phys.* **40,** 285 (2001).

[00378] Lukosius, M. *et al.* Electrical and Morphological Properties of ALD and AVD Grown Perovskite-Type Dielectrics and Their Stacks for Metal-Insulator-Metal Applications. *ECS J.* Solid State Sci. Technol. **1,** N1–N5 (2012).

What is Claimed:

1. A capacitive component, comprising:
a plurality of films, the plurality of films comprising:
a first grained film component,
the first grained film component comprising at least one of $SrTiO_3$, $BaTiO_3$, and $(Ba, Sr)TiO_3$, and
the first grained film component optionally being characterized as being at least partially polymorphic crystalline in nature;
a second film component contacting the first grained film component,
the second film component optionally comprising Al_2O_3, and
the first grained film component optionally defining an average grain size of less than about 10 micrometers.

2. The capacitive component of claim 1, wherein the first grained film component defines a grain size in the range of from about 0.01 to about 9 micrometers.

3. The capacitive component of any one of claims 1-2, wherein the first grained film component defines a thickness in the range of from about 1 to about 50 nm.

4. The capacitive component of any one of claims 1-2, wherein the second film component defines a thickness in the range of from about 1 to about 50 nm.

5. The capacitive component of any one of claims 1-2, wherein the first grained film component defines a thickness, the second film component defines a thickness, and wherein the ratio of the thickness of the first grained film component to the thickness of the second film component is from about 50:1 to about 1:5.

6. The capacitive component of any one of claims 1-2, wherein the plurality of films is characterized as having a dielectric constant, at 0 V, of greater than about 40.

7. The capacitive component of any one of claims 1-2, wherein the plurality of films is characterized as having a dielectric constant, at 0 V, of from about 40 to about 120.

8. The capacitive component of any one of claims 1-2, wherein the plurality of films is characterized as having a leakage current, measured at 1 MV/cm and at 125 deg C., in the range of from about 1 x 10^{-7} A/mm^2 to about 1 x 10^{-8} A/mm^2.

9. The capacitive component of any one of claims 1-2, wherein the plurality of films comprises a third film component.

10. The capacitive component of claim 9, wherein the third film component comprises Al_2O_3.

11. The capacitive component of claim 9, wherein the third film component defines a thickness in the range of from about 1 to about 20 nm.

12. The capacitive component of any one of claims 1-2, wherein the plurality of films is disposed between a first electrode and a second electrode.

13. The capacitive component of any one of claims 1-2, wherein the first grained film component comprises $BiTiO_3$, and wherein the molar ratio of Ba to Ti is from about 0.80 to about 1.06.

14. A capacitive component, comprising:
a plurality of films, the plurality of films optionally being disposed between a first electrode and a second electrode, and the plurality of films comprising:
a first grained film component,
the first grained film component being characterized as being at least partially crystalline polymorphic;
a second film component contacting the first grained film component,
the second film component optionally comprising Al_2O_3, and

the plurality of films being characterized as optionally having a dielectric constant, at 0 V, of from about 40 to about 140 and optionally having a leakage current, measured at 1 MV/cm and 125 deg. C., of from about 10^{-7} A/mm^2 to about 10^{-8} A/mm^2.

15. The capacitive component of claim 14, wherein the first grained film component defines a thickness, the second film component defines a thickness, and wherein the ratio of the thickness of the first grained film component to the thickness of the second film component is from about 50:1 to about 1:5.

16. The capacitive component of any one of claims 14-15, wherein the first grained film component defines a grain size of less than about 10 micrometers.

17. An article, the article comprising a capacitive component according to any one of claims 1-2 or 14.

18. A method, comprising discharging electrical energy from a capacitive component according to any one of claims 1-2 or 14.

19. A method, comprising storing electrical energy in a capacitive component according to any one of claims 1-2 or 14.

20. A method, comprising energizing an electrical load with energy discharged from a capacitive component according to any one of claims 1-2 or 14.

21. A component, the component being made according to any methods described herein.

22. The component of claim 21, wherein the component is a component according to any one of claims 1-2 or 14.

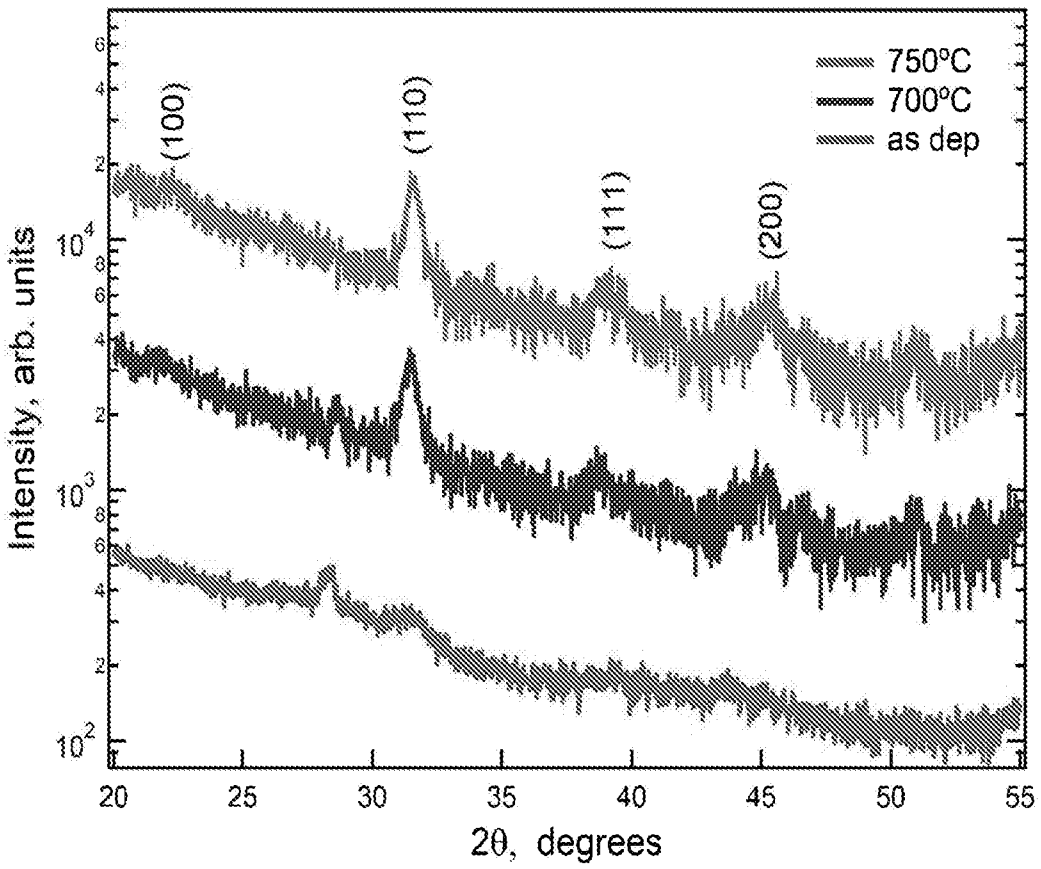
750°C
700°C
as dep
(100)
(110)
(111)
(200)
Intensity, arb. units
2θ, degrees

FIG. 1

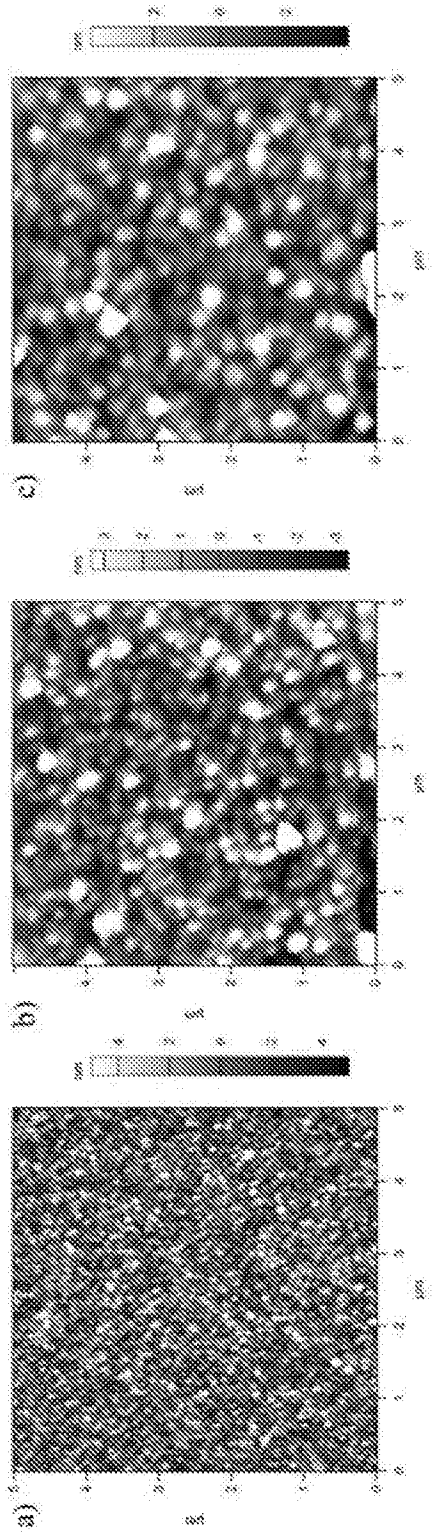

FIG. 2

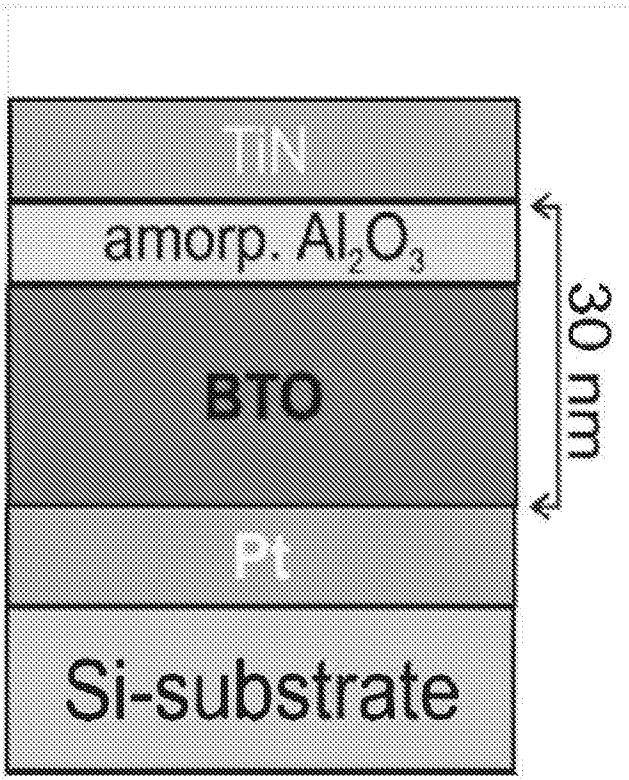

FIG. 3

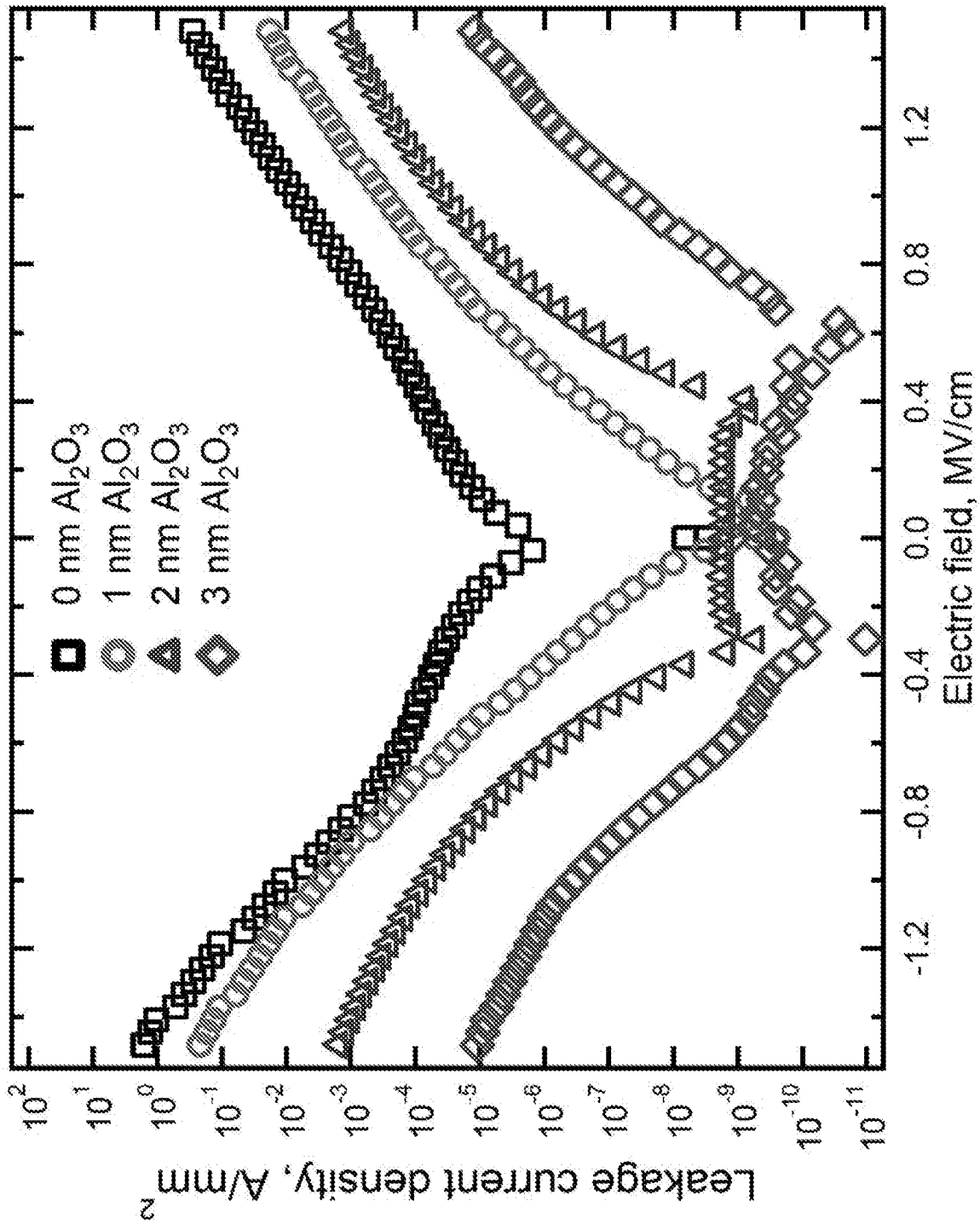
0 nm Al_2O_3
1 nm Al_2O_3
2 nm Al_2O_3
3 nm Al_2O_3
Leakage current density, A/mm^2
Electric field, MV/cm
10^{-2}
10^{-1}
10^{0}
10^{-1}
10^{-2}
10^{-3}
10^{-4}
10^{-5}
10^{-6}
10^{-7}
10^{-8}
10^{-9}
10^{-10}
10^{-11}
-1.2
-0.8
-0.4
0.0
0.4
0.8
1.2

FIG. 4

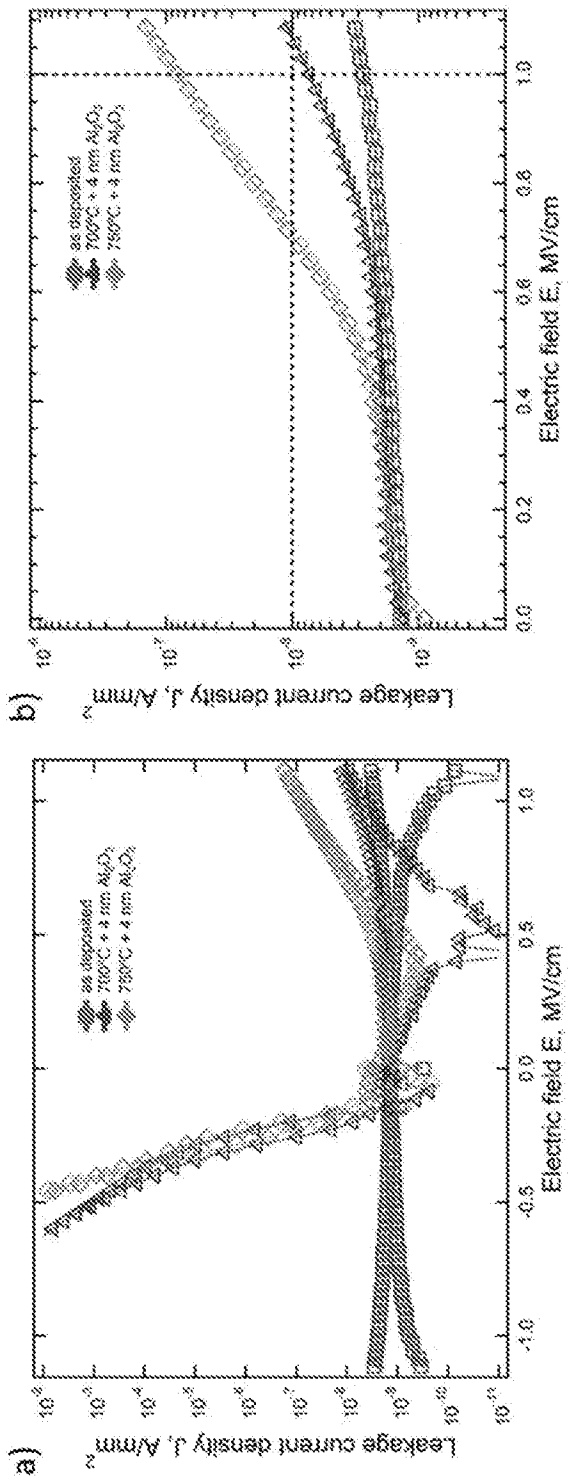
b)
Leakage current density j, A/mm²
Electric field E, MV/cm
as deposited
700°C + 4 nm Al2O3
750°C + 4 nm Al2O3
a)
Leakage current density j, A/mm²
Electric field E, MV/cm
as deposited
700°C + 4 nm Al2O3
750°C + 4 nm Al2O3

FIG. 5

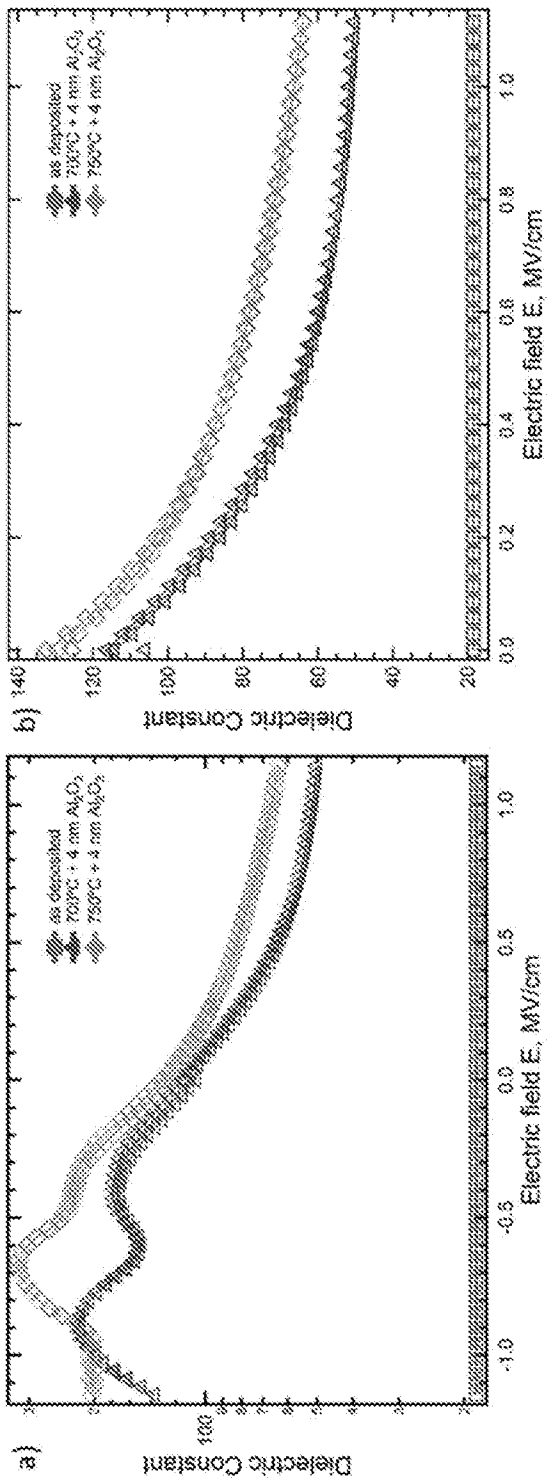
b)
Dielectric Constant
Electric field E, MV/cm
as deposited
750°C + 4 nm Al2O3
760°C + 4 nm Al2O3
a)
Dielectric Constant
Electric field E, MV/cm
as deposited
750°C + 4 nm Al2O3
760°C + 4 nm Al2O3

FIG. 6

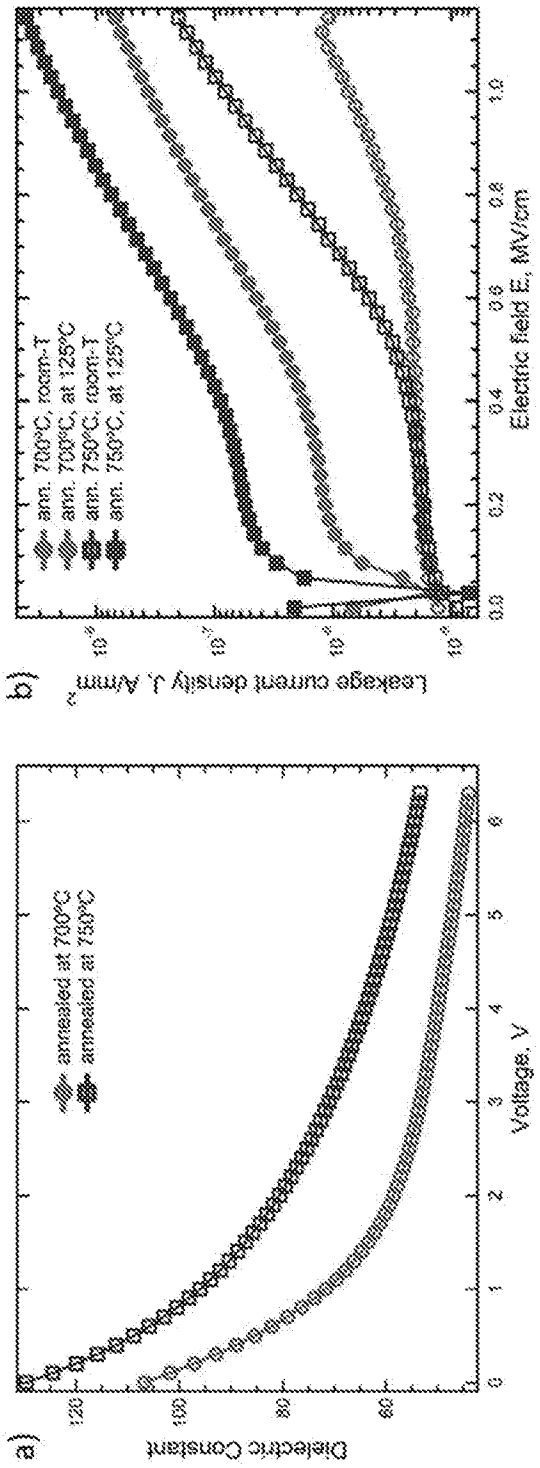
b)
Leakage current density J, A/mm²
Electric field E, MV/cm
ann. 700°C, room-T
ann. 700°C, at 125°C
ann. 750°C, room-T
ann. 750°C, at 125°C
a)
Dielectric Constant
Voltage, V
annealed at 700°C
annealed at 750°C

FIG. 7

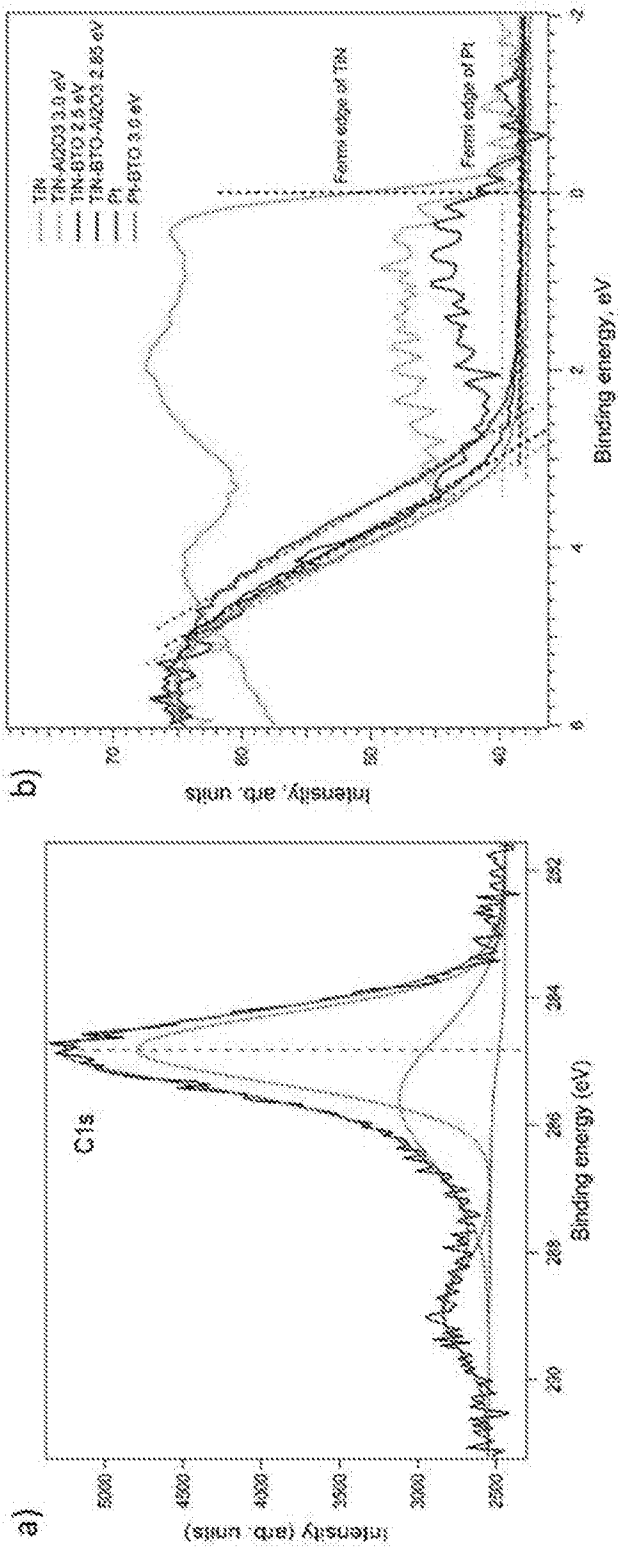
a)
C1s
Intensity (arb. units)
Binding energy (eV)
b)
TiN
TiN-Al2O3 3.0 eV
TiN-BTO 2.5 eV
TiN-BTO-Al2O3 2.85 eV
Pt
Pt-BTO 3.9 eV
Fermi edge of TiN
Fermi edge of Pt
Intensity, arb. units
Binding energy, eV

FIG. 8

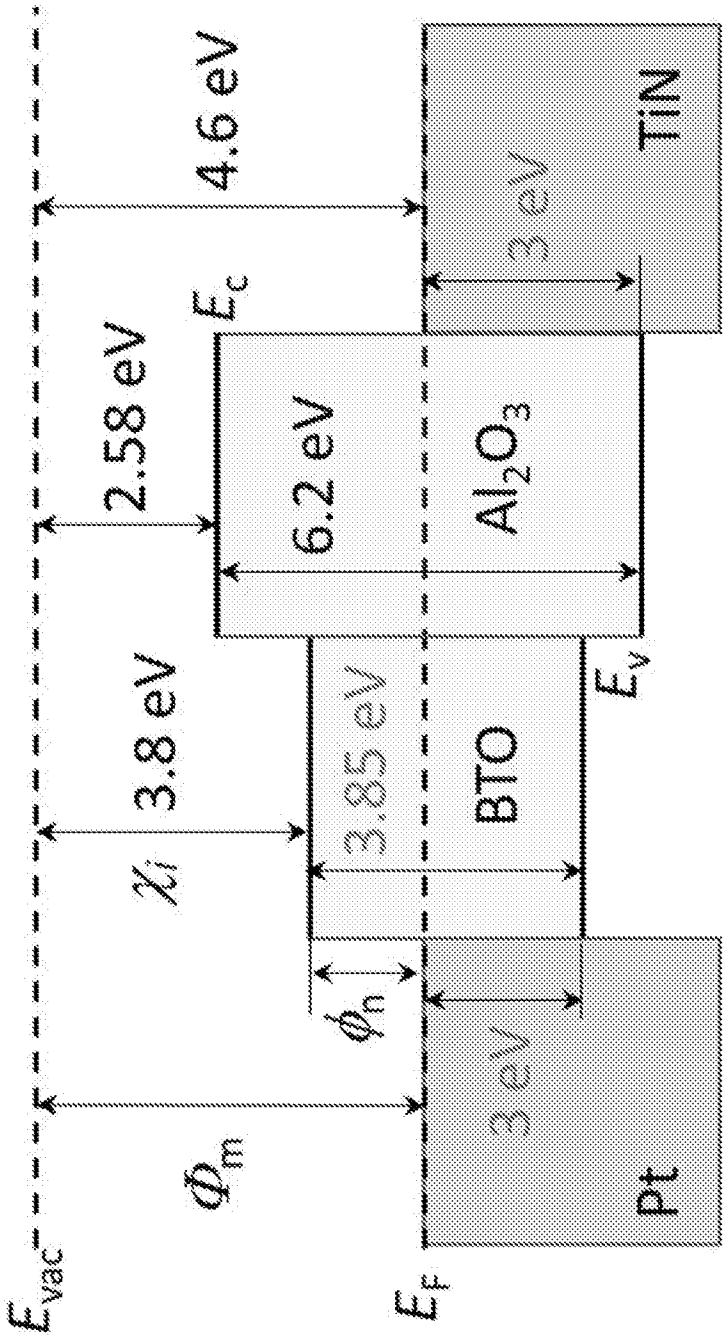
4.6 eV
TiN
3 eV
E_c
2.58 eV
6.2 eV
Al_2O_3
E_v
3.8 eV
3.85 eV
BTO
χ_i
ϕ_n
3 eV
Pt
ϕ_m
E_{vac}
E_F

FIG. 9

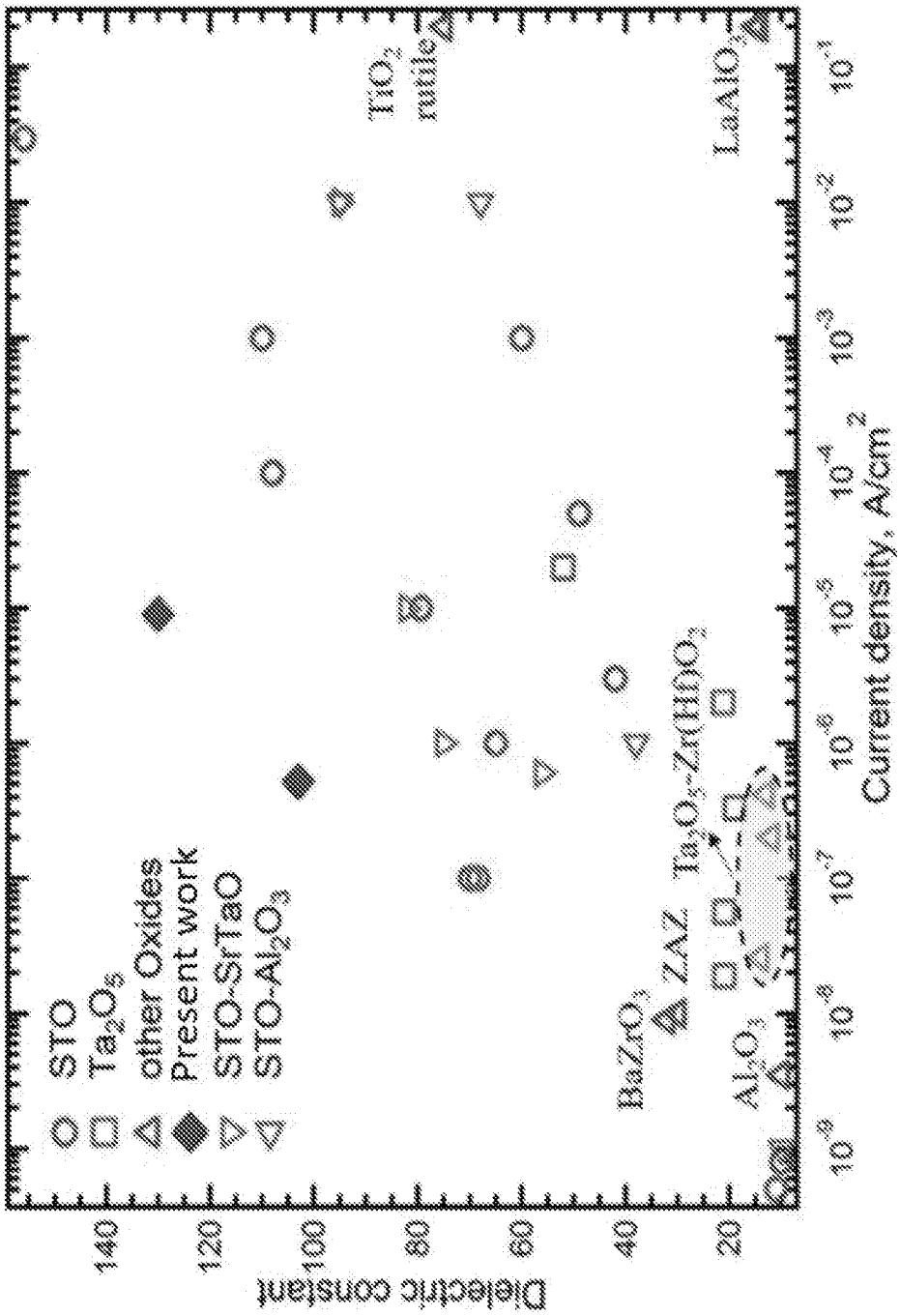
STO
Ta_2O_5
other Oxides
Present work
STO-SrTaO
STO-Al_2O_3
TiO_2 rutile
$LaAlO_3$
$BaZrO_3$
ZAZ
Ta_2O_5-$Zr(Hf)O_2$
Al_2O_3
Au
Dielectric constant
Current density, A/cm^2

FIG. 10

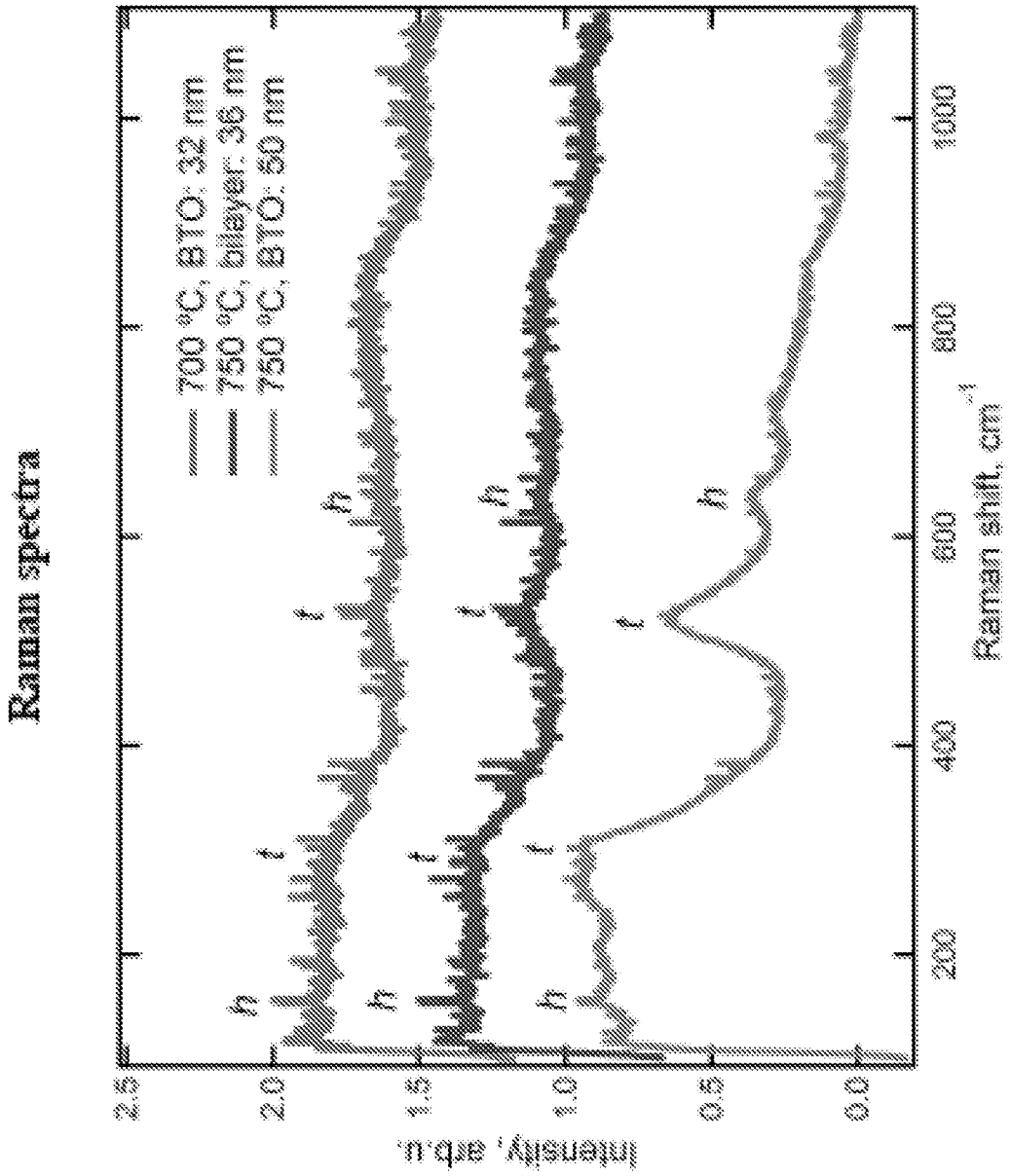
Raman spectra
700 °C, BTO: 32 nm
750 °C, bilayer: 36 nm
750 °C, BTO: 50 nm
h
t
Intensity, arb.u.
Raman shift, cm-1
0.0
0.5
1.0
1.5
2.0
2.5
200
400
600
800
1000

FIG. 11

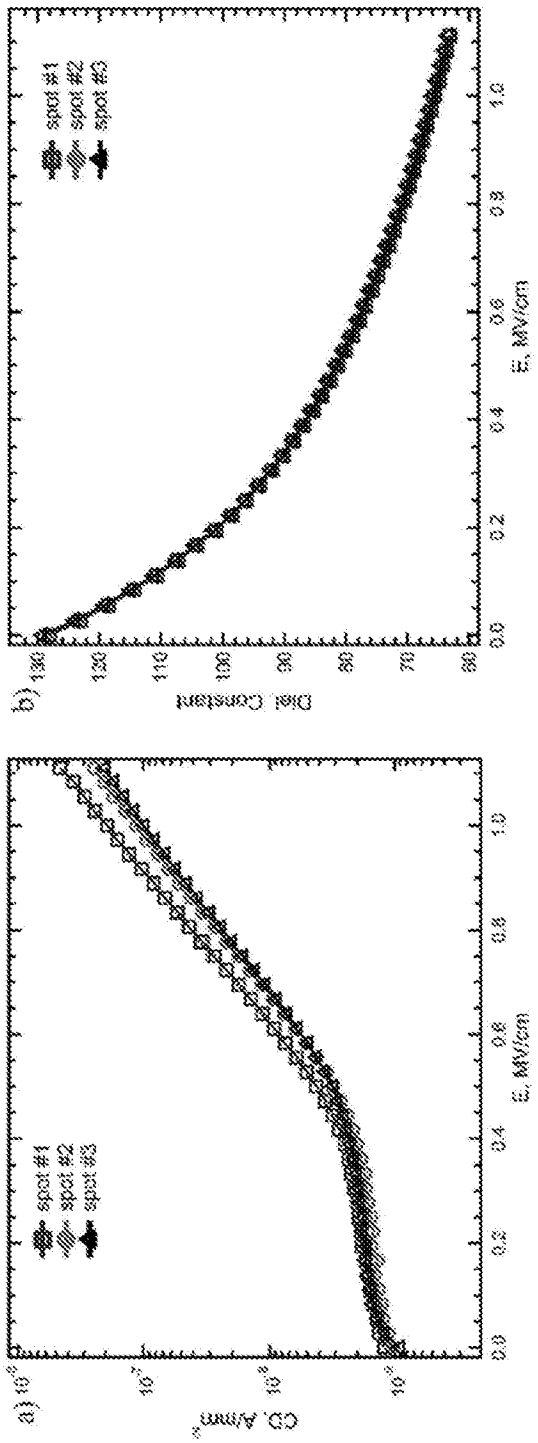
(b)
Die Constant
E, MV/cm
spot #1
spot #2
spot #3
(a)
CD, A/mm²
E, MV/cm
spot #1
spot #2
spot #3

FIG. 12

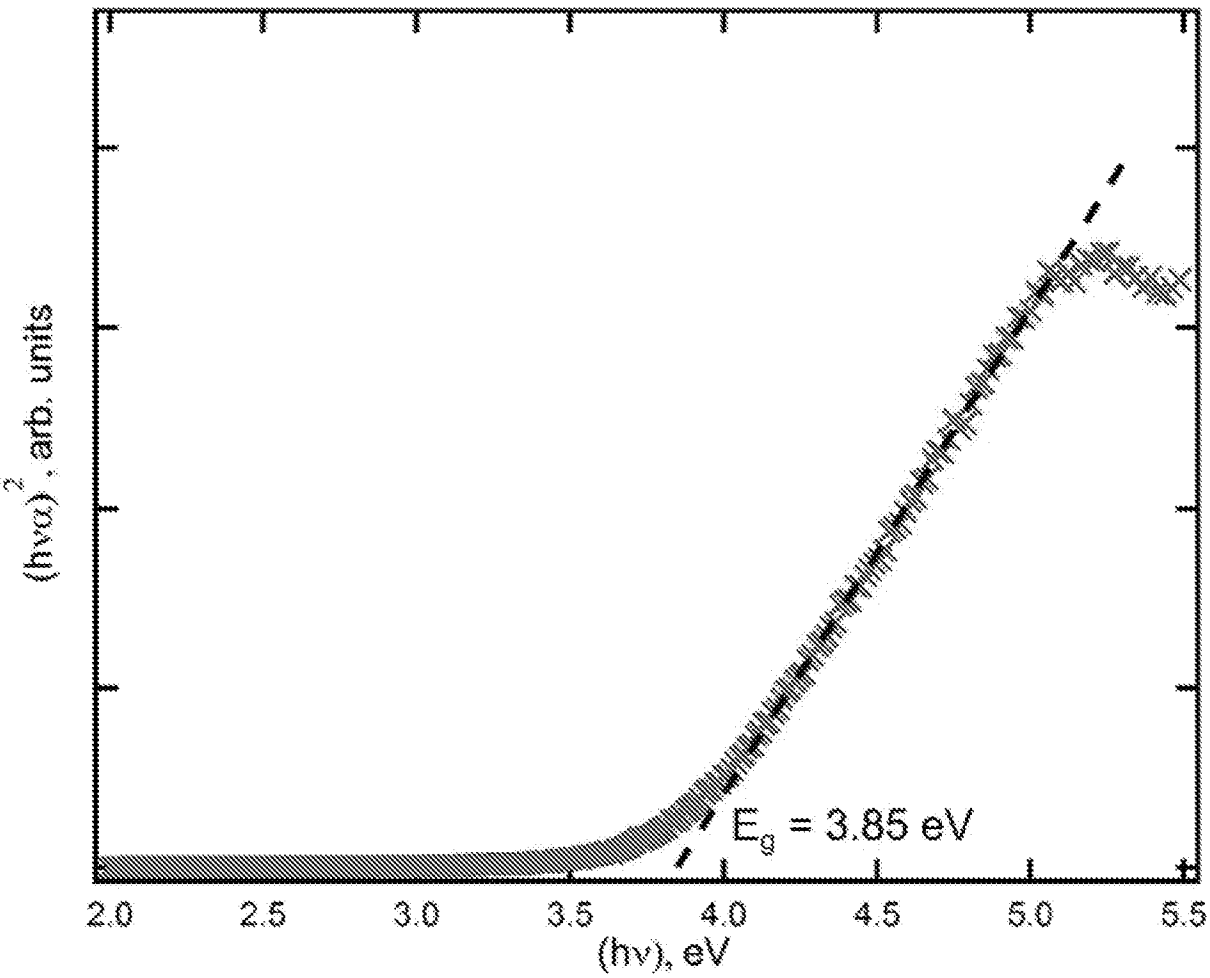

FIG. 13

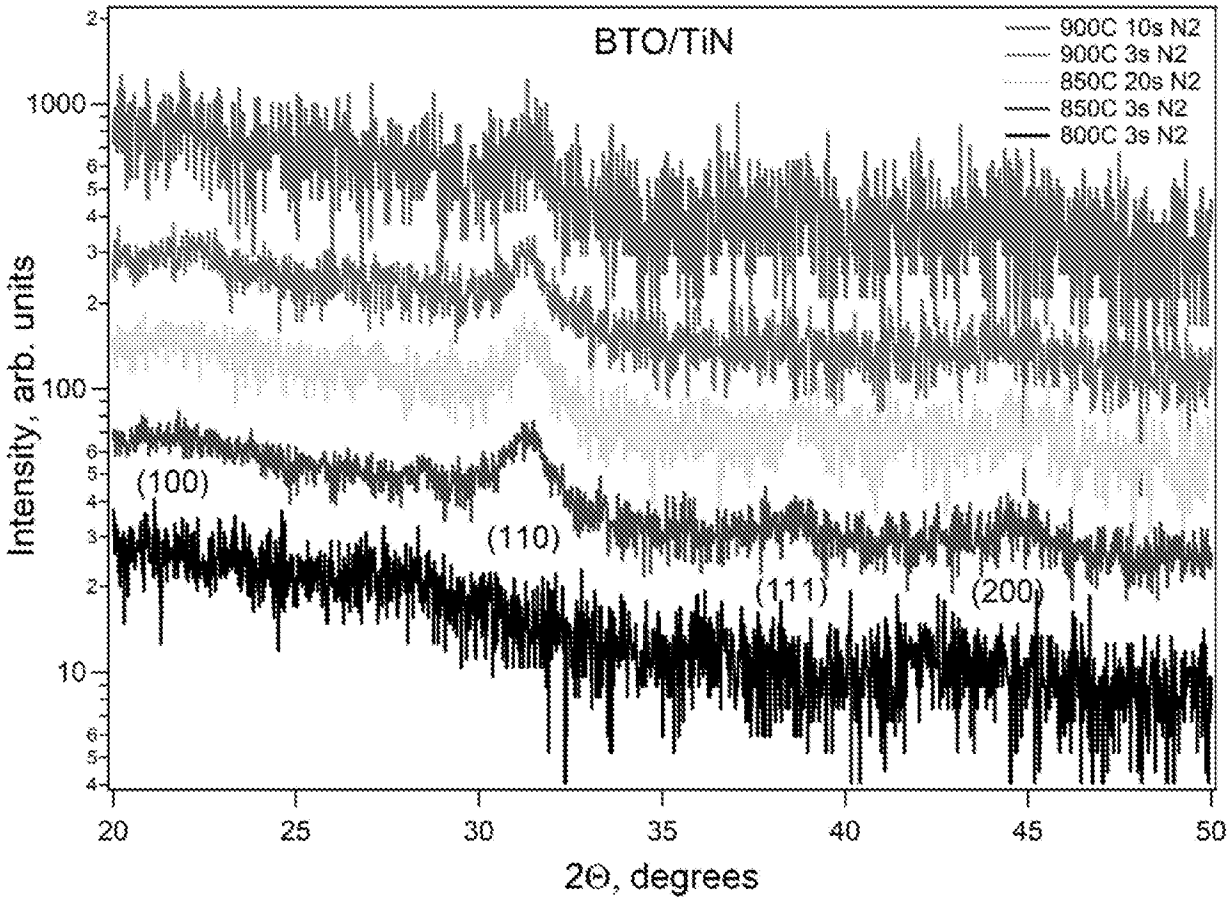
BTO/TiN
900C 10s N2
900C 3s N2
850C 20s N2
850C 3s N2
800C 3s N2
Intensity, arb. units
2Θ, degrees
(100)
(110)
(111)
(200)
1000
100
10
20
25
30
35
40
45
50

Figure 14

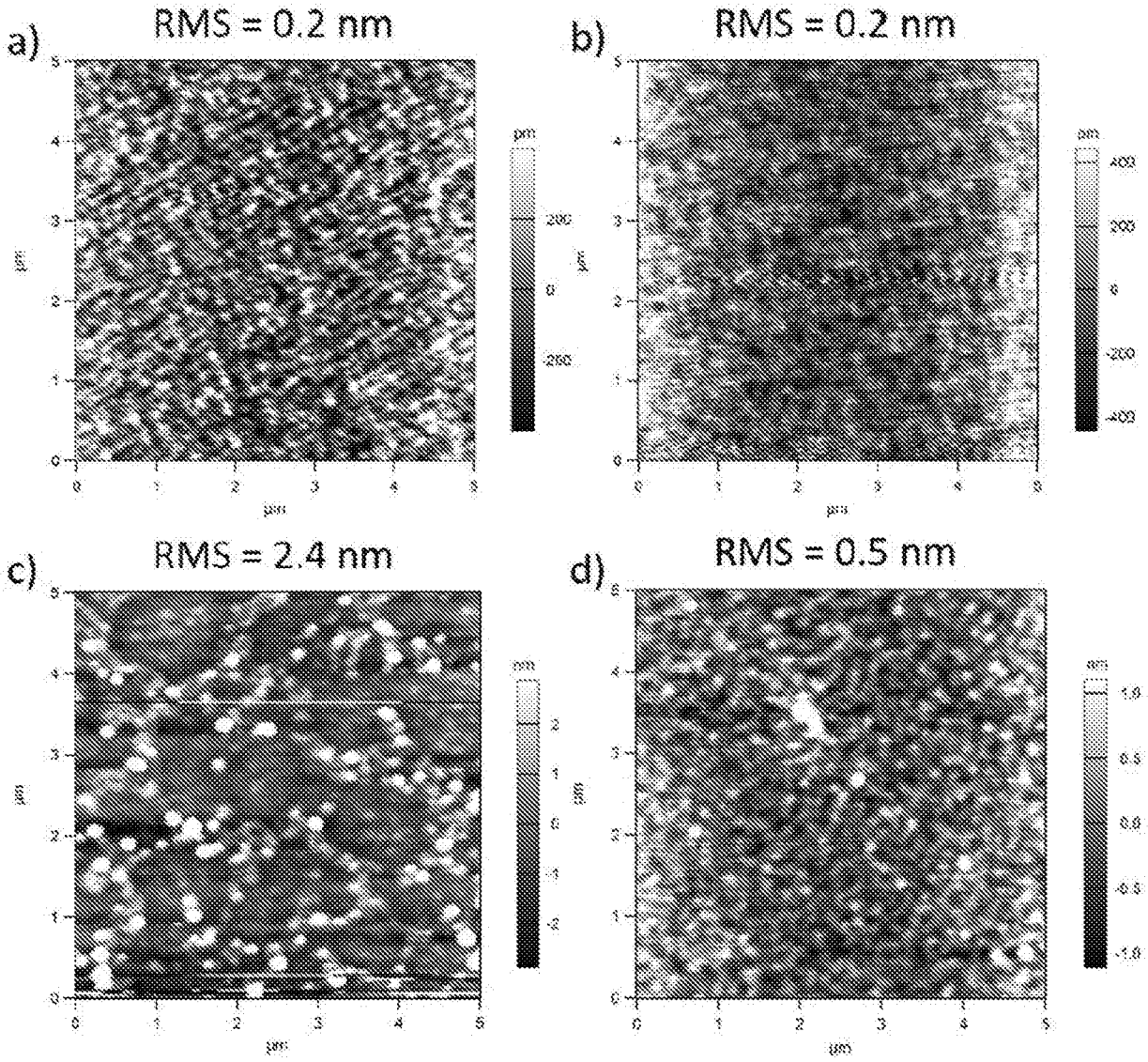

Figure 15

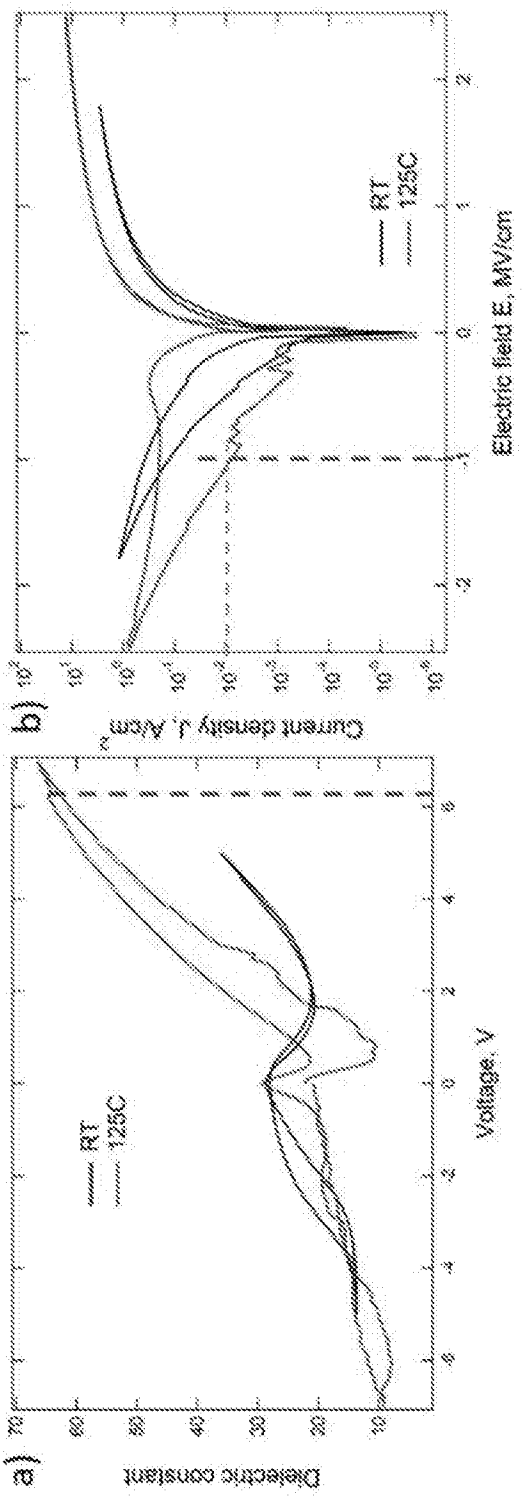
a)
Dielectric constant
Voltage, V
RT
125C
b)
Current density J, A/cm²
Electric field E, MV/cm
RT
125C

Figure 16

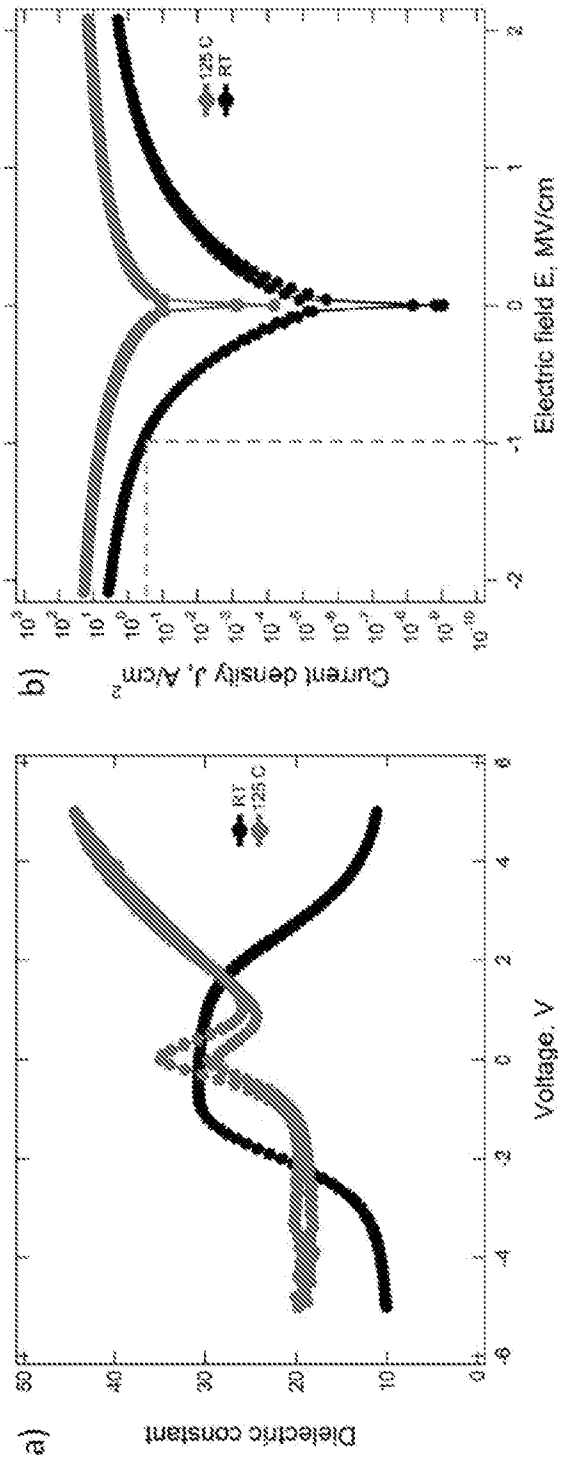
a)
Dielectric constant
Voltage, V
RT
125 C
b)
Current density J, A/cm²
Electric field E, MV/cm
125 C
RT

Figure 17

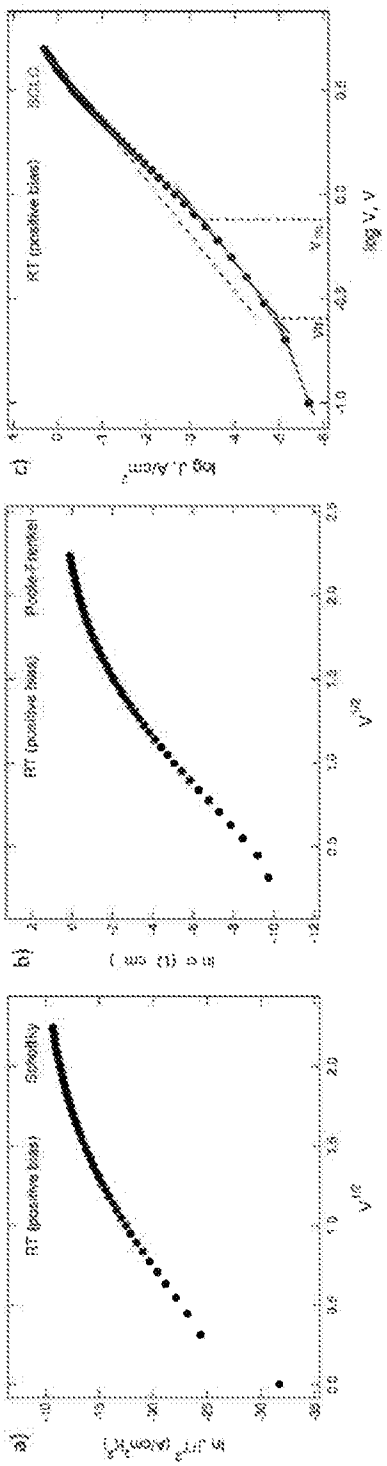
RT (positive bias)
RT (positive bias)
RT (positive bias)
Schottky
Poole-Frenkel
Poole-Frenkel
Schottky
Schottky
log J, A/cm²
ln σ (Ω⁻¹ cm⁻¹)
ln J/T² (A/cm²K²)
V, V
V^1/2
V^1/2
V^1/2

Figure 18

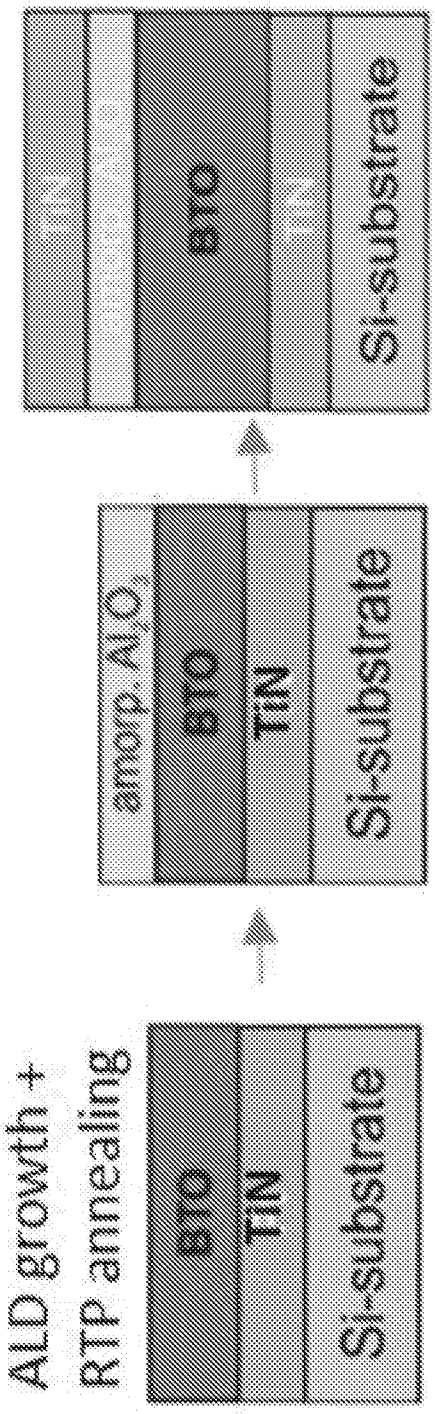
ALD growth +
RTP annealing
BTO
TiN
Si-substrate
amorp. AlO_x
BTO
TiN
Si-substrate
BTO
Si-substrate

Figure 19

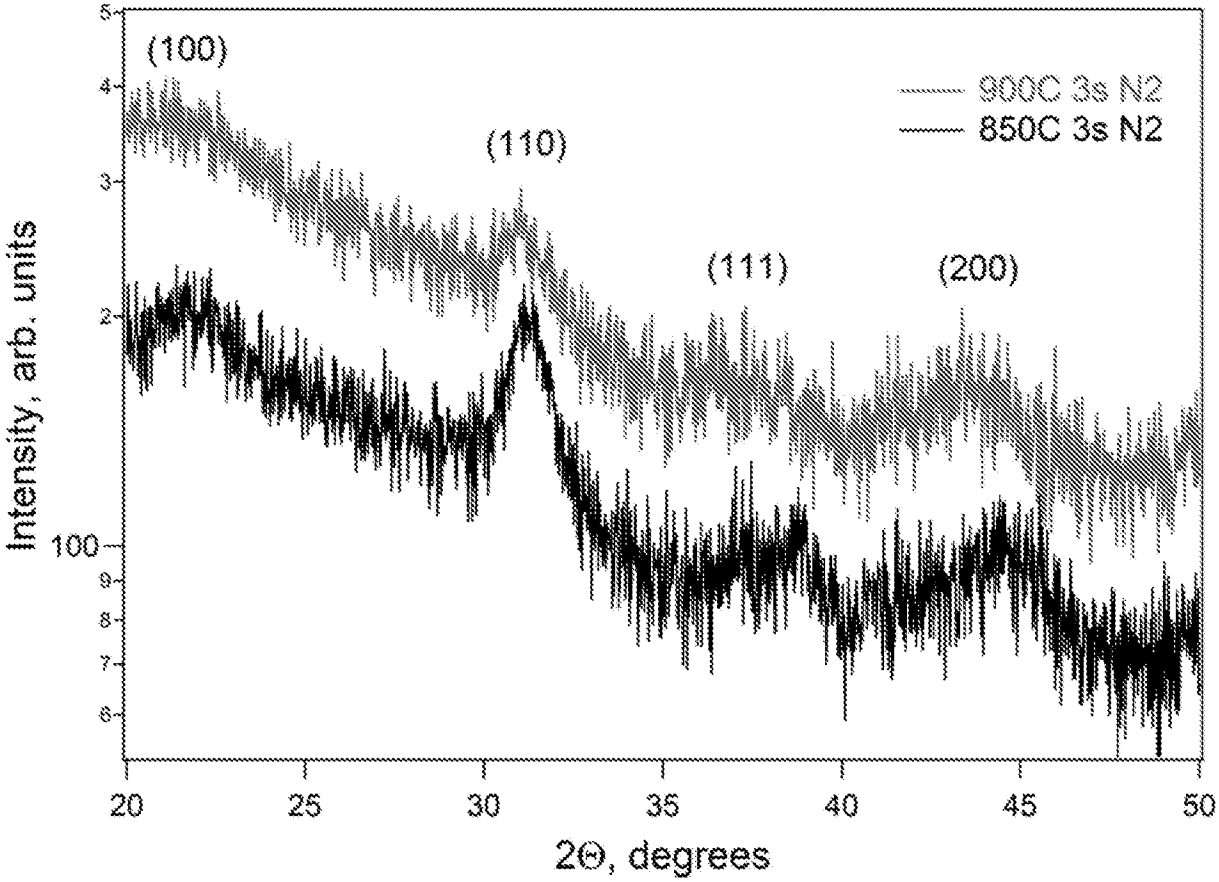
(100)
(110)
(111)
(200)
900C 3s N2
850C 3s N2
Intensity, arb. units
2Θ, degrees
20
25
30
35
40
45
50

Figure 20

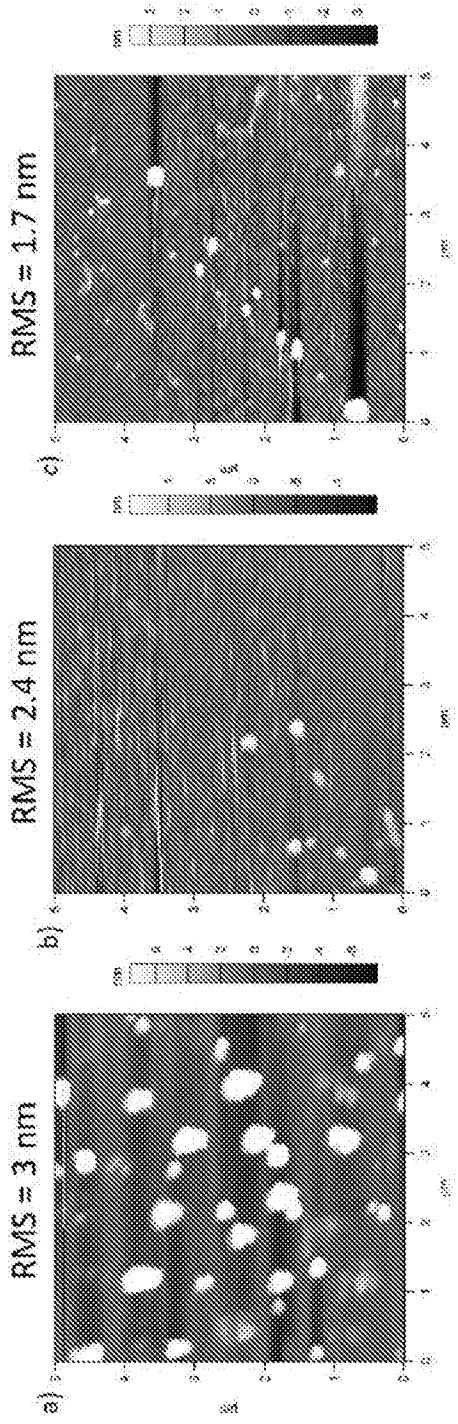

Figure 21

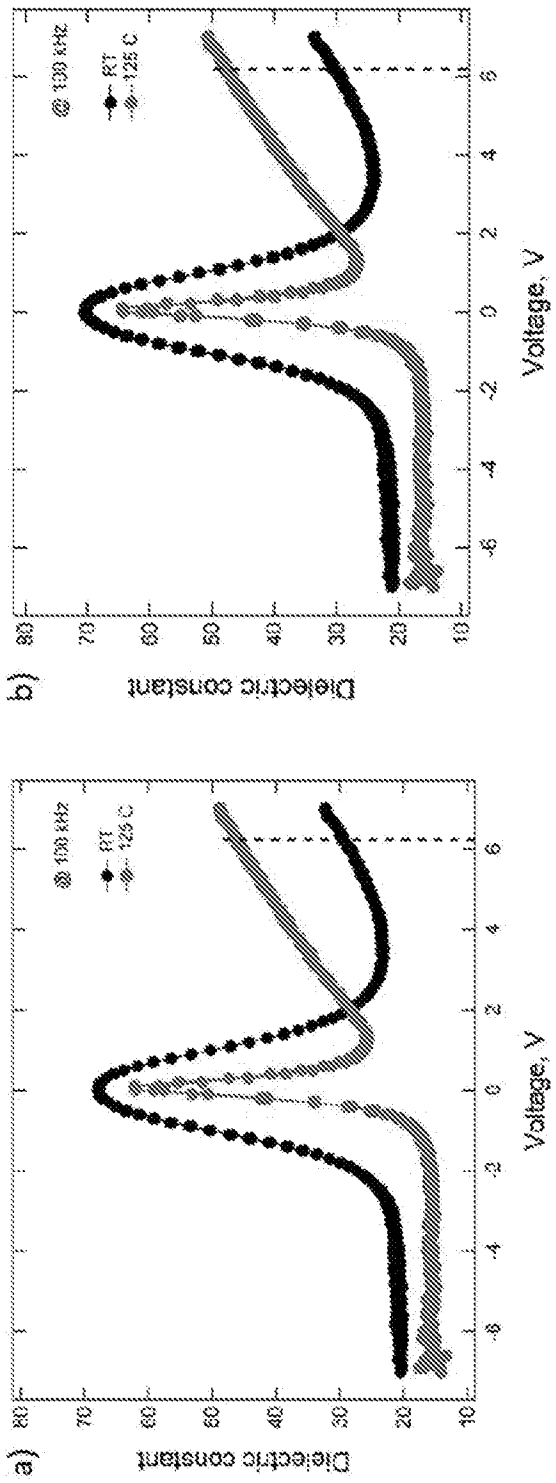
b)
Dielectric constant
Voltage, V
@ 100 kHz
RT
125 C
a)
Dielectric constant
Voltage, V
@ 100 kHz
RT
125 C

Figure 22

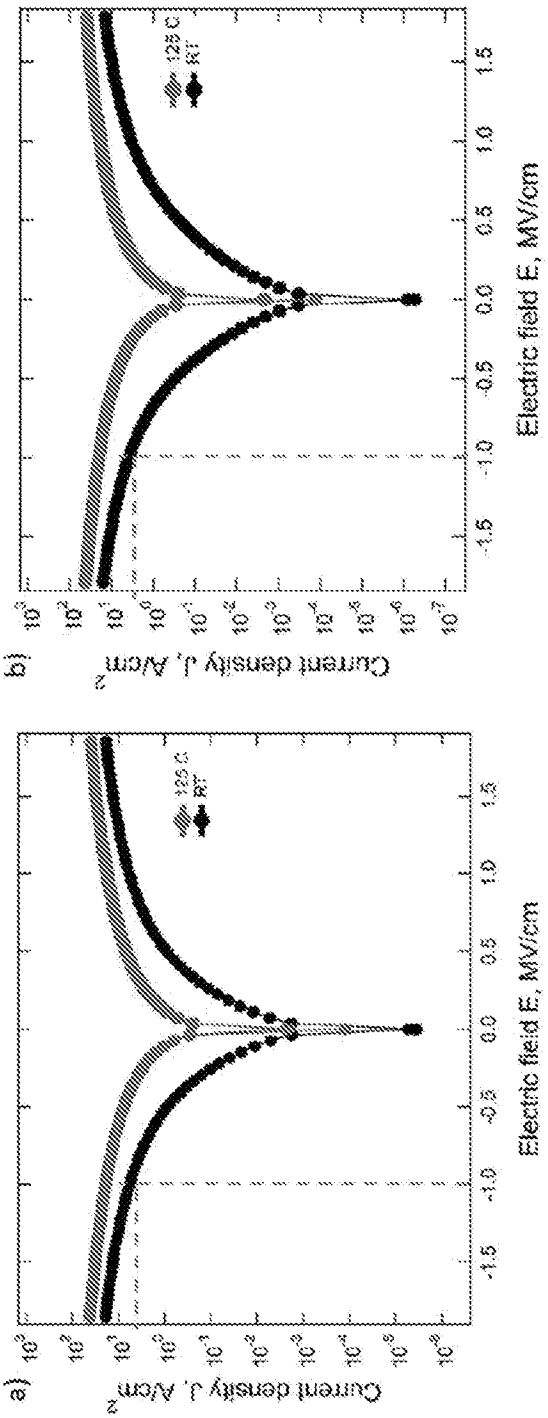
b)
Current density J, A/cm²
Electric field E, MV/cm
125 C
RT
a)
Current density J, A/cm²
Electric field E, MV/cm
125 C
RT

Figure 23

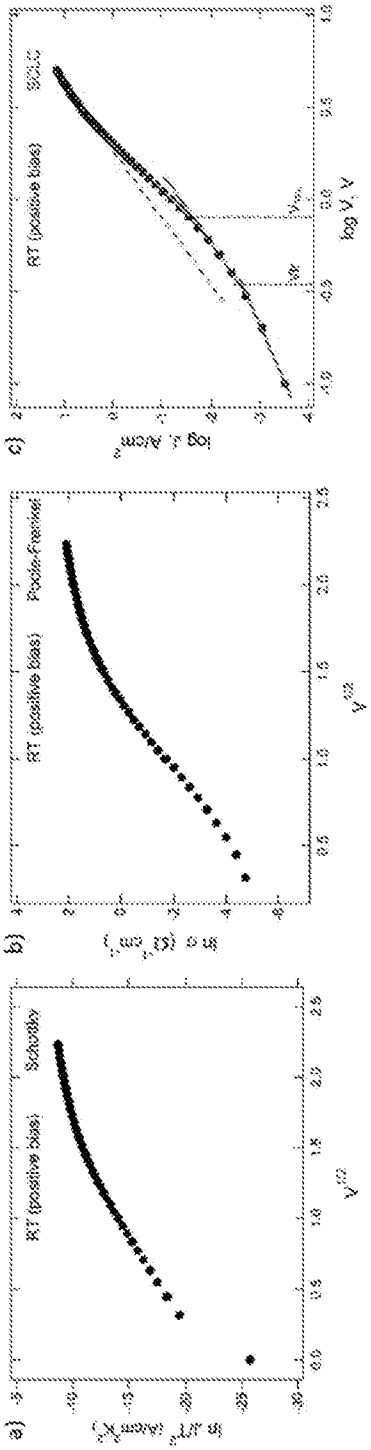
a)
RT (positive bias)
Schottky
b)
RT (positive bias)
Poole-Frenkel
c)
RT (positive bias)
SCLC

Figure 24

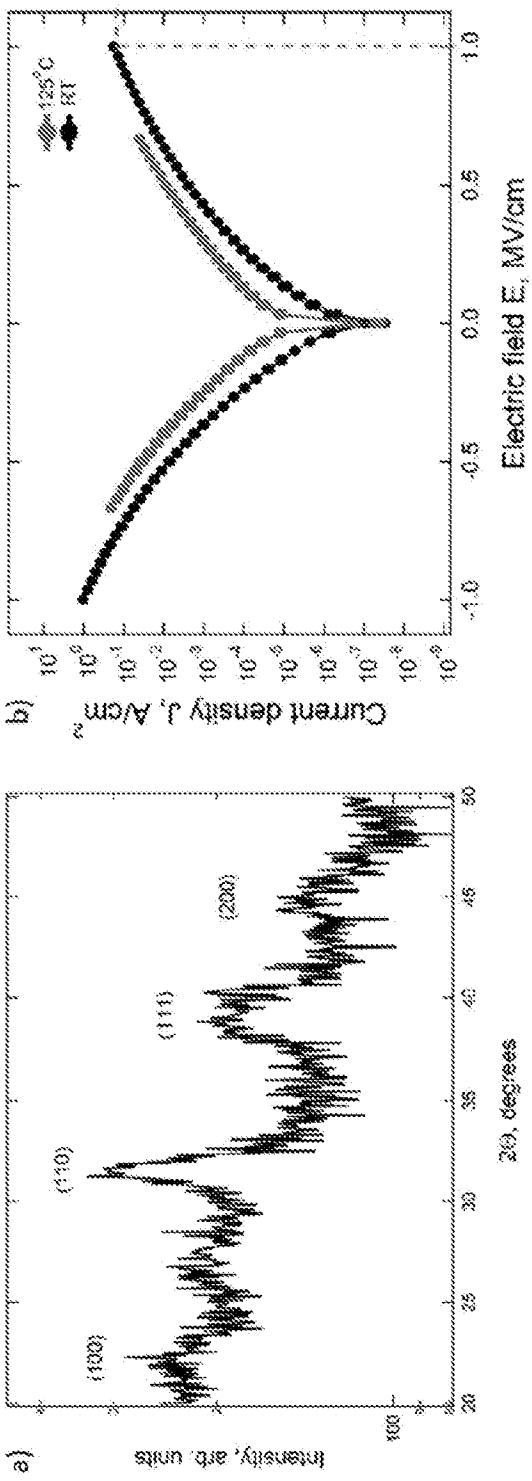
b)
Current density j, A/cm²
Electric field E, MV/cm
135°C
RT
a)
Intensity, arb. units
2θ, degrees
(100)
(110)
(111)
(200)

Figure 25

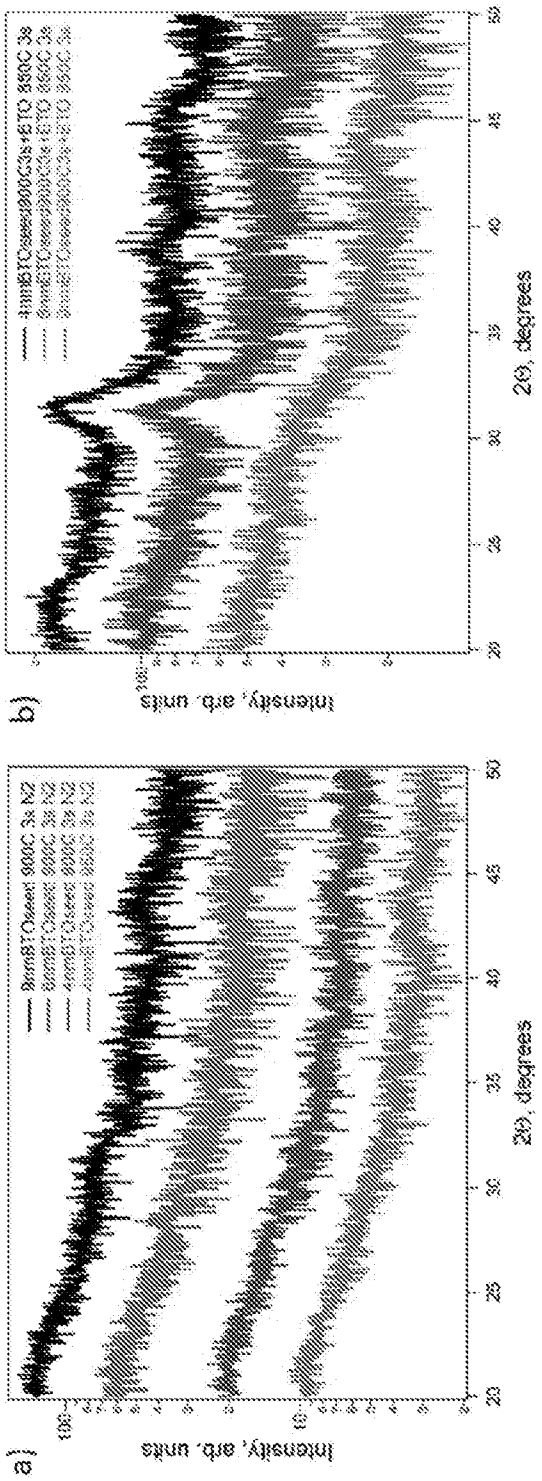
b)
Intensity, arb. units
2θ, degrees
a)
Intensity, arb. units
2θ, degrees

Figure 26

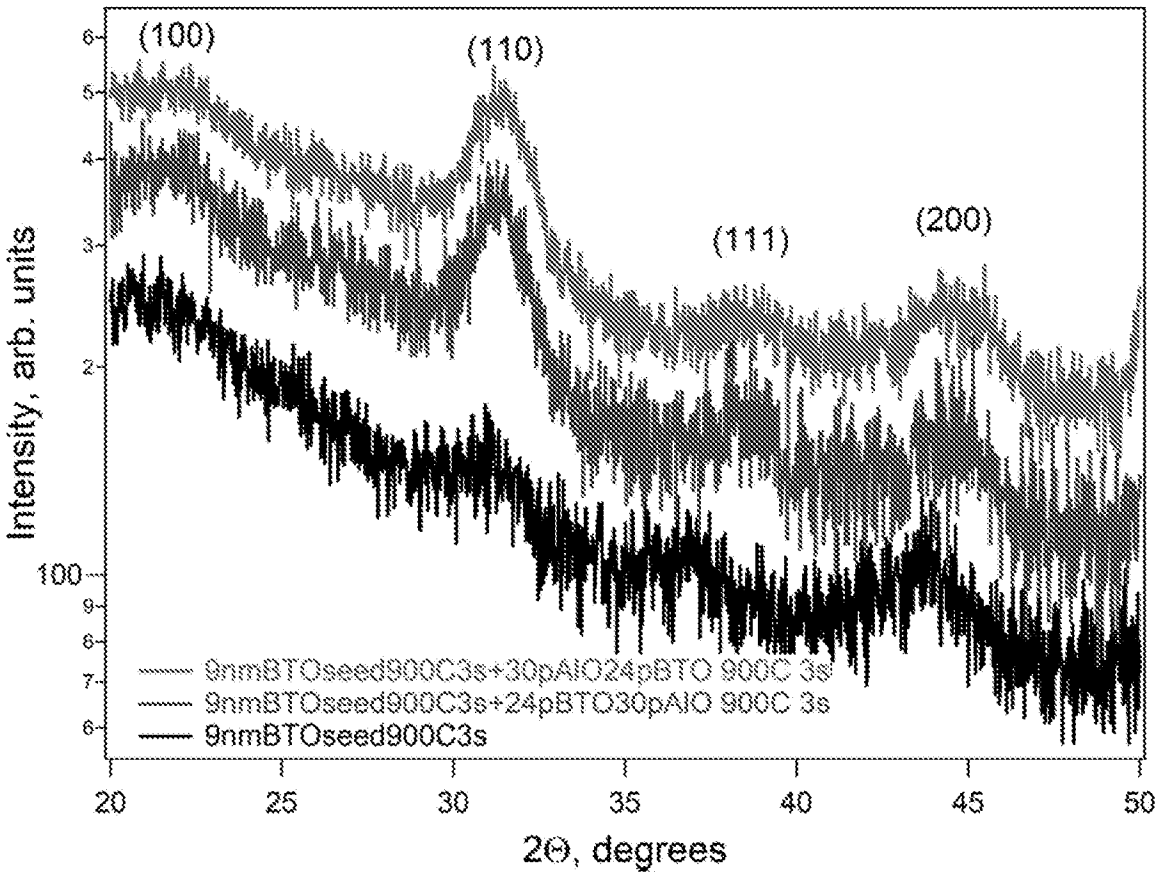
(100)
(110)
(111)
(200)
Intensity, arb. units
100
9nmBTOseed900C3s+30pAlO24pBTO 900C 3s
9nmBTOseed900C3s+24pBTO30pAlO 900C 3s
9nmBTOseed900C3s
20
25
30
35
40
45
50
2Θ, degrees

Figure 27

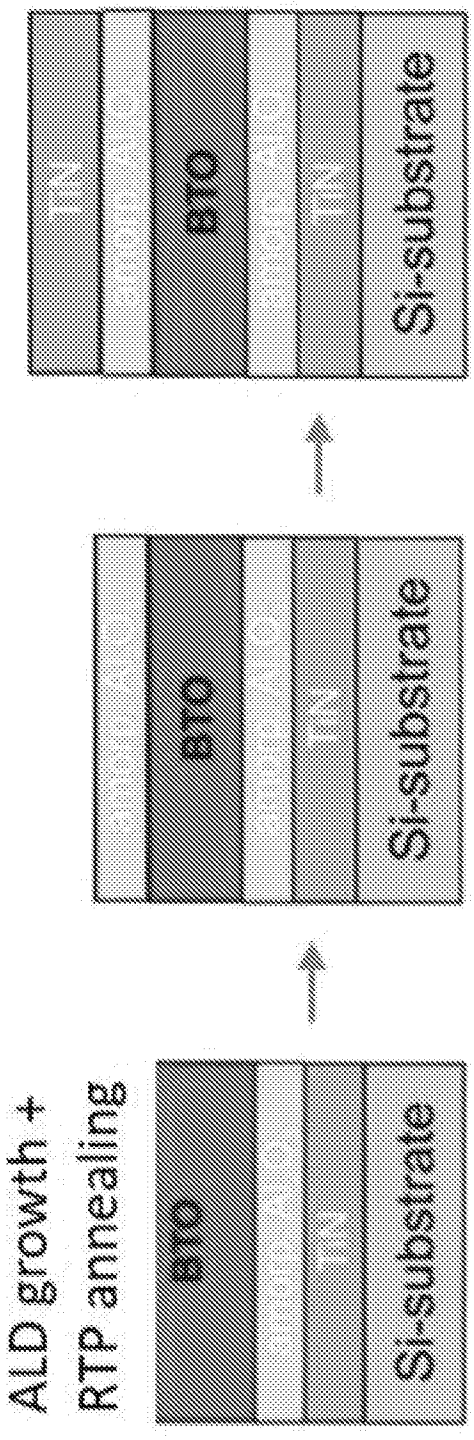
ALD growth +
RTP annealing
BTO
Si-substrate
BTO
Si-substrate
BTO
Si-substrate

Figure 28

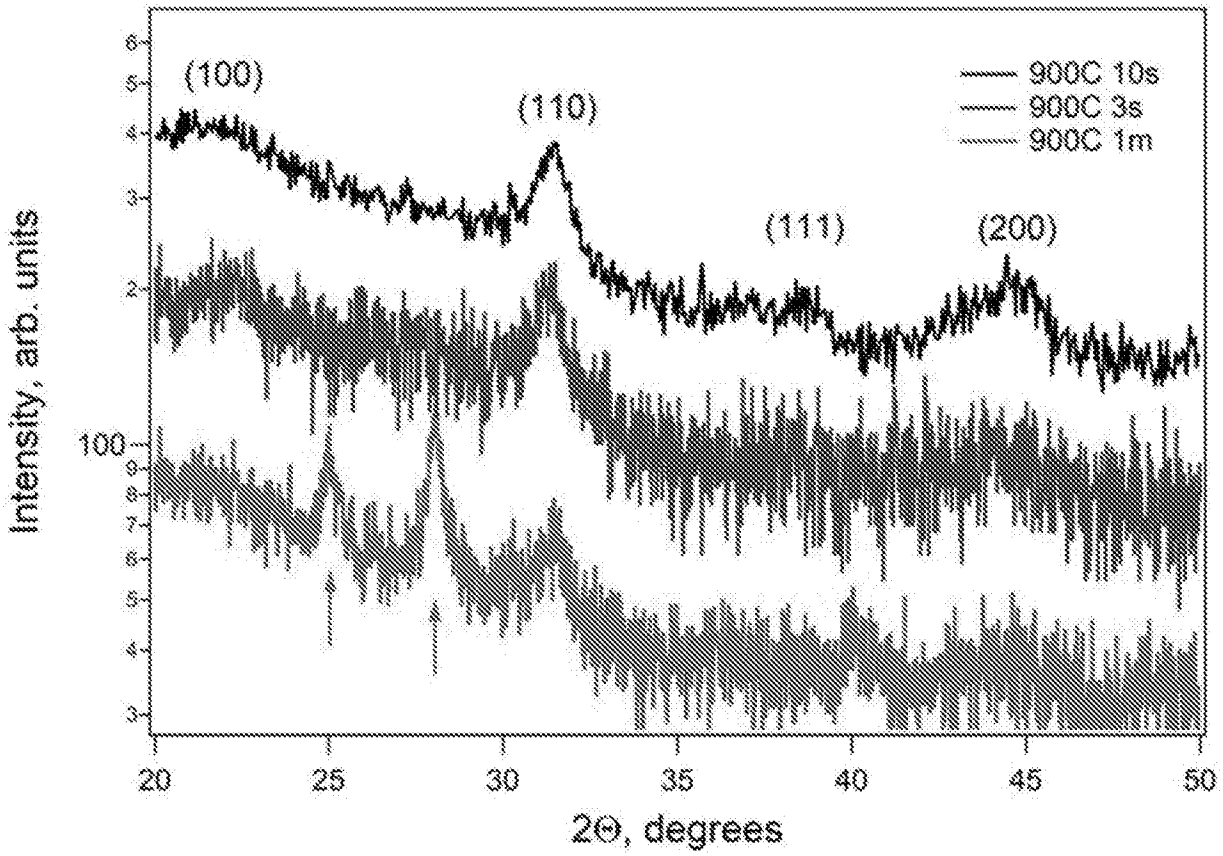
(100)
(110)
(111)
(200)
900C 10s
900C 3s
900C 1m
Intensity, arb. units
100
20
25
30
35
40
45
50
2Θ, degrees

Figure 29

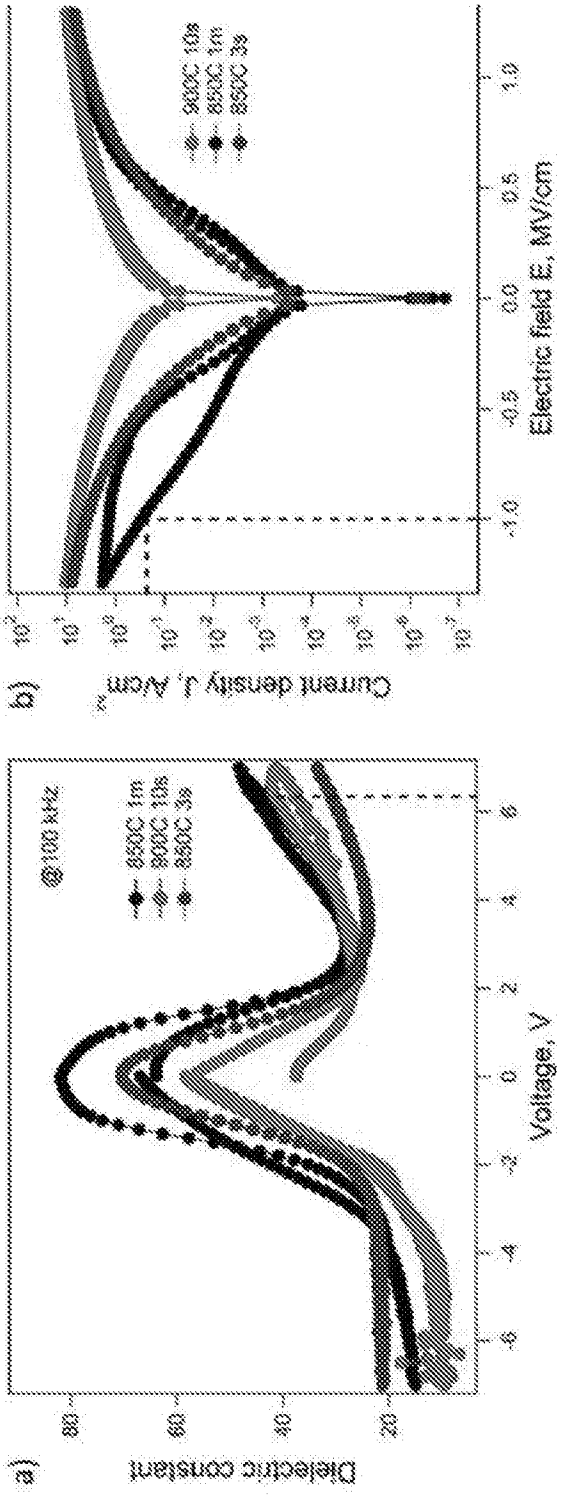
b)
Current density J, A/cm²
Electric field E, MV/cm
900C 15s
850C 1m
850C 3s
a)
Dielectric constant
Voltage, V
@100 kHz
850C 1m
800C 15s
850C 3s

Figure 30

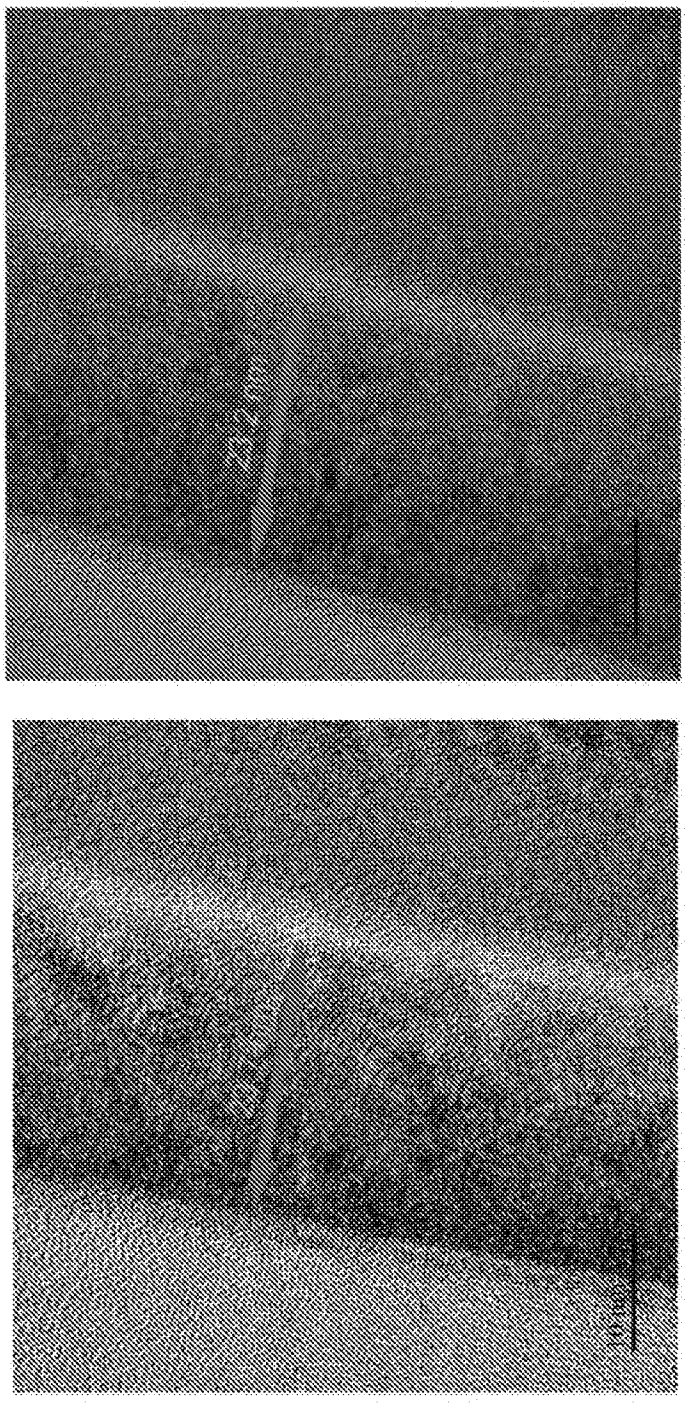

Figure 31

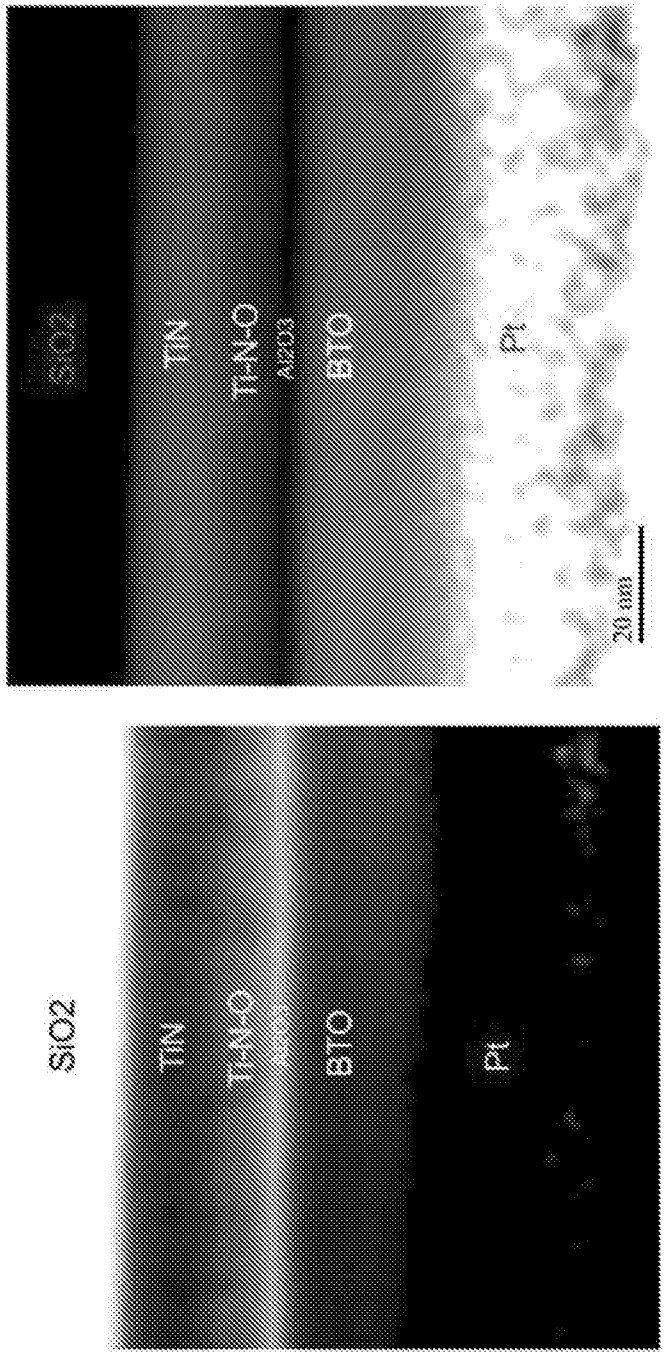

Figure 32

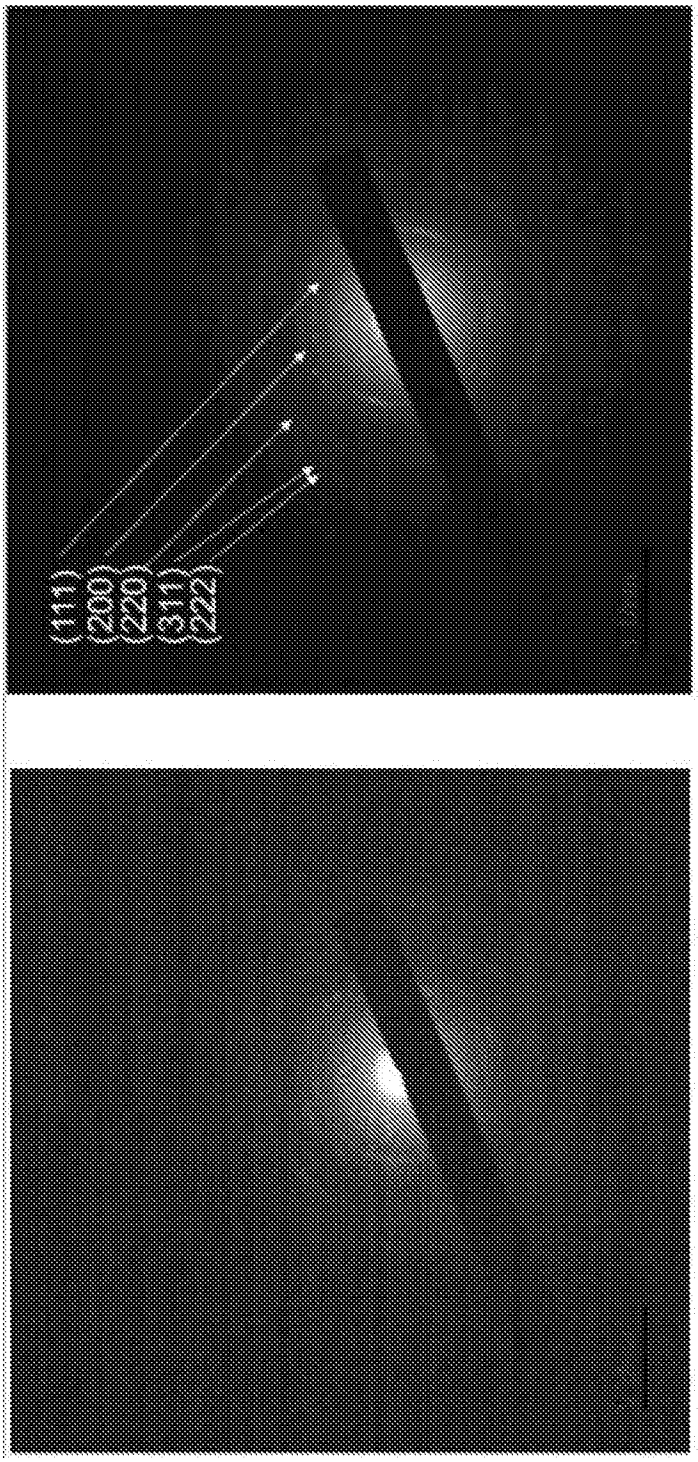

Figure 33

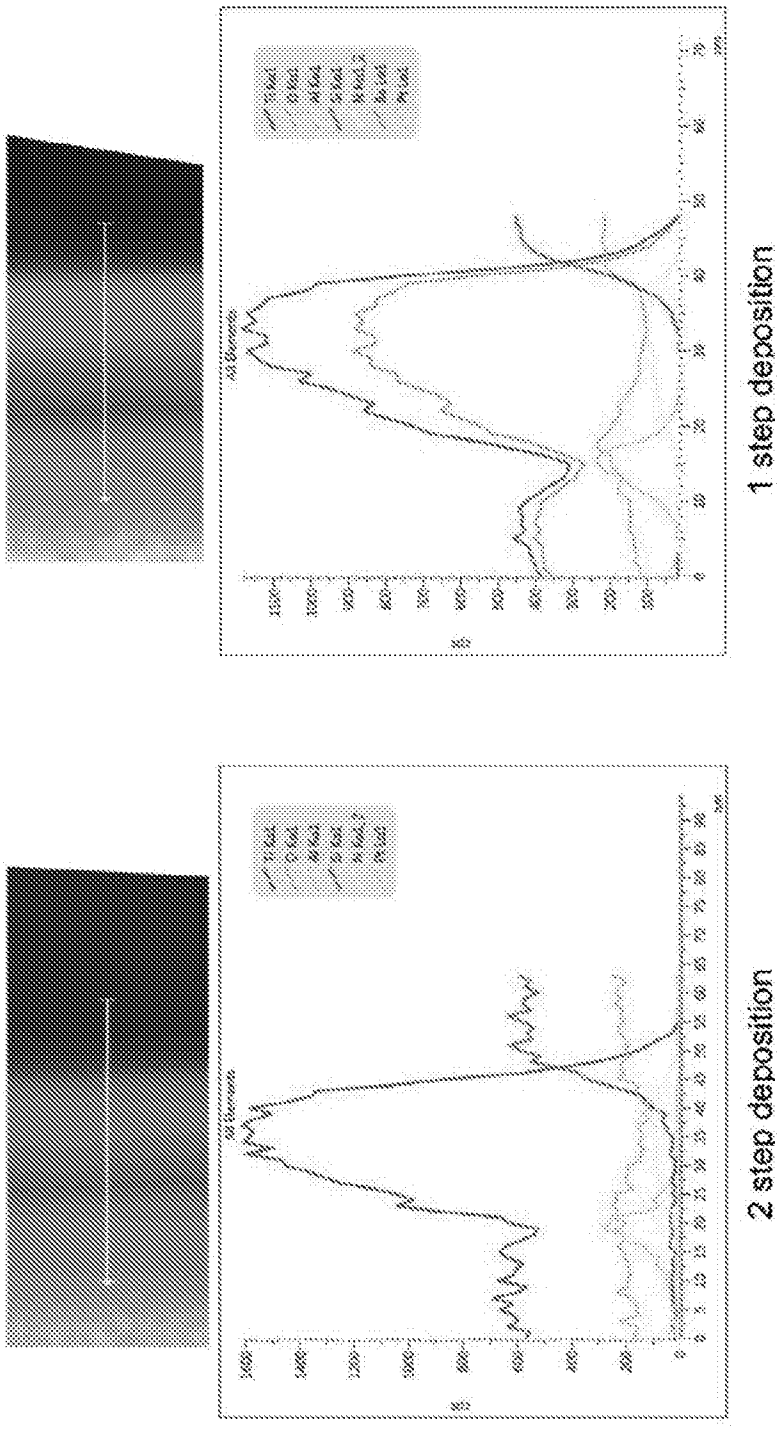

Figure 34

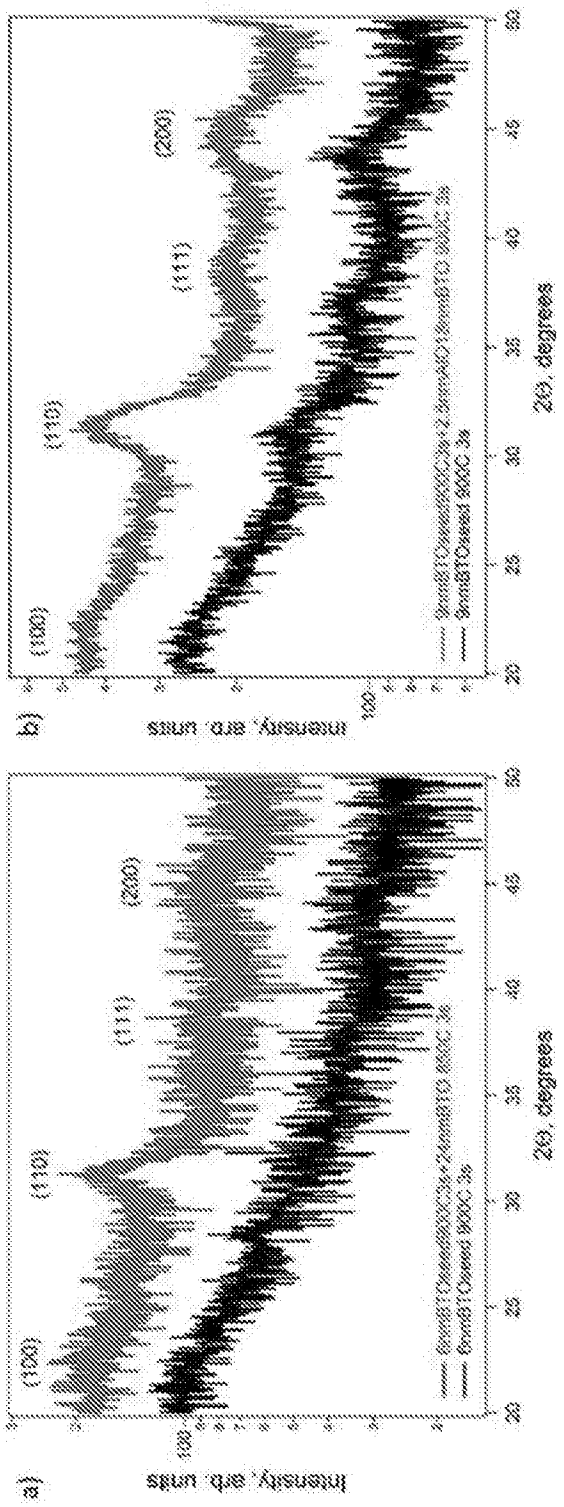

Figure 35

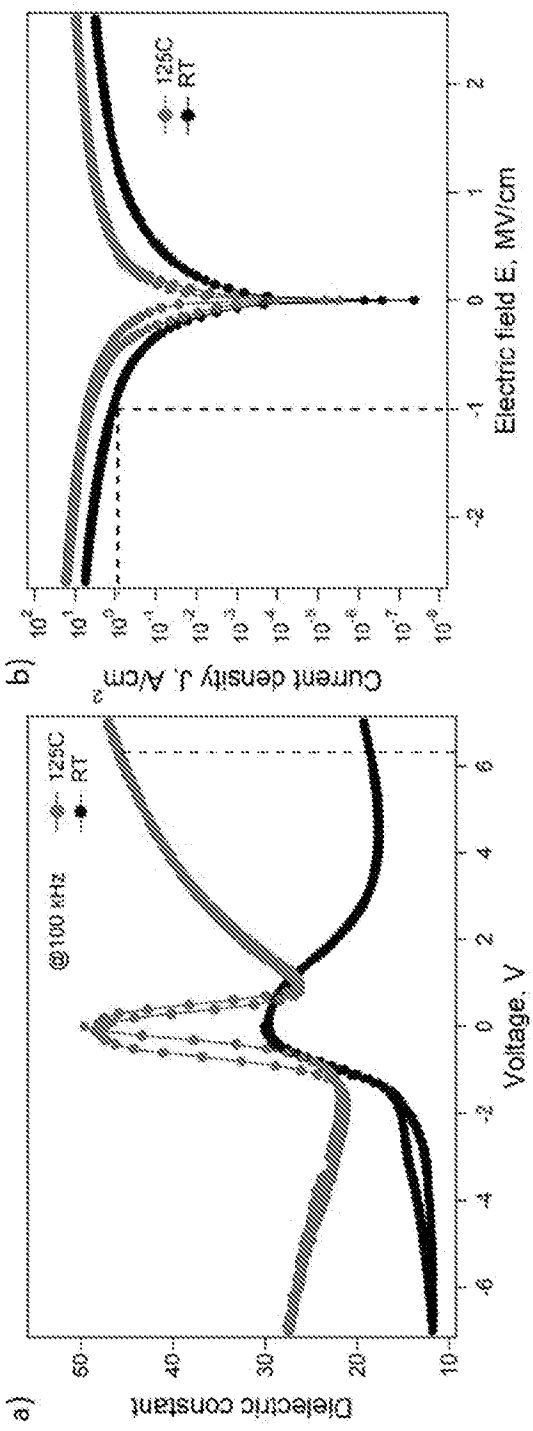
a)
Dielectric constant
@100 kHz
125C
RT
Voltage, V
b)
Current density J, A/cm²
125C
RT
Electric field E, MV/cm

Figure 36

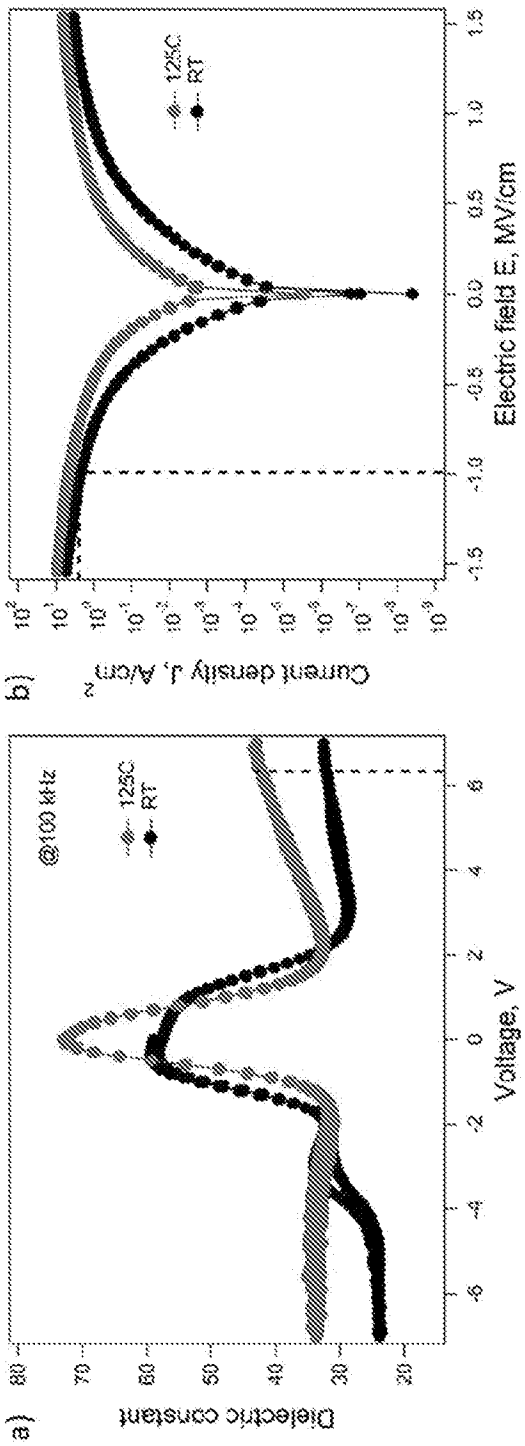
a)
Dielectric constant
@100 kHz
125C
RT
Voltage, V
b)
Current density J, A/cm2
125C
RT
Electric field E, MV/cm

Figure 37

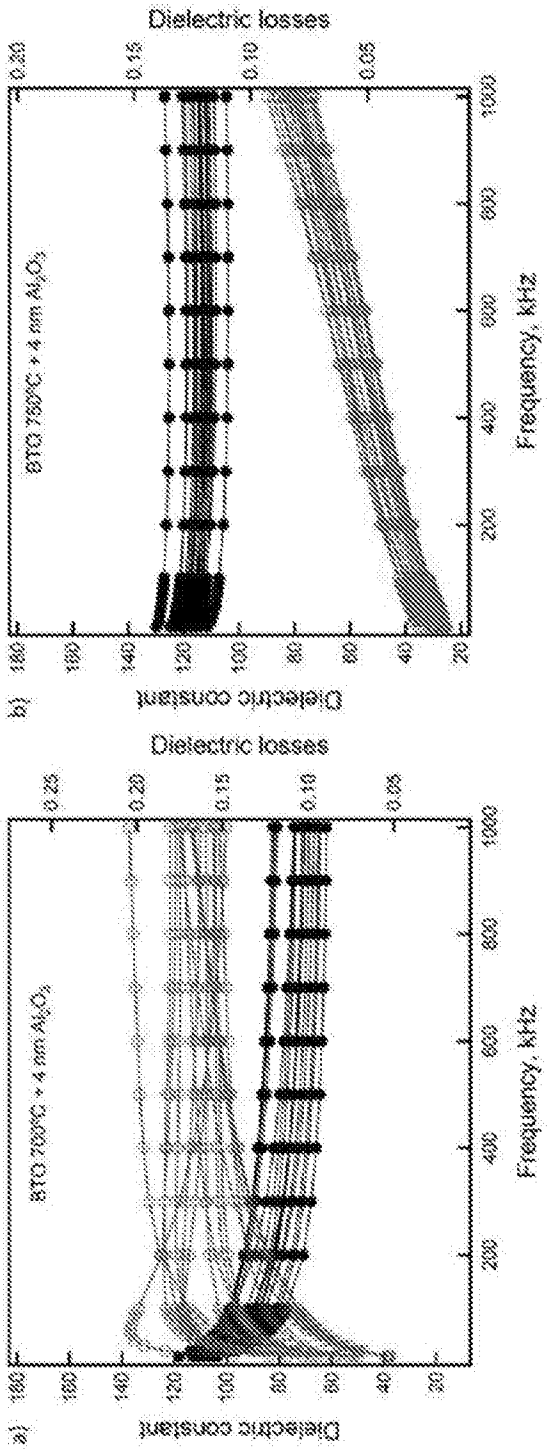
Dielectric losses
0.20
0.15
0.10
0.05
BTO 750°C + 4 nm Al_2O_3
1000
800
600
400
200
Frequency, kHz
160
140
120
100
80
60
40
20
Dielectric constant
b)
Dielectric losses
0.25
0.20
0.15
0.10
0.05
BTO 750°C + 4 nm Al_2O_3
1000
800
600
400
200
Frequency, kHz
160
140
120
100
80
60
40
20
Dielectric constant
a)

Figure 38

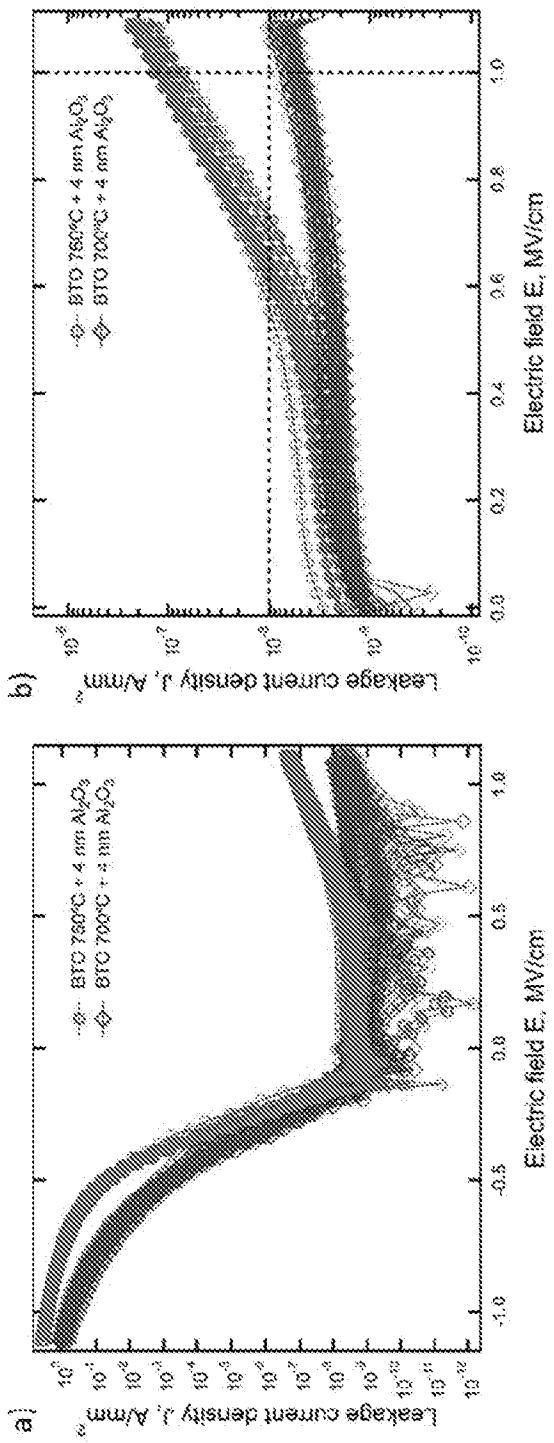
a)
b)
Leakage current density J, A/mm²
Electric field E, MV/cm
BTO 750°C + 4 nm Al2O3
BTO 700°C + 4 nm Al2O3

Figure 39

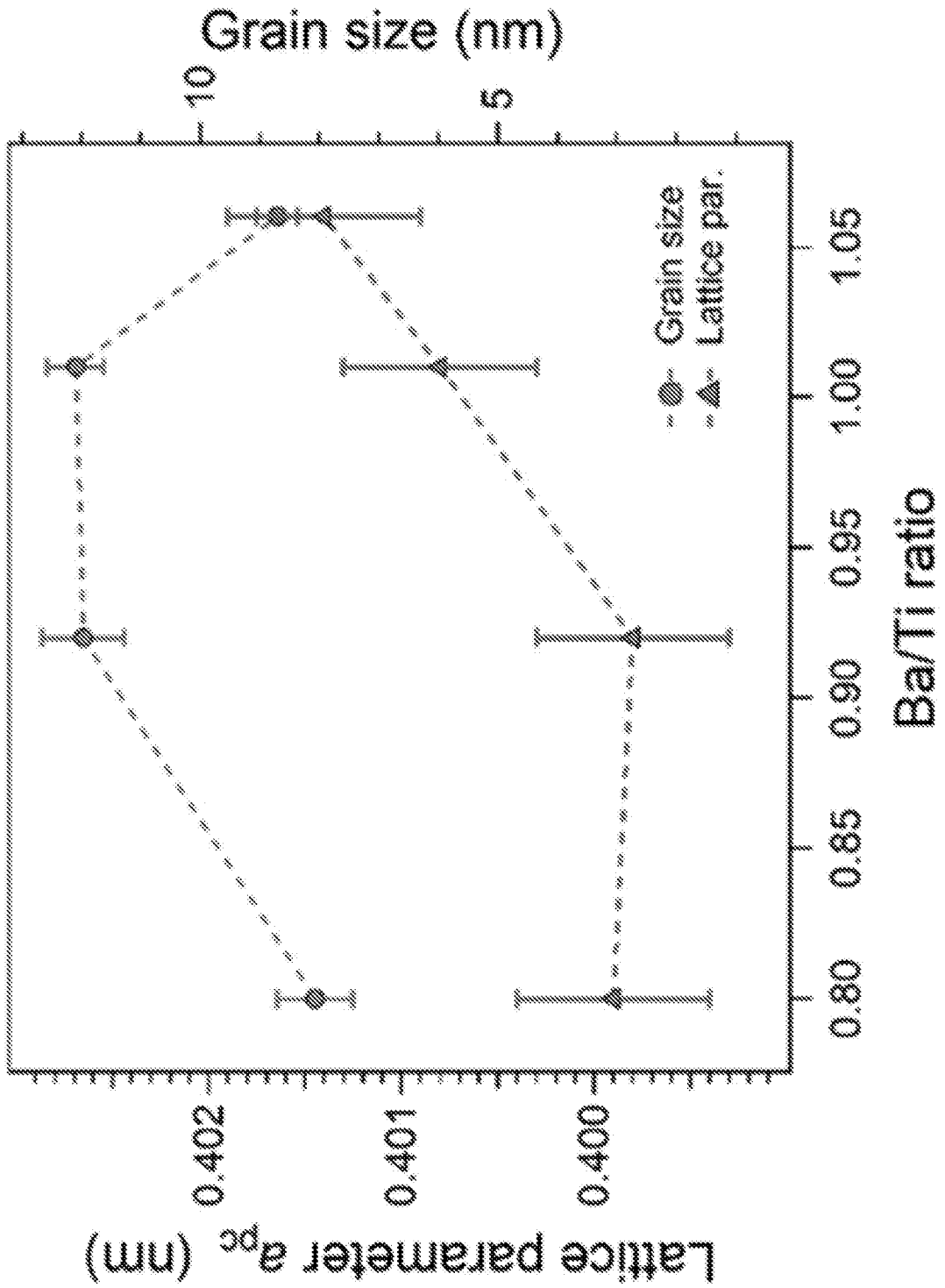
Grain size (nm)
10
5
Grain size
Lattice par.
Ba/Ti ratio
0.80
0.85
0.90
0.95
1.00
1.05
0.402
0.401
0.400
Lattice parameter a_{pc} (nm)

FIG.40

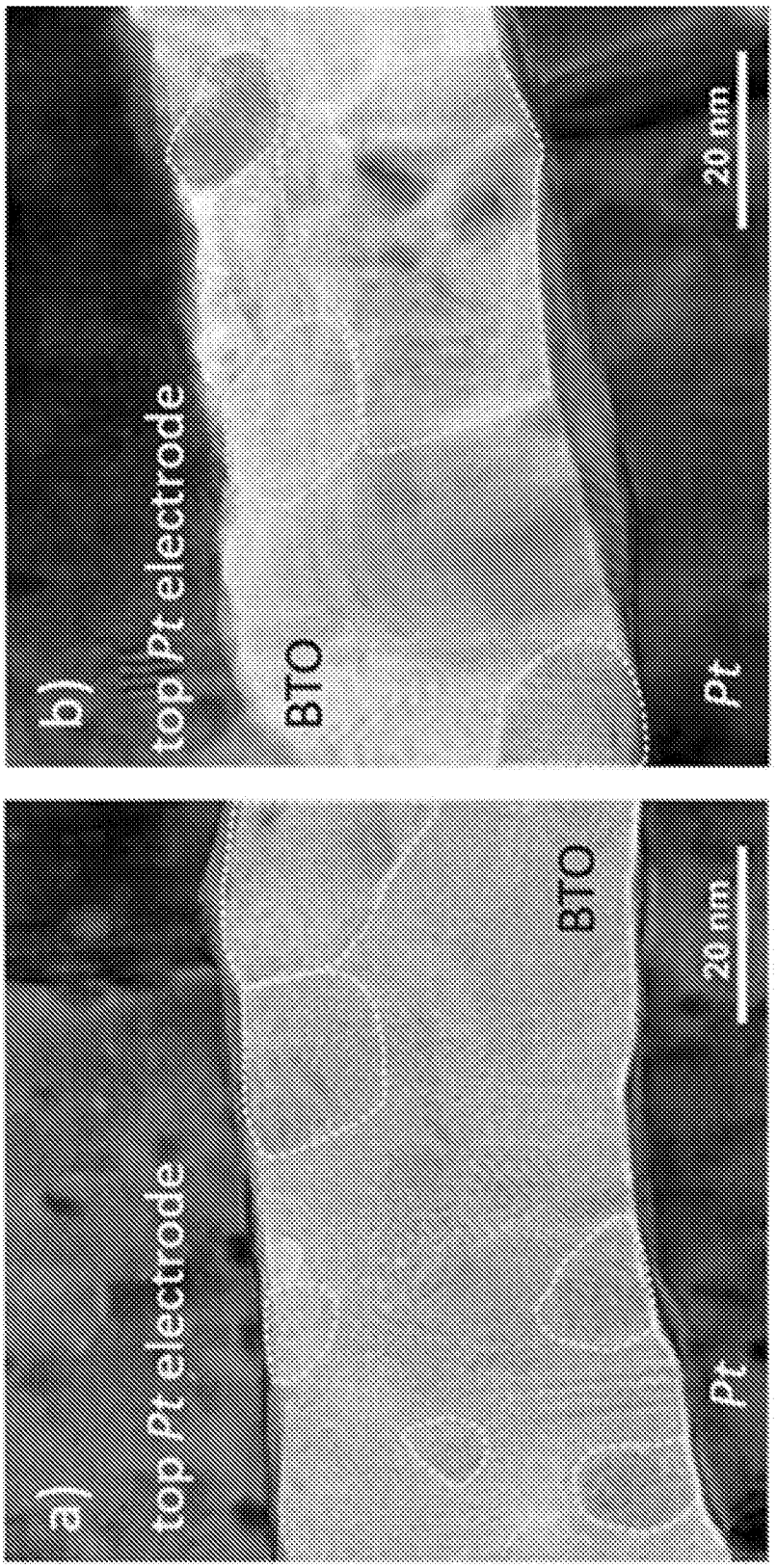

FIG. 41

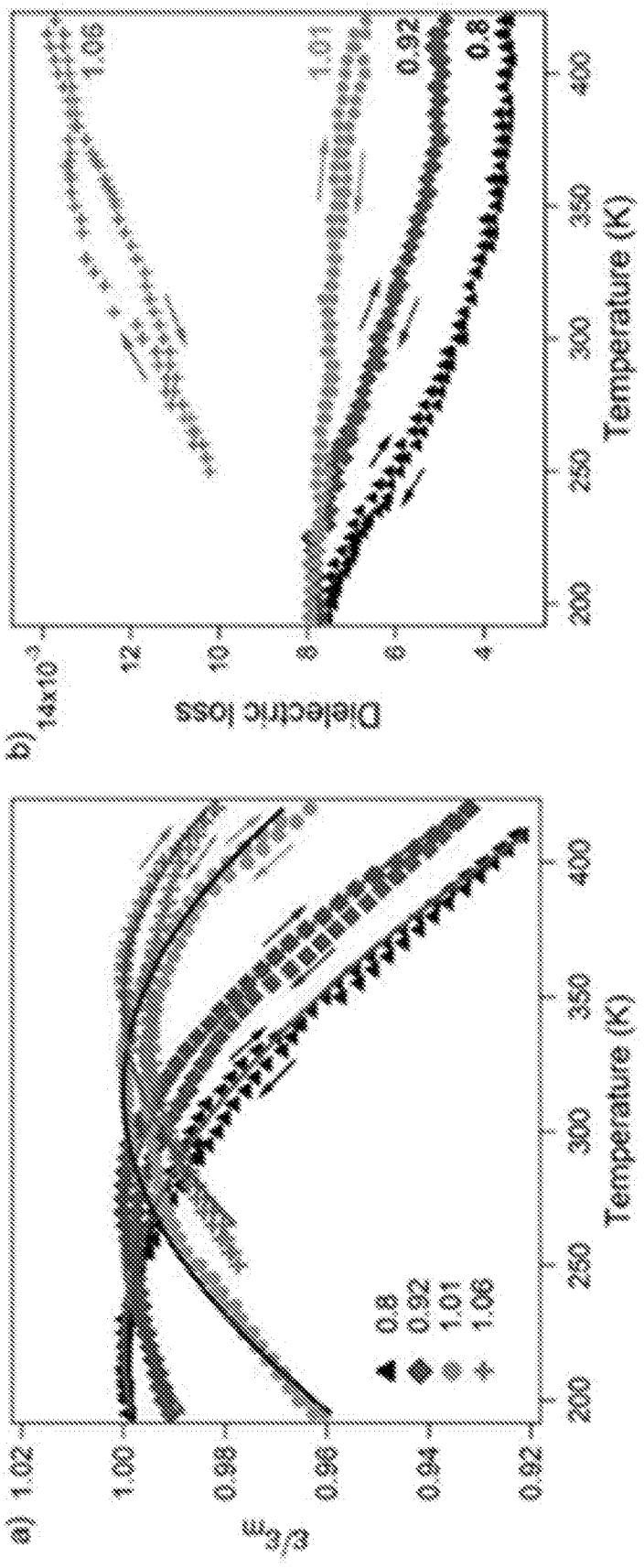
b)
Dielectric loss
Temperature (K)
0.8
0.92
1.01
1.06
c)
$\varepsilon/\varepsilon_m$
Temperature (K)
0.8
0.92
1.01
1.06

FIG. 42

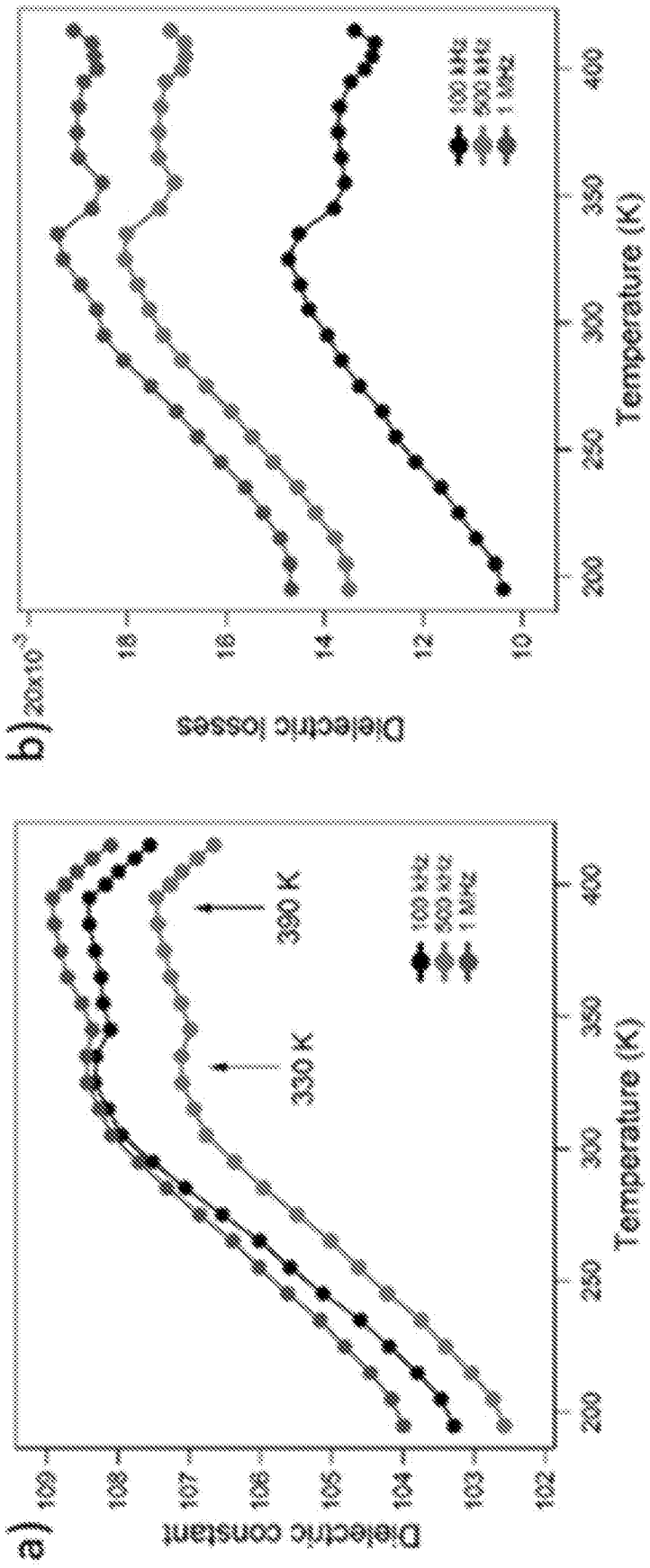
a)
Dielectric constant
109
108
107
106
105
104
103
102
200
250
300
350
400
Temperature (K)
390 K
330 K
100 kHz
400 kHz
1 MHz
b)
Dielectric losses
20x10⁻³
18
16
14
12
10
200
250
300
350
400
Temperature (K)
100 kHz
400 kHz
1 MHz

FIG. 43

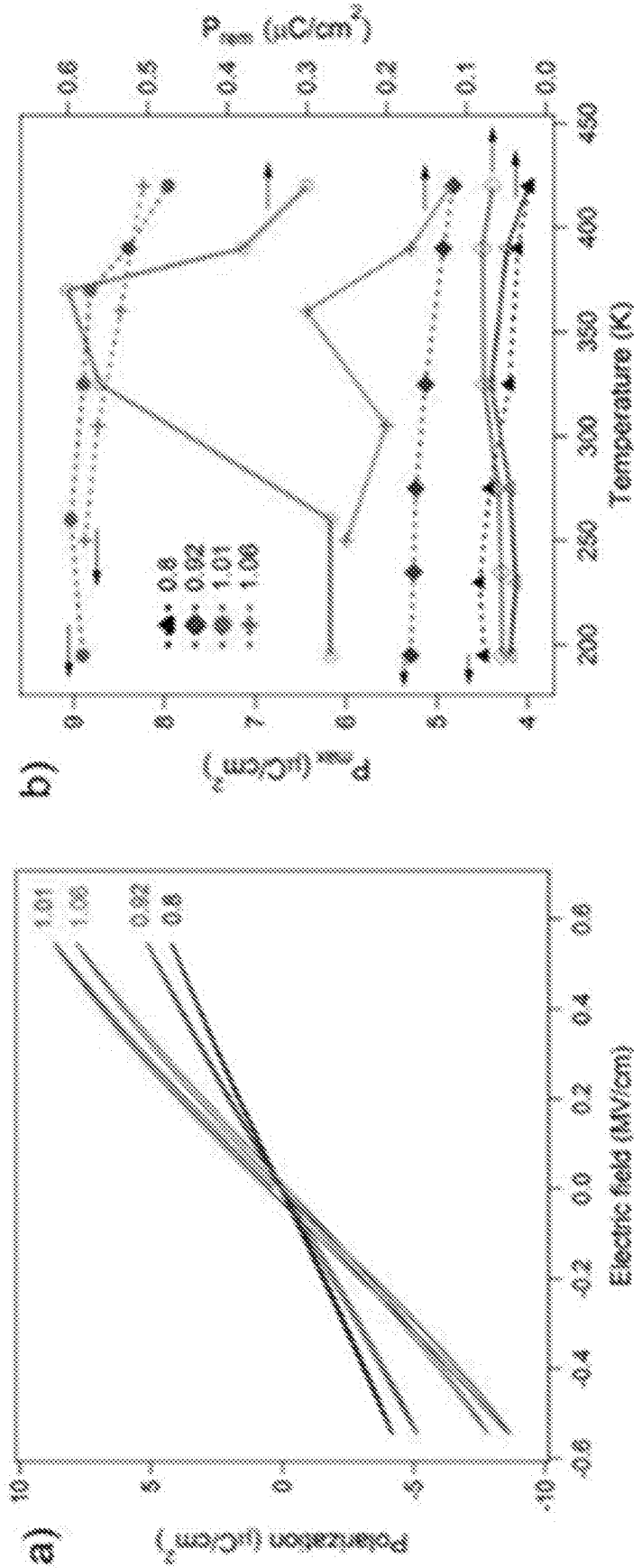
b)
P_{max} ($\mu C/cm^2$)
0.6
0.5
0.4
0.3
0.2
0.1
0.0
450
400
350
300
250
200
Temperature (K)
P_{max} ($\mu C/cm^2$)
0
-1
-2
-3
-4
0.6
0.53
0.51
0.5
a)
Polarization ($\mu C/cm^2$)
10
5
0
-5
-10
1.01
1.00
0.53
0.6
0.6
0.4
0.2
0.0
-0.2
-0.4
-0.6
Electric field (MV/cm)

FIG. 44

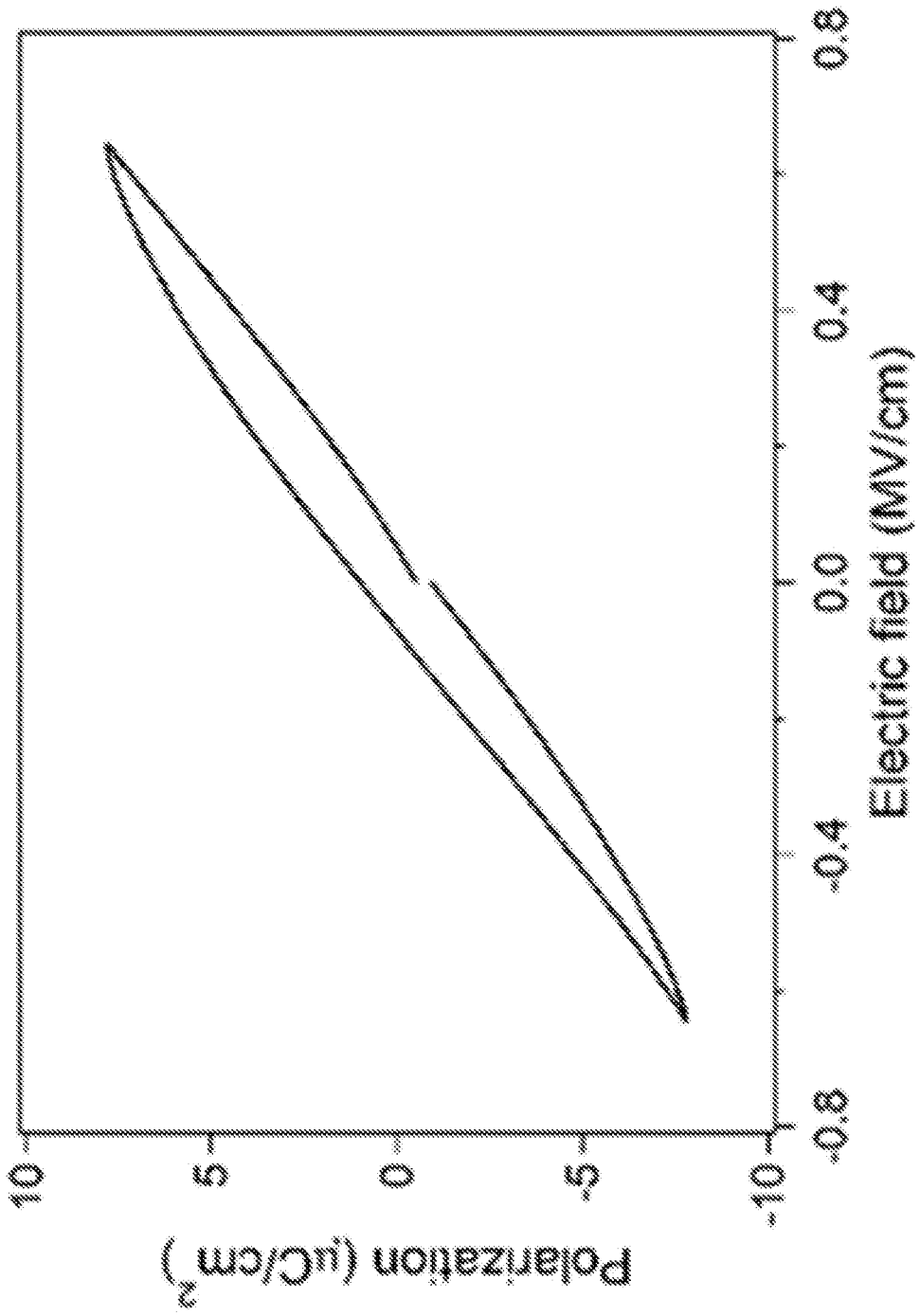
Electric field (MV/cm)
0.8
0.4
0.0
-0.4
-0.8
Polarization (μC/cm²)
10
5
0
-5
-10

FIG. 45

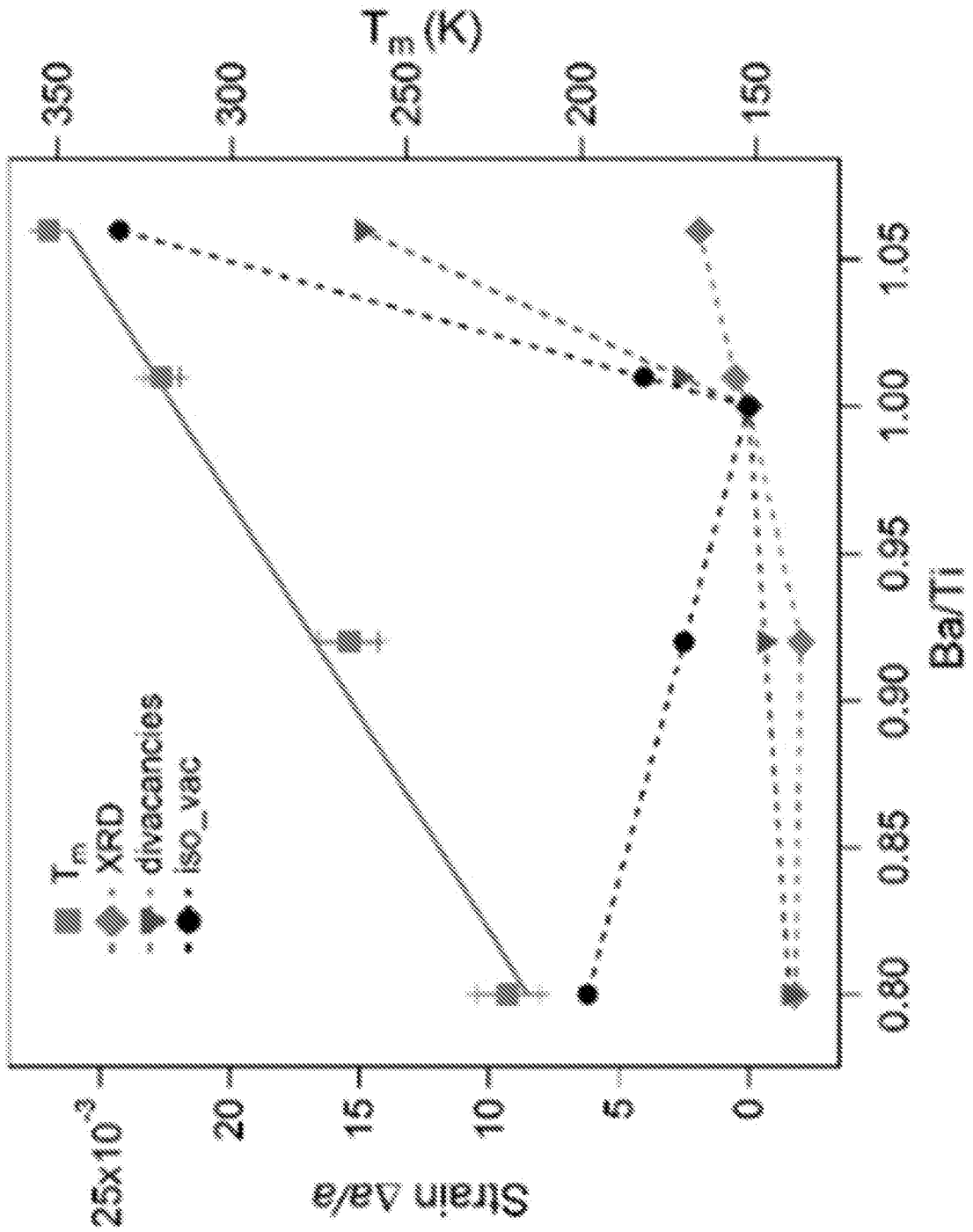
T_m (K)
350
300
250
200
150
Ba/Ti
0.80
0.85
0.90
0.95
1.00
1.05
Strain Δa/a
25x10^{-2}
20
15
10
5
0
T_m
XRD
divacancios
iso_vac

FIG. 46

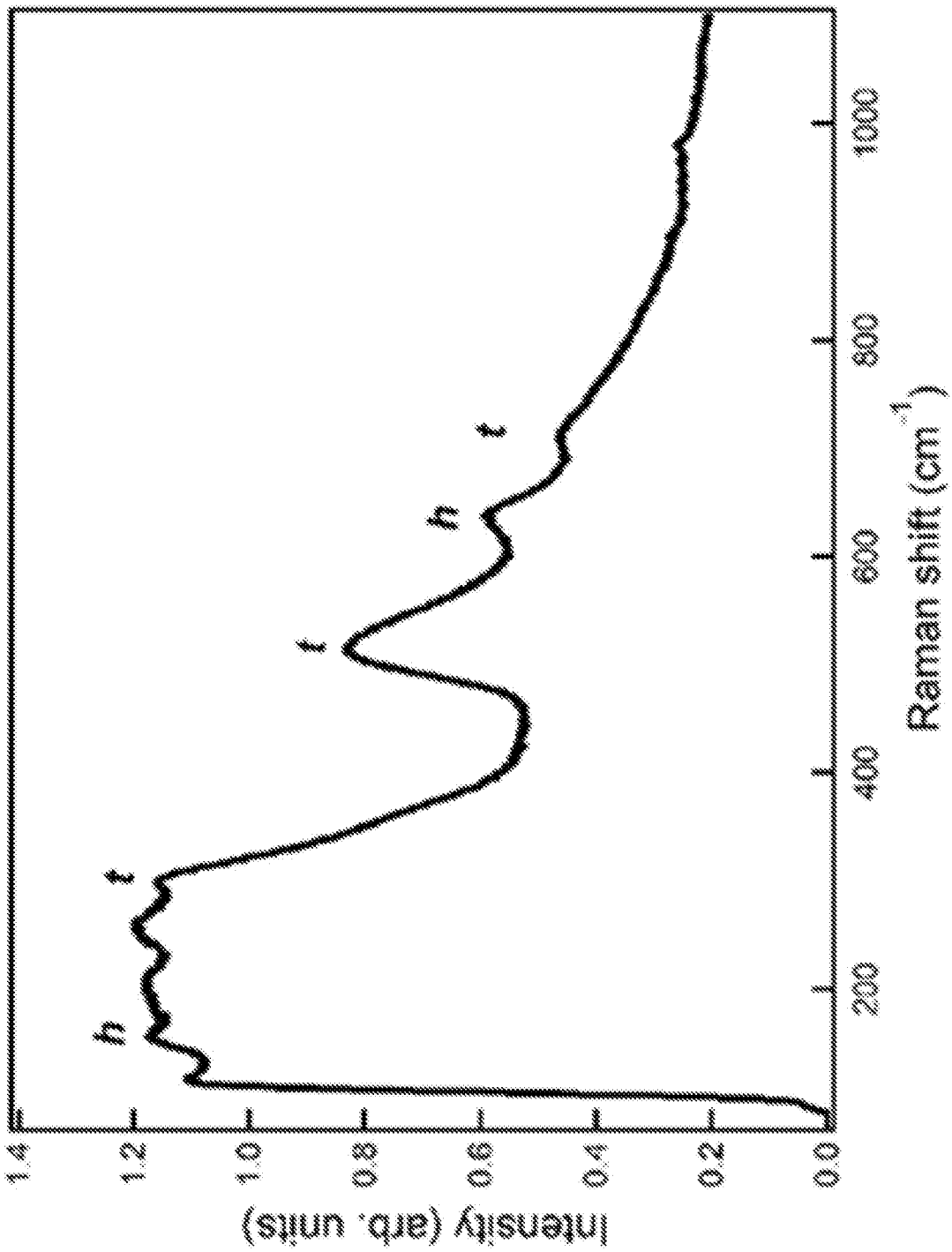
Intensity (arb. units)
0.0
0.2
0.4
0.6
0.8
1.0
1.2
1.4
200
400
600
800
1000
Raman shift (cm-1)
h
t
t
h
t
t

FIG. 47

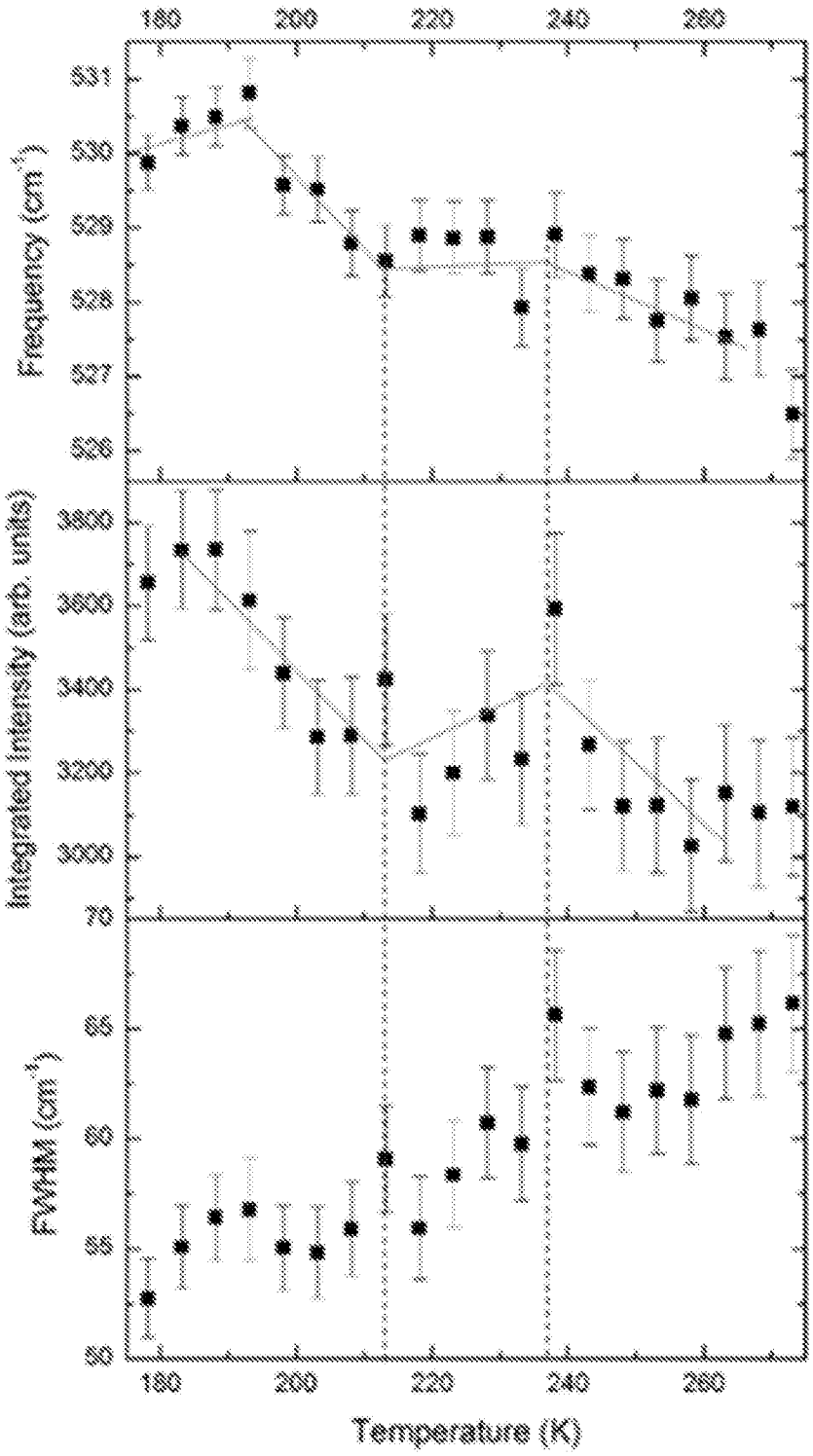
180
200
220
240
260
Frequency (cm-1)
531
530
529
528
527
526
Integrated Intensity (arb. units)
360
340
320
300
70
FWHM (cm-1)
66
65
64
63
Temperature (K)

FIG. 48

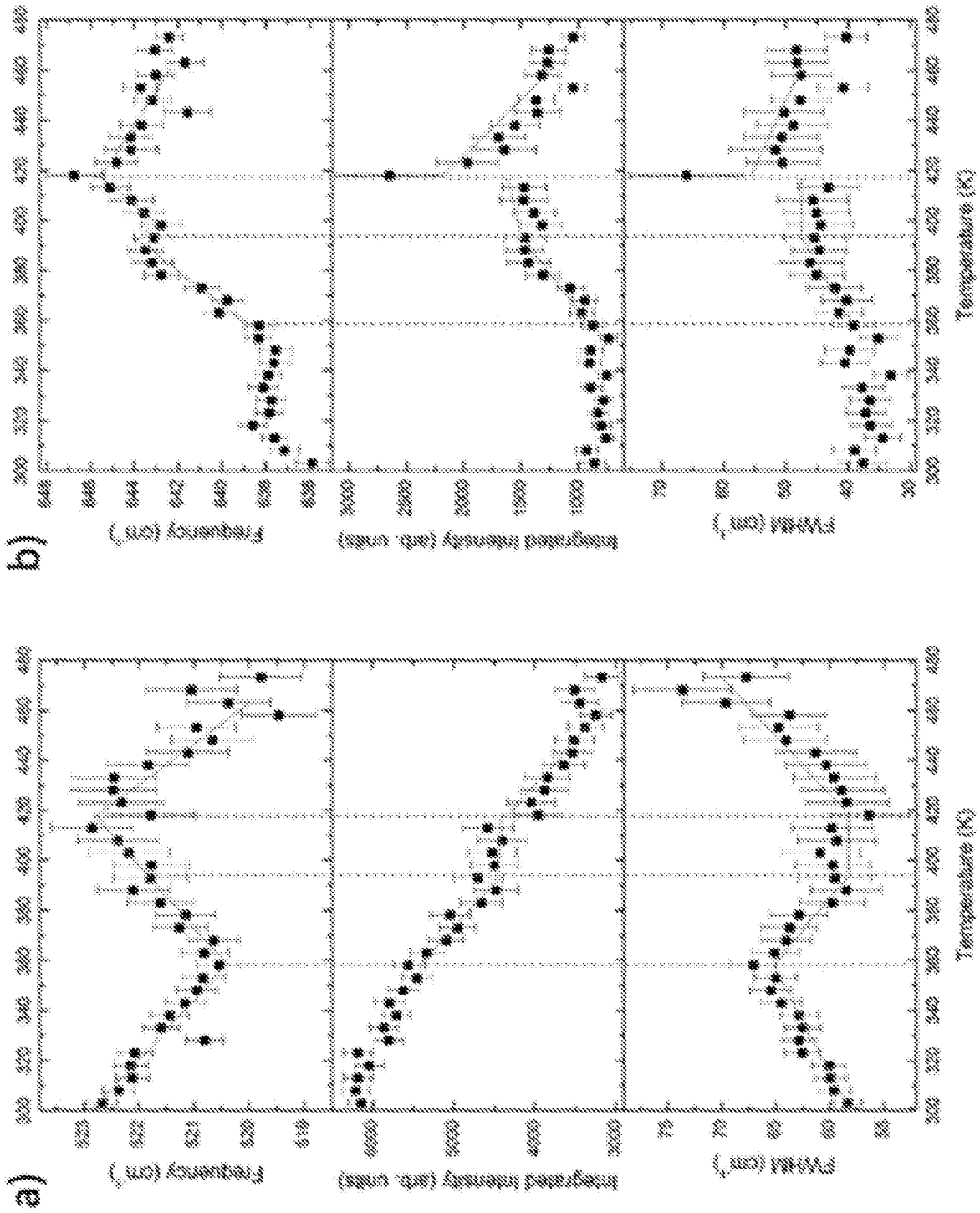
b)
a)
Temperature (K)
Frequency (cm⁻¹)
Integrated Intensity (arb. units)
FWHM (cm⁻¹)

FIG. 49

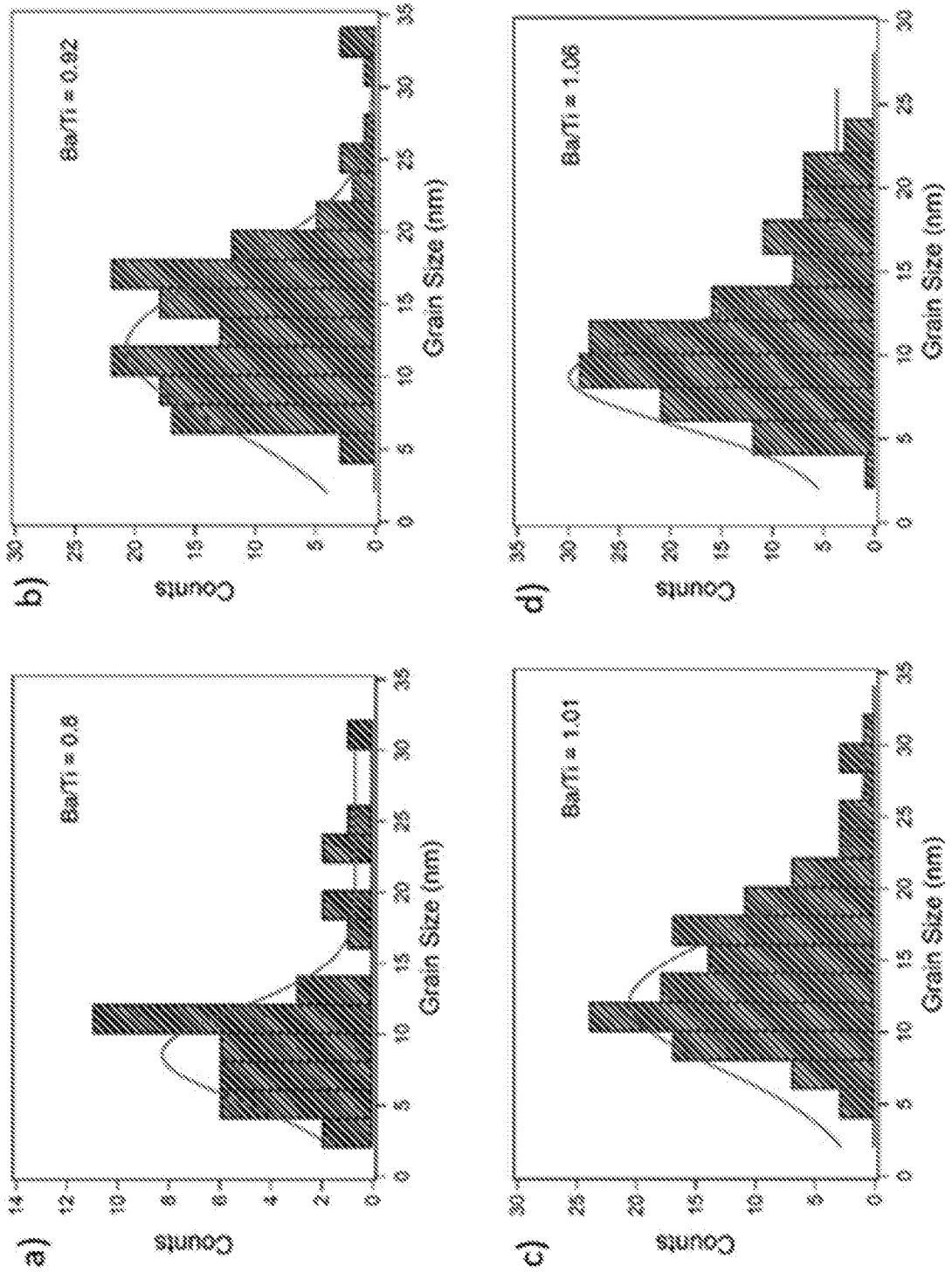
a)
Ba/Ti = 0.8
Counts
Grain Size (nm)
b)
Ba/Ti = 0.92
Counts
Grain Size (nm)
c)
Ba/Ti = 1.01
Counts
Grain Size (nm)
d)
Ba/Ti = 1.06
Counts
Grain Size (nm)

FIG. 50

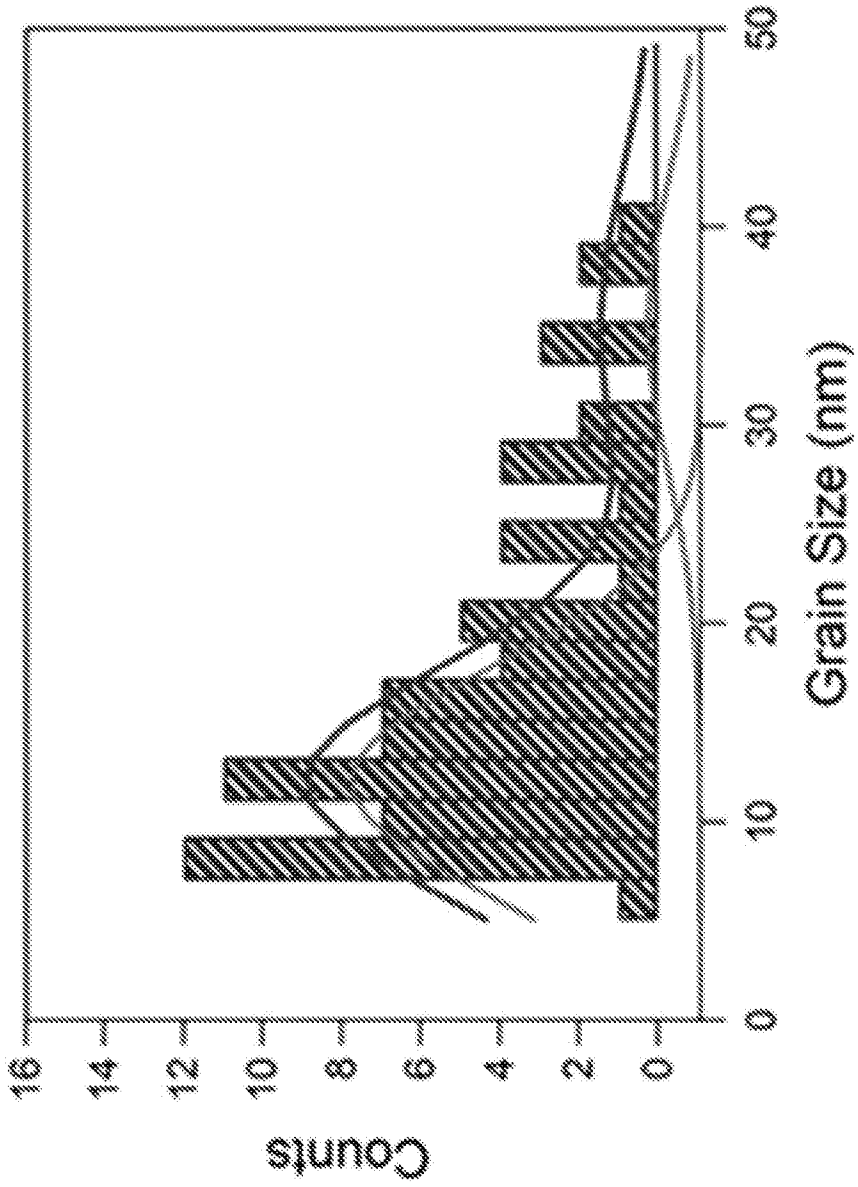

FIG. 51

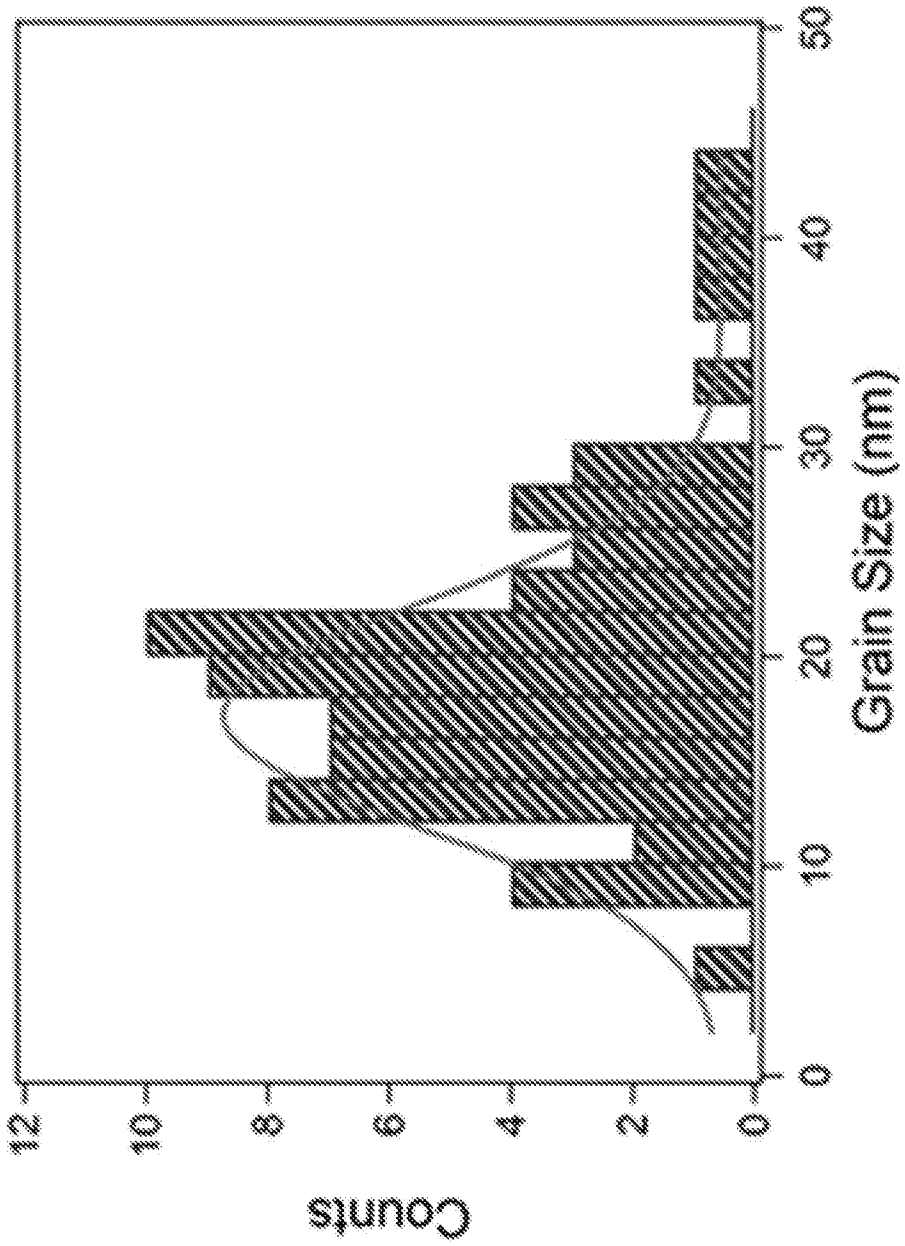

FIG. 52

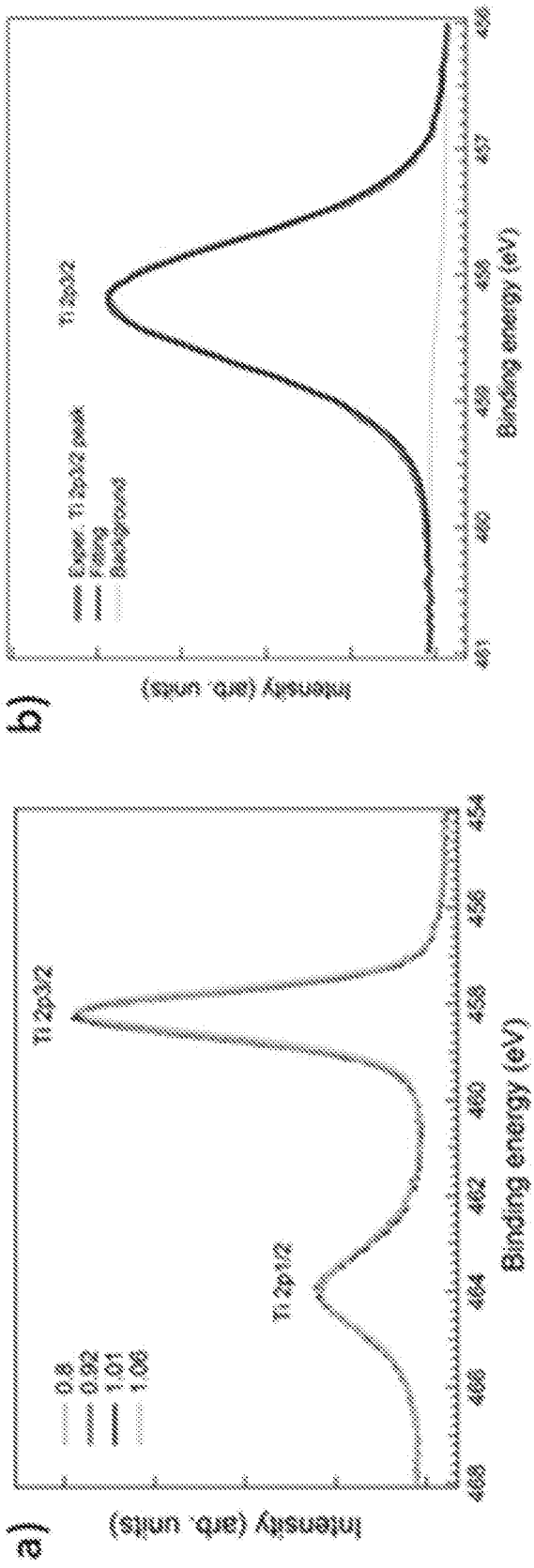
a)
Intensity (arb. units)
Ti 2p3/2
Ti 2p1/2
0.8
0.92
1.01
1.08
Binding energy (eV)
b)
Intensity (arb. units)
Ti 2p3/2
Binding energy (eV)

FIG. 53

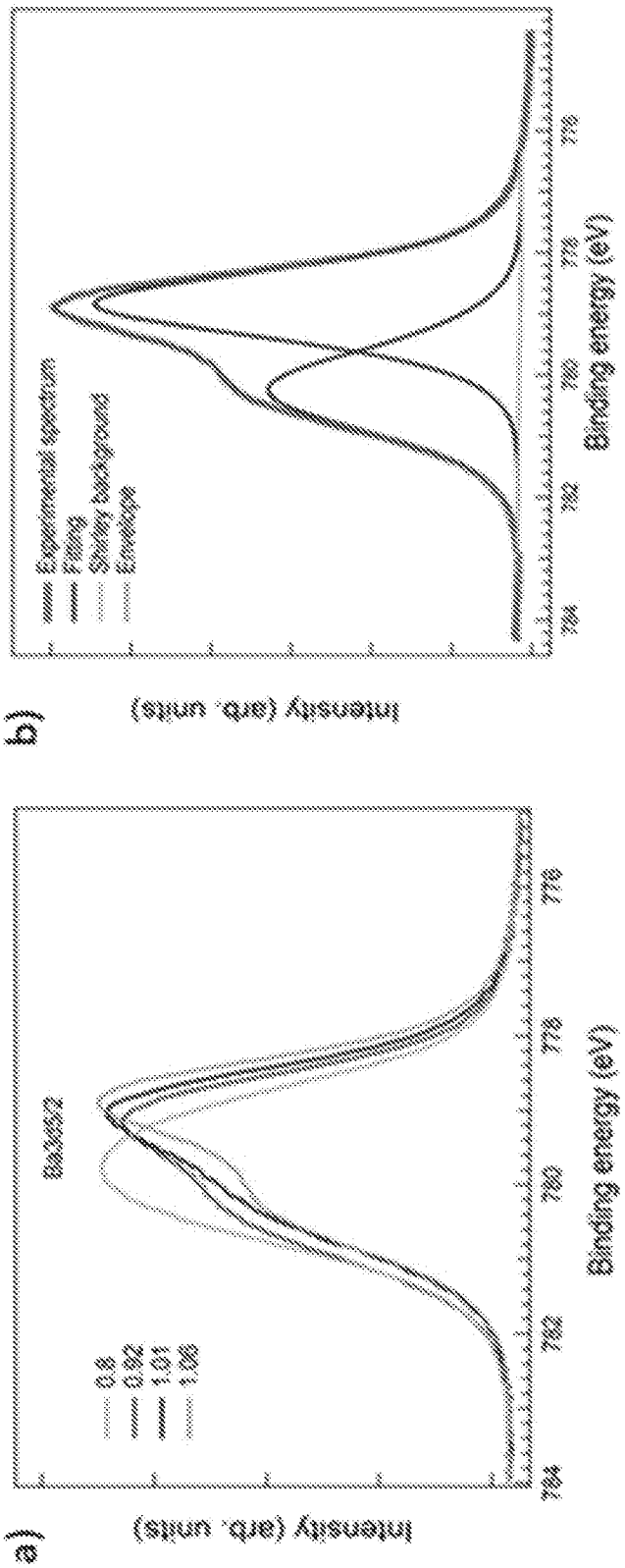
b)
Intensity (arb. units)
Experimental spectrum
Fitting
Sliding background
Envelope
784
782
780
778
776
Binding energy (eV)
a)
Intensity (arb. units)
as-cast
0.8
0.92
1.01
1.08
784
782
780
778
776
Binding energy (eV)

FIG. 54

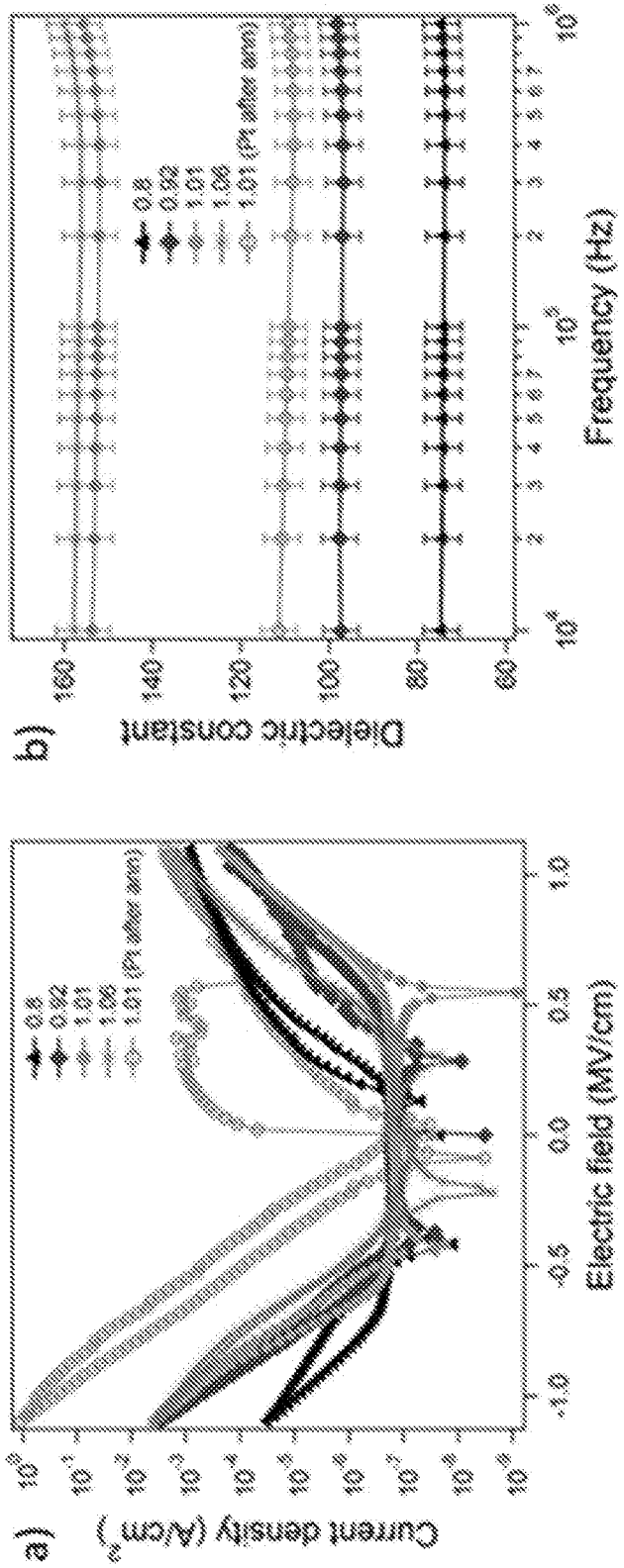
b)
Dielectric constant
160
140
120
100
80
60
10^4
10^5
10^6
Frequency (Hz)
0.8
0.92
1.01
1.08
1.01 (Pr after wu)
a)
Current density (A/cm^2)
10^{-3}
10^{-4}
10^{-5}
10^{-6}
10^{-7}
10^{-8}
10^{-9}
10^{-10}
-1.0
-0.5
0.0
0.5
1.0
Electric field (MV/cm)
0.8
0.92
1.01
1.08
1.01 (Pr after wu)

FIG. 55

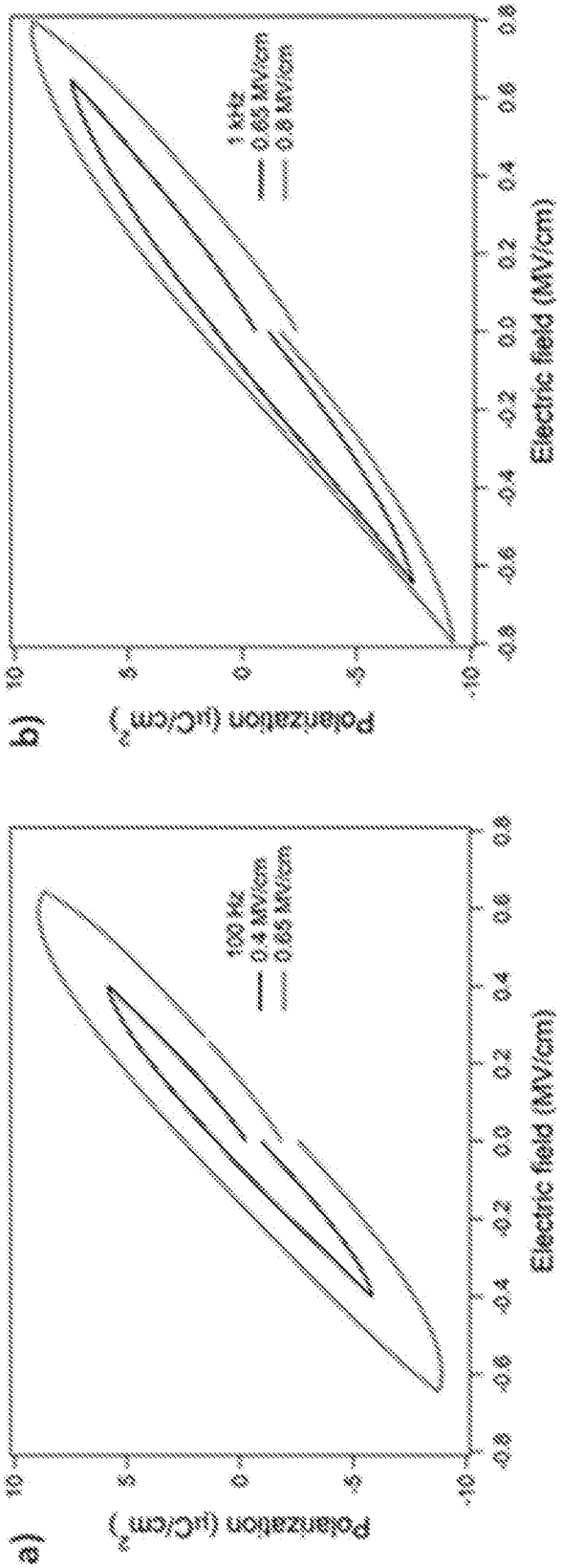
a)
100 Hz
0.4 MV/cm
0.65 MV/cm
Polarization (μC/cm²)
Electric field (MV/cm)
b)
1 kHz
0.65 MV/cm
0.8 MV/cm
Polarization (μC/cm²)
Electric field (MV/cm)

FIG. 56

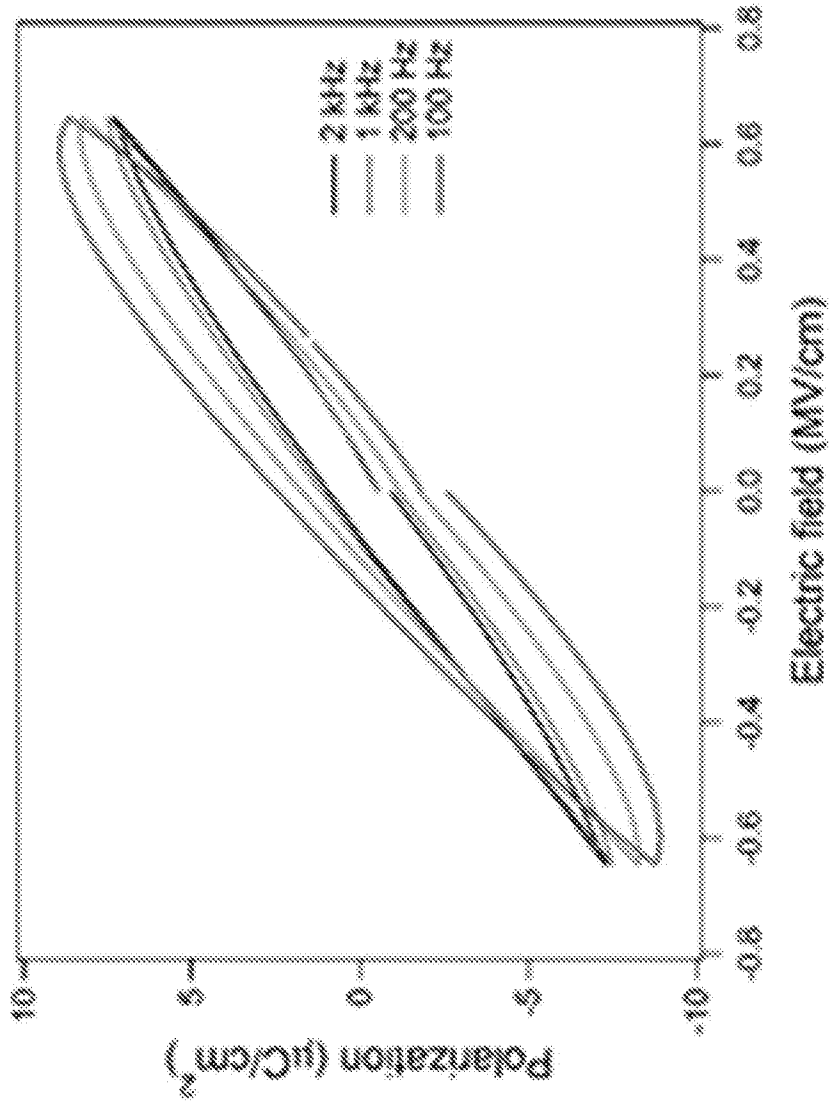
2 kHz
1 kHz
200 Hz
100 Hz
Electric field (MV/cm)
0.8
0.6
0.4
0.2
0.0
-0.2
-0.4
-0.6
-0.8
Polarization (μC/cm²)
10
5
0
-5
-10

FIG. 57

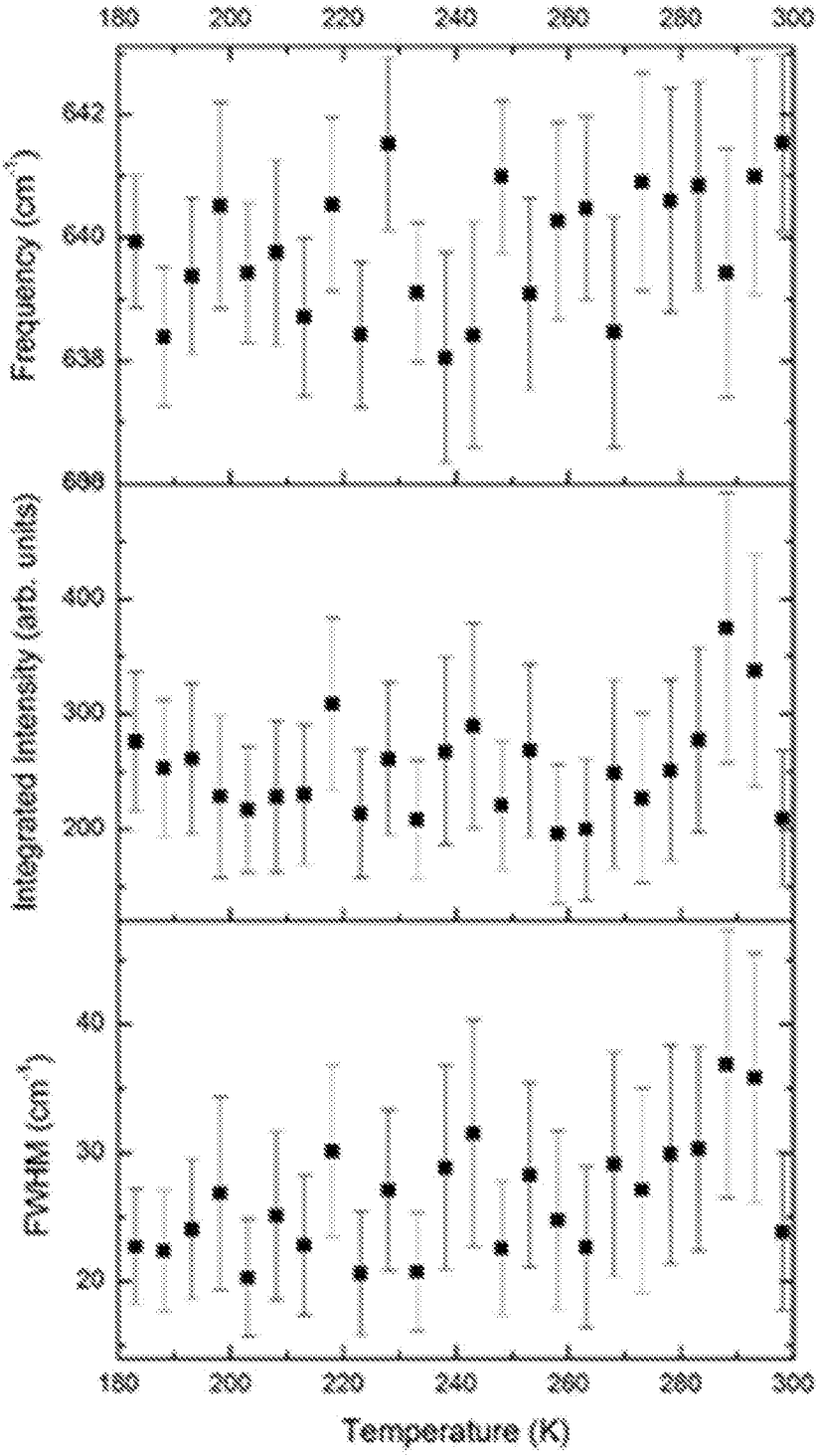
Frequency (cm^{-1})
Integrated Intensity (arb. units)
FWHM (cm^{-1})
Temperature (K)
180
200
220
240
260
280
300
632
634
636
638
640
642
20
30
40
50
60
70
10
20
30
40

FIG. 58

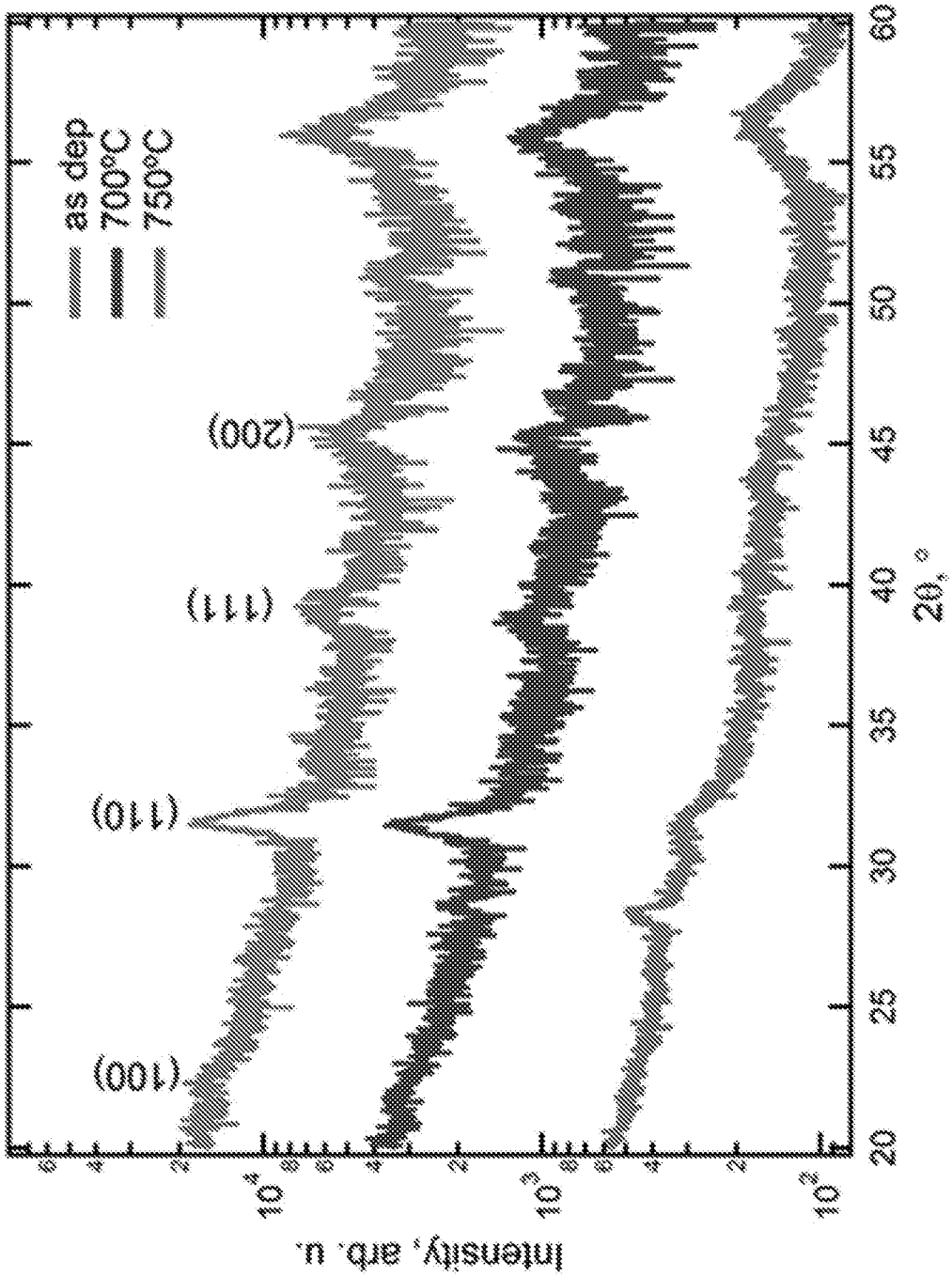

FIG. 59

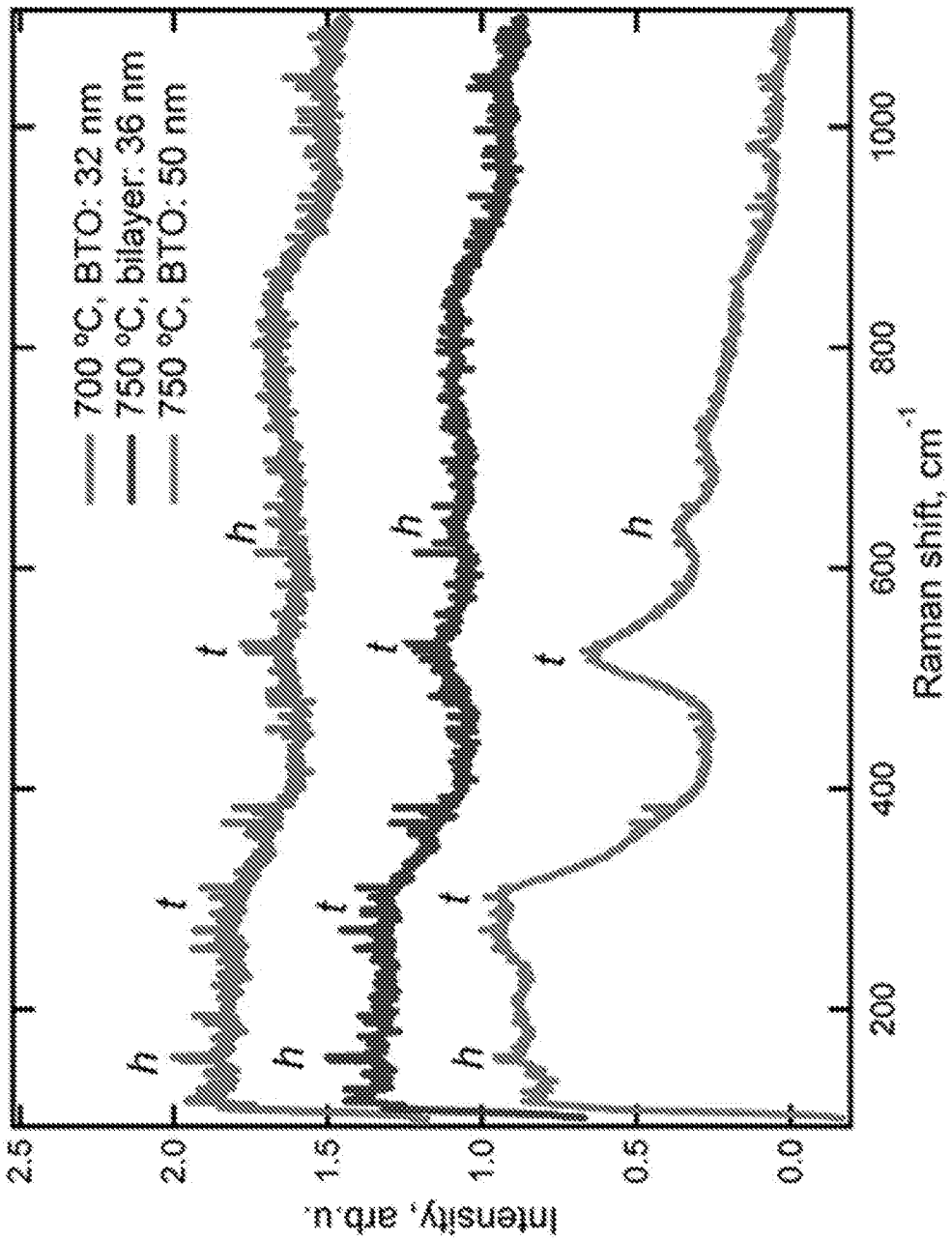
700 °C, BTO: 32 nm
750 °C, bilayer: 36 nm
750 °C, BTO: 50 nm
h
t
Intensity, arb.u.
Raman shift, cm-1
0.0
0.5
1.0
1.5
2.0
2.5
200
400
600
800
1000

FIG. 60

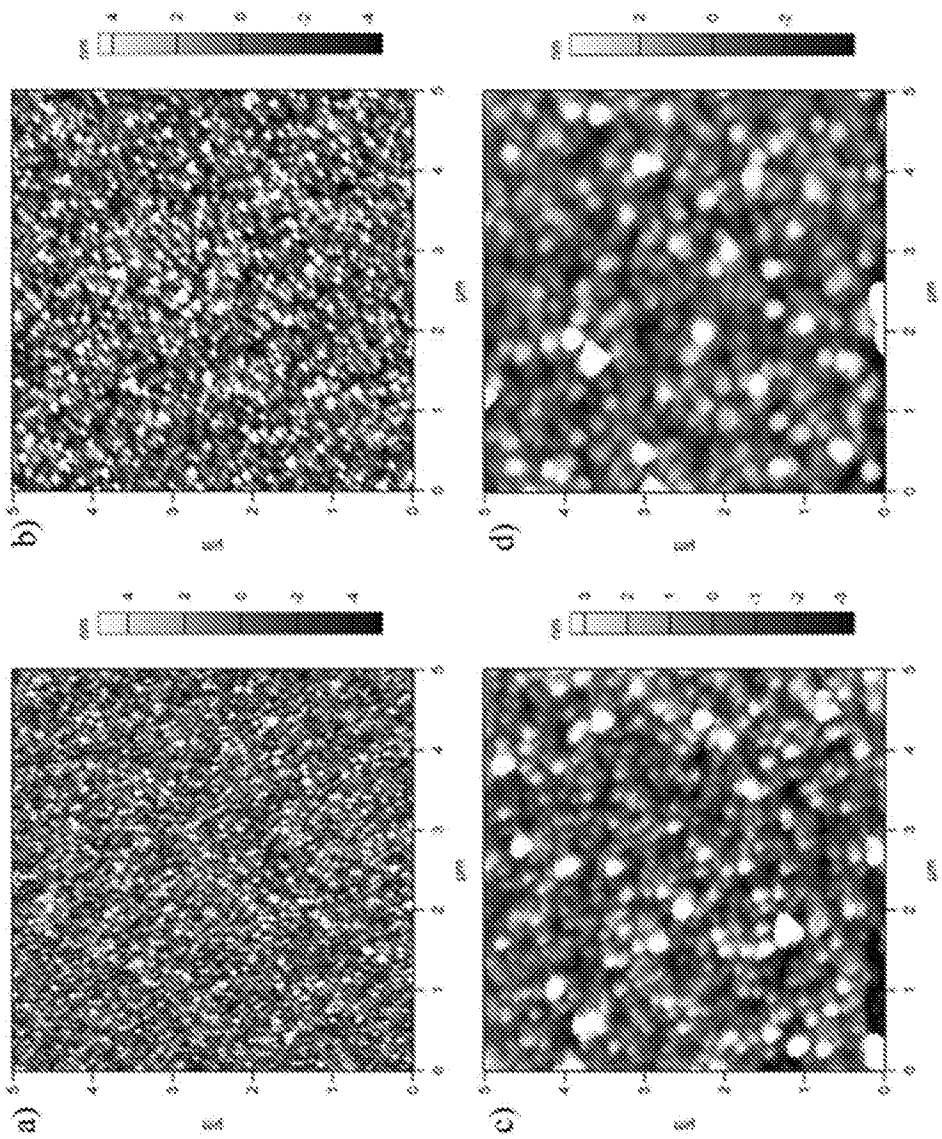

FIG. 61

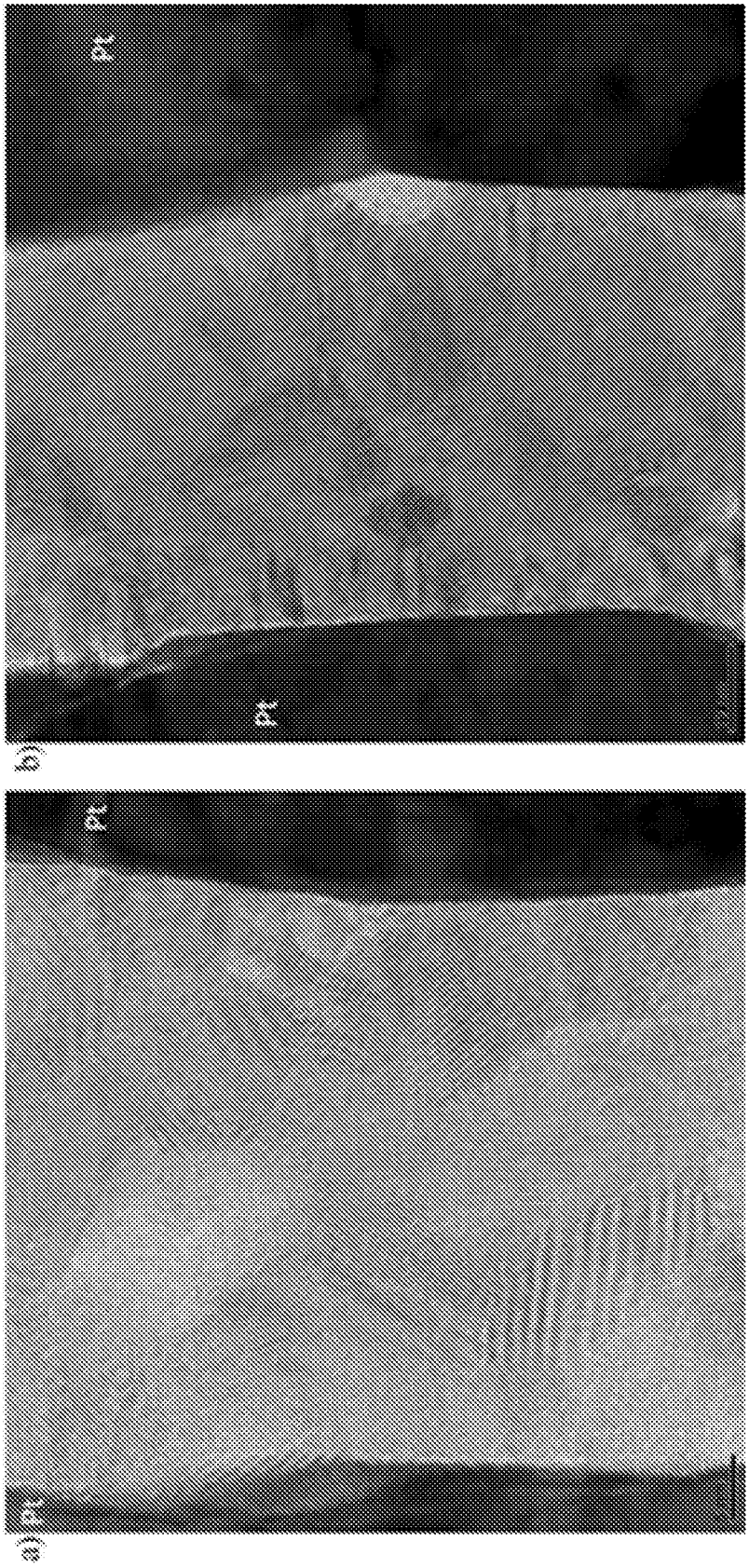

FIG. 62

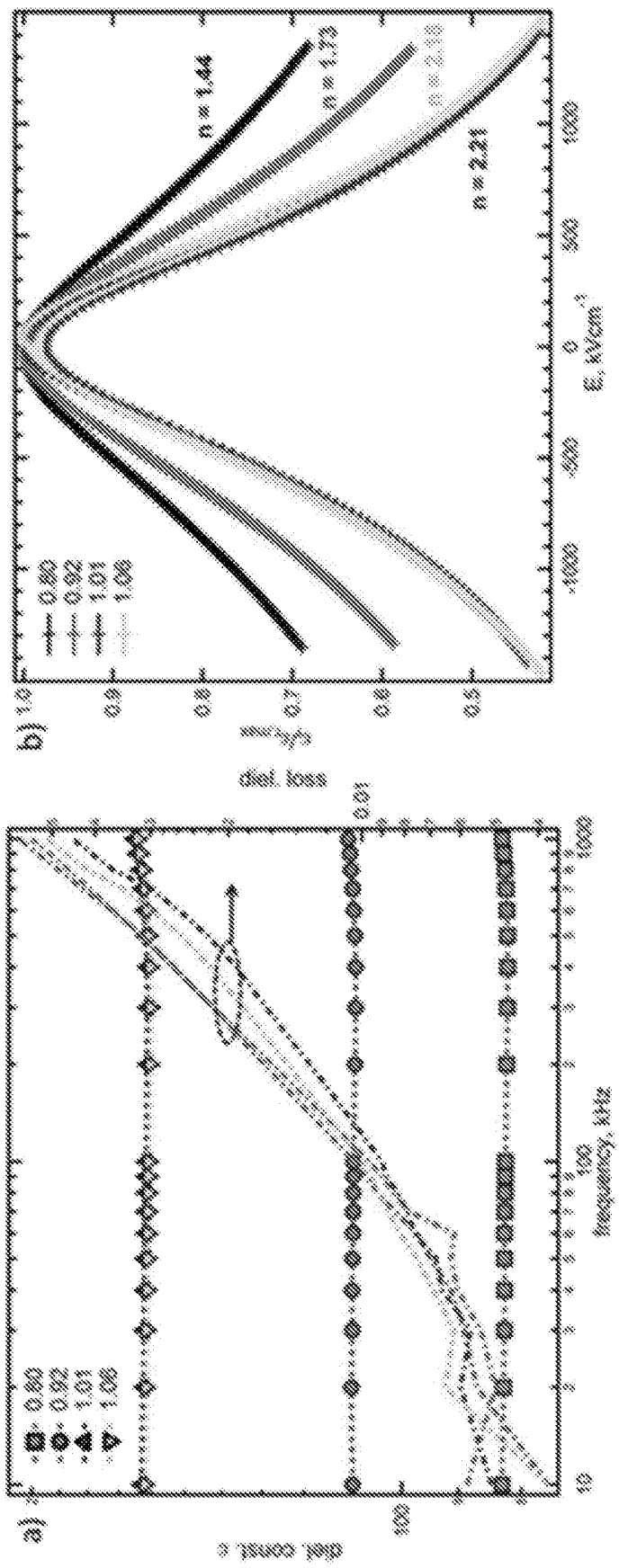
(b)
n = 1.44
n = 1.73
n = 2.21
0.90
0.92
1.01
1.08
E, kV/cm
diel. loss
(a)
diel. const. ε
frequency, kHz

FIG. 63

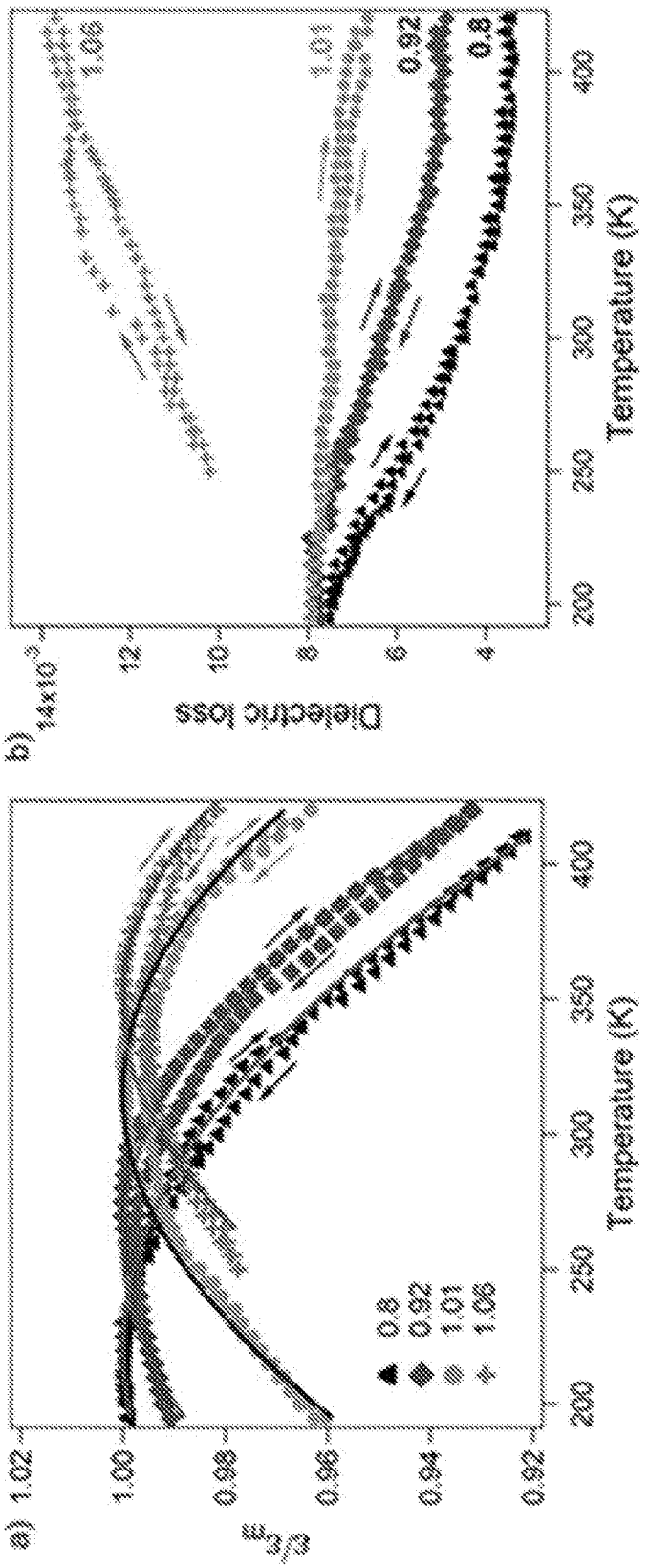
b)
Dielectric loss
14x10^-3
12
10
8
6
4
200
250
300
350
400
Temperature (K)
1.06
1.01
0.92
0.8
a)
$\varepsilon/\varepsilon_m$
1.02
1.00
0.98
0.96
0.94
0.92
0.8
0.92
1.01
1.06

FIG. 64

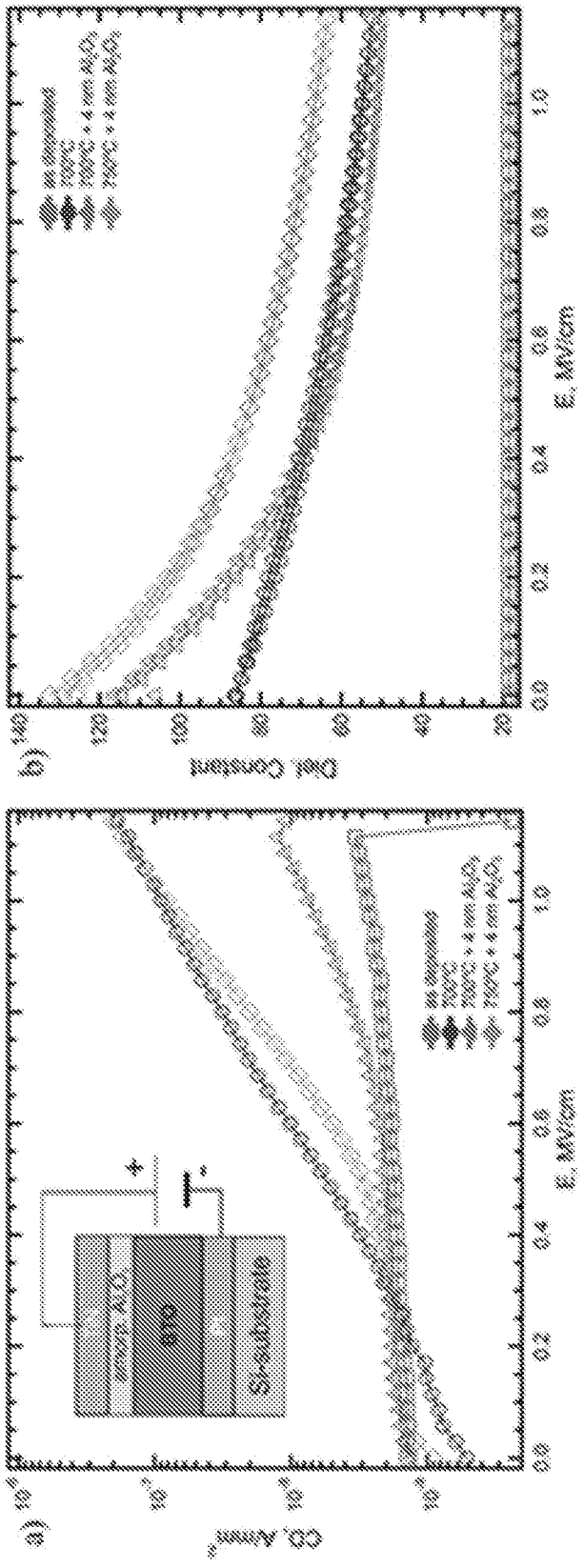

FIG. 65

INTERNATIONAL SEARCH REPORT

International application No.
PCT/US 19/61271

A. CLASSIFICATION OF SUBJECT MATTER

IPC - H01L 51/00 (2019.01)

CPC - H01L 51/004; H01L 51/0048; H01L 51/0076; H01L 51/0093; H01L 2031/0344; H01L 51/0003

According to International Patent Classification (IPC) or to both national classification and IPC

B. FIELDS SEARCHED

Minimum documentation searched (classification system followed by classification symbols)
See Search History document

Documentation searched other than minimum documentation to the extent that such documents are included in the fields searched
See Search History document

Electronic data base consulted during the international search (name of data base and, where practicable, search terms used)
See Search History document

C. DOCUMENTS CONSIDERED TO BE RELEVANT

Category*	Citation of document, with indication, where appropriate, of the relevant passages	Relevant to claim No.
X -- Y	US 5,453,908 A (Tsu et al.) 26 September 1995 (26.09.1995); abstract, col 1, ln 38-39, 65-66, col 2, ln 21-24, 62, 67, col 3, ln 1-3, 21-24, col 4, ln 7-10, col 5, ln 21-22, 45-67, col 6, ln 12-13, 18-19	1-6, 8, 12-20 ---------- 7, 9-11
Y	Ahn et al. "Effect of Al2O3 insertion on the electrical properties of SrTiO3 thin films: A comparison between Al2O3-doped SrTiO3 and SrTiO3/Al2O3/SrTiO3 sandwich structure" Materials Research Bulletin. 2015, vol 64, pg. 1-5; pg. 1, abstract, pg. 2, Fig. 1, pg. 4, Fig. 4a	7, 9-11
A	US 2015/0298161 A1 (UNIVERSITEIT GENT) 22 October 2015 (22.10.2015); entire document	1-20
A	WO 2017/087611 A1 (ALLIANCE FOR SUSTAINABLE ENERGY, LLC) 26 May 2017 (26.05.2017); entire document	1-20
A	US 7,029,971 B2 (Borland et al.) 18 April 2006 (18.04.2006); entire document	1-20

☐ Further documents are listed in the continuation of Box C. ☐ See patent family annex.

* Special categories of cited documents:
"A" document defining the general state of the art which is not considered to be of particular relevance
"D" document cited by the applicant in the international application
"E" earlier application or patent but published on or after the international filing date
"L" document which may throw doubts on priority claim(s) or which is cited to establish the publication date of another citation or other special reason (as specified)
"O" document referring to an oral disclosure, use, exhibition or other means
"P" document published prior to the international filing date but later than the priority date claimed
"T" later document published after the international filing date or priority date and not in conflict with the application but cited to understand the principle or theory underlying the invention
"X" document of particular relevance; the claimed invention cannot be considered novel or cannot be considered to involve an inventive step when the document is taken alone
"Y" document of particular relevance; the claimed invention cannot be considered to involve an inventive step when the document is combined with one or more other such documents, such combination being obvious to a person skilled in the art
"&" document member of the same patent family

Date of the actual completion of the international search	Date of mailing of the international search report
13 January 2020	28 JAN 2020
Name and mailing address of the ISA/US Mail Stop PCT, Attn: ISA/US, Commissioner for Patents P.O. Box 1450, Alexandria, Virginia 22313-1450 Facsimile No. 571-273-8300	Authorized officer Lee Young Telephone No. PCT Helpdesk: 571-272-4300

INTERNATIONAL SEARCH REPORT

International application No.
PCT/US 19/61271

Box No. II Observations where certain claims were found unsearchable (Continuation of item 2 of first sheet)

This international search report has not been established in respect of certain claims under Article 17(2)(a) for the following reasons:

1. ☐ Claims Nos.:
because they relate to subject matter not required to be searched by this Authority, namely:

2. ☐ Claims Nos.:
because they relate to parts of the international application that do not comply with the prescribed requirements to such an extent that no meaningful international search can be carried out, specifically:

3. ☒ Claims Nos.: 21-22
because they are dependent claims and are not drafted in accordance with the second and third sentences of Rule 6.4(a).

Box No. III Observations where unity of invention is lacking (Continuation of item 3 of first sheet)

This International Searching Authority found multiple inventions in this international application, as follows:

1. ☐ As all required additional search fees were timely paid by the applicant, this international search report covers all searchable claims.

2. ☐ As all searchable claims could be searched without effort justifying additional fees, this Authority did not invite payment of additional fees.

3. ☐ As only some of the required additional search fees were timely paid by the applicant, this international search report covers only those claims for which fees were paid, specifically claims Nos.:

4. ☐ No required additional search fees were timely paid by the applicant. Consequently, this international search report is restricted to the invention first mentioned in the claims; it is covered by claims Nos.:

Remark on Protest

☐ The additional search fees were accompanied by the applicant's protest and, where applicable, the payment of a protest fee.

☐ The additional search fees were accompanied by the applicant's protest but the applicable protest fee was not paid within the time limit specified in the invitation.

☐ No protest accompanied the payment of additional search fees.